MULTI-SEGMENT WAVEGUIDE PHOTODETECTORS FOR HIGH RESOLUTION WAVELENGTH MONITORING NEAR 1.55 μm

by

ADAM DENSMORE

B.Sc. (Ottawa) 1996

A Thesis
Submitted to the School of Graduate Studies
in Partial Fulfilment of the Requirements
for the Degree
Doctor of Philosophy

McMaster University

SEGMENTED WAVEGUIDE PHOTODETECTORS FOR WAVELENGTH MONITORING

DOCTOR OF PHILOSOPHY (December 2001) McMaster University
(Engineering Physics) Hamilton, Ontario

TITLE: Multi-Segment Waveguide Photodetectors For High Resolution Wavelength Monitoring Near 1.55 μm

AUTHOR: Adam Densmore

SUPERVISORS: Dr. P.E. Jessop

NUMBER OF PAGES: ix, 122

Abstract

This thesis documents the development of a new optoelectronic device capable of functioning as a high resolution wavelength monitor near 1.55 μm. The primary objective of this work was to devise a simple and potentially low cost approach to monitor wavelength shifts in wavelength division multiplexing (WDM) networks and fiber Bragg grating optical strain sensors.

The presented technique utilizes in-line pairs of quantum well waveguide photodiodes fabricated in an InGaAsP/InP material system. The ratio of photocurrents produced between two consecutive waveguide detectors is taken as a sensitive measure of wavelength near the absorption band edge of the quantum wells. The device is shown to function over the conventional wavelength band with near pm wavelength sensitivity, while performing independently of the optical input power and signal polarization. The simultaneous monitoring of several incoming wavelengths is also demonstrated, where arrays of in-line detectors are utilized with a wavelength demultiplexer.

In this thesis, several unique methods are presented to improve the performance of the devices, including the use of the quantum confined Stark effect to expand the wavelength operating range and to reduce the thermal sensitivity. Finally, as a practical demonstration, the in-line detectors are used to track the small wavelength shifts induced in various types of fiber Bragg grating optical strain sensors.

Acknowledgements

Without the help of several people this work would not have been possible. Firstly, I would like to thank my supervisor Dr. Paul Jessop for his guidance, patience and for introducing me to this exciting research field. Next, I would like to acknowledge Dr. Doug Bruce whose valuable advice and assistance with device fabrication were invaluable. For generous financial support of my graduate education, I would like to thank the Natural Sciences and Engineering Research Council of Canada and the Department of Engineering Physics at McMaster University.

Material growths used in this thesis were performed by Brad Robinson and were greatly appreciated. Thanks to our summer research assistants Brian Mitchell and Danica Rogers for help with the detector electronics and LabView programming.

My deepest gratitude to my parents Ashley and Joanne who have encouraged me in all of my endeavors. Their love and support have been the most important influences in my life and for this I will be eternally grateful.

On a personal note, I would like to thank Amanda Bullen for putting up with me during the tough times and for bringing joy to my life.

Lastly, I would like to thank my colleagues in the lab who always kept graduate life interesting. In no particular order, my warmest regards to Luke, Ed, Matt, Ted, Debbie, Christine, Chris, Graham, Phil, Sam, Mark, Sean, Gord, Greg, John, Mike C, Peter M and J and all the rest. I hope that we all stay in touch.

Contents

List of Figures

List of Tables

Chapter 1

Introduction

The rapid growth of the Internet and other interactive services has caused an enormous increase in the information traffic being transmitted around the globe. These explosive trends are expected to continue well into the next 30 years, as the number of Internet users and the sophistication of information-based applications grow. Conventional copper wire lines cannot handle such traffic volume and alternative technologies, such as the optical fiber, have become essential to support this magnitude of data exchange.

Society now depends on fiber optic systems to provide a variety of services, many of which influence our daily lives. These services encompass a broad range of applications from strain sensing in bridges to broadband Internet access. To meet the public's ever increasing demands for information-based services, advanced lightwave systems are rapidly being deployed. Digital data of many forms including telephone, television, fax machine and modem signals, are now being transmitted over optical fibers. Thus far, the majority of research has been directed towards telecommunications, which has been the main driving force behind this technology.

One of the reasons why fiber-based systems have become so successful is the development of high performance optoelectronic semiconductor devices. These components have demonstrated reliable and efficient operation, while being relatively inexpensive to manufacture [1]. Devices such as waveguides, lasers, photodetectors, modulators, optical amplifiers and wavelength demultiplexers are now being routinely fabricated.

Monolithic integration of these components onto the same semiconductor chip to form an optoelectronic integrated circuit (OEIC) is a desirable and ambitious goal. OEICs offer increased functionality, improved performance and a reduced size, while significantly lowering the manufacturing costs. For these reasons, extensive work has been focused towards their development.

1.1 Optical Communication Systems

The most basic type of optical communication system consists of an optical source (usually a laser diode), a silica fiber transmission medium, an optical amplifier and a photodetector. After being coded for transmission, electrical data is converted to an optical signal by directly modulating the output power of a laser diode. The optical signal is then transmitted through a fiber cable until it arrives at its destination. During transmission, the signal degrades due to attenuation in the fiber. One of the main advantages of optical communication systems is the low loss properties of silica fibers, allowing amplification or repeater stations to be spaced much further apart than in electrical systems. During transit, the signal is amplified and then received by a photodetector at its destination, where it is converted back to the electrical domain to be analyzed.

Two common wavelength transmission "windows" are used with silica glass fibers: 1.3 μm, where there is a local minimum in fiber attenuation and dispersion; and 1.55 μm, where an absolute minimum in fiber attenuation is located [2]. Since the advent of the Erbium doped fiber amplifier (EDFA), significant research has been directed towards the 1.55 μm communications band. The EDFA offers a highly desirable means for all optical amplification, typically over a range of 1.53-1.56 μm, known as the conventional, or "C"-wavelength band. Significant research effort is now being conducted to extend this range to longer wavelengths or into the "L"-band. Traditional amplifiers were based on the use of electro-optic repeaters, in which the optical signal was transferred to the electrical domain using a photodetector, and then amplified with a standard transistor amplifier. The amplified electrical signal was then used to drive another laser diode, transforming the information back to the optical domain.

This technology was very expensive and separate repeaters were required for each wavelength in the system. For the above reasons, 1.55 μm systems now dominate the telecommunication industry.

Despite the increased carrying capacity offered by the optical fiber, there are still capacity problems. Obvious solutions are to simply lay more fiber cable or to increase the data bit rate at which information is transmitted through the system. The installation of new fiber is a very costly answer and service providers usually wish to avoid this solution whenever possible. Work focusing on techniques to improve the frequency response of the transmitters to increase the bit rate is constantly being conducted. However, inherent characteristics of the semiconductor devices such as capacitance, chirp and dispersion effects in the optical fiber limit the potential gains that can be obtained.

A very popular alternative is wavelength division multiplexing (WDM), in which high bit rate information carried on several independent wavelength channels is transmitted through a single optical fiber. By adding more wavelengths to the system, the capacity can be increased without the need to lay additional fiber. Such a system is illustrated in Fig. 1.1, in which N wavelengths are combined by a multiplexing element and then transmitted through a common fiber cable. At the destination, the wavelengths are separated by a wavelength demultiplexer and sent to separate photodetector receivers.

WDM has been a major advancement for fiber transmission systems and is generally seen to be a feasible method to meet society's demands. To maximize the capacity of these networks, attempts are being made to send an ever increasing number of channels through the optical fiber. However, the range of wavelengths used is currently limited by the operating amplification range of the EDFA. To increase the channel count, the system wavelengths must therefore be spaced more densely. Long-haul communication systems are being developed which contain over 100 channels with wavelengths being spaced less than 0.4 nm (50 GHz) apart, which are termed "dense WDM" or "DWDM" systems. The tolerances of components operating in these high capacity networks are continually becoming more stringent as channel counts increase. Thus, substantial research activity has been directed towards the development of high

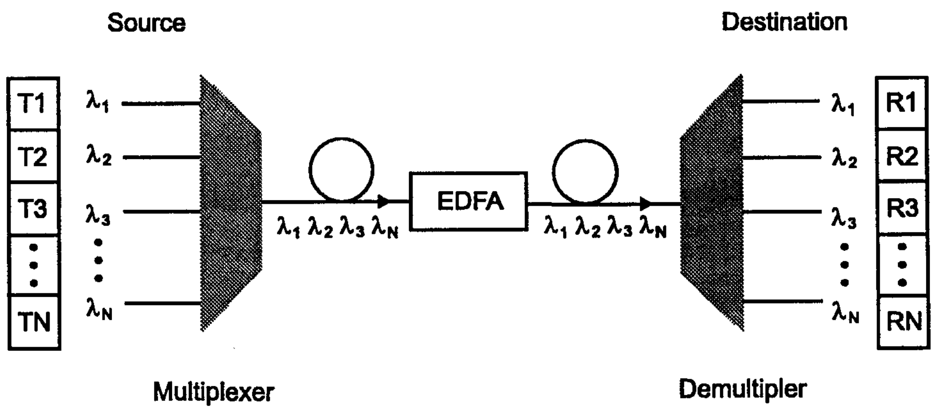

Figure 1.1: Schematic of an N-channel optical communication system utilizing WDM. TN and RN represents the N'th laser transmitter and receiver, respectively.

performance optoelectronic devices which can meet these demands.

1.2 The Need For Wavelength Monitoring

As the sophistication of optical systems increases, components to monitor the network's operation and performance become progressively more important. The monitoring of DWDM channels has become a required function to minimize network down time and to anticipate future problems [3, 4]. Two of the more critical parameters that require monitoring are the power and wavelength of the individual channels. Channel power is affected by many factors including: transmitter output power, insertion loss, polarization dependent loss and amplifier gain. The channel positions are determined by the laser diode wavelengths, which are known to drift over time [5, 6]. Wavelength drifts resulting from effects such as temperature variations, changes in the drive currents and aging, can significantly degrade system performance. If these wavelengths drift beyond their designated tolerances, they will not only contribute towards their own failure, but to that of neighboring channels as well. For DWDM applications, a typical wavelength tolerance of 10% of the channel spacing is set to maintain low inter-channel crosstalk. For 50 GHz systems this tolerance is very tight, being on the order of $\pm$ 20 pm. Therefore, wavelength monitoring instruments must be capable of providing this degree of resolution.

Tunable diode lasers are now being developed to increase the flexibility of WDM networks. These components offer a desirable means to supply fail-safe operation in a system if a given transmitter fails. If this should occur, a tunable laser integrated into the network is activated and set to operate at the necessary wavelength. Without the use of these devices, back-up lasers at every channel wavelength must be present, increasing the cost and complexity of the individual transmitter modules.

The wavelengths in a WDM system can be measured either directly at the individual laser diodes (before being multiplexed) or during transit through the network. In the first case, an individual wavelength monitor is required for each laser transmitter. Since there can be hundreds of wavelengths present, it is important that the monitoring instruments be compact and inexpensive. A convenient and highly desirable means to satisfy this requirement is through the use of transmitters containing monolithically integrated wavelength/power monitors, as illustrated in Fig. 1.2. Fabrication of such a device on a common optoelectronic "chip" significantly reduces the overall cost of the module and offers many important benefits over discrete or hybrid components. These include simultaneous fabrication, decreased insertion loss, significant reduction in module size, lowered parasitics and the elimination of high precision optical alignment, commonly performed manually.

For tunable lasers, the need for wavelength monitoring is even more pronounced. Monitors must be able to function over a span encompassing the laser's tuning range, which can be over tens of nm. Recently, there has been significant work performed on the development of tunable diode lasers containing back-facet wavelength monitors, most of which has focused on the development of hybrid devices, containing various discrete components. This is largely due to the lack of high performance and reliable wavelength monitoring devices that are capable of being monolithically integrated with a laser diode. However, there has been a limited number of reported attempts [7, 8], but in general they have exhibited poor performance with low wavelength resolution.

In the case where WDM system wavelengths are to be measured after being multiplexed, it is beneficial for a wavelength monitor to be capable of functioning with

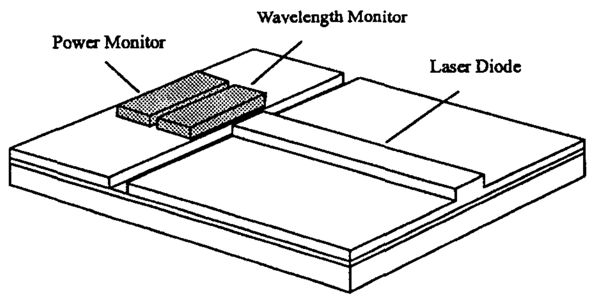

Figure 1.2: Schematic of a laser transmitter with an integrated wavelength and power monitor.

multiple input signals. If this poses a problem, a demultiplexer may be utilized to separate the wavelengths and send them to individual monitoring elements. In this scheme, a device which offers the potential for monolithic integration with the demultiplexing component would be advantageous.

Another field of growing interest is optical sensing based on fiber Bragg gratings [9]. One of the driving forces behind this technology is the development of "smart-structures," which are physical structures that have the ability to sense local changes in their environment, via an internal sensor network. If a fiber Bragg grating (FBG) is embedded within such a structure, it can function as an effective sensing element. When illuminated with a broadband optical source, a FBG acts as a spectral filter that will reflect a very narrow band of the incident wavelength spectrum [10]. When subjected to strain or temperature fluctuations, the center wavelength of its reflection will shift and by detecting this shift, the strain in a structure may be determined [9]. These applications require a sensitive wavelength monitor capable of providing near picometer wavelength resolution, over an operating range of several nanometers. Recently, there has been substantial work directed towards the development of compact, high performance devices for this purpose with no preferred technique being yet established.

1.3 Existing Technologies

There are many ways to determine the wavelength of an optical signal. Traditional technologies such as interferometers and monochromators have existed for many years and can provide accurate, reliable operation. However, these instruments are usually confined to the laboratory as they require precision optical alignment and utilize a large working area.

Optical spectrum analyzers (OSAs) have been specifically adapted for use with fiber optic systems and are currently the conventional technology for analyzing the spectral properties of semiconductor and fiber components [4]. Most optics laboratories now contain these instruments, which usually have a connectorized fiber input and a visual display of the signal spectrum. They can be based on one of many designs, the most common of which utilizes a fixed detector element and a rotating grating to spectrally disperse the signal. Despite their popularity, there are many undesirable features associated with these instruments. The presence of moving parts in the grating's tuning motor makes the technique sensitive to mechanical vibrations and shock. They are also very prone to wavelength drift and frequent calibration is required. Furthermore, the relatively slow scanning mechanism of the device makes it unsuitable for applications that demand the simultaneous monitoring of several incoming signals, or that involve rapidly varying wavelength shifts.

Optical spectrum analyzers are a very bulky and expensive technology and are therefore not a practical candidate for field deployment. A broad range of compact, "low cost" alternatives have recently been reported, which offer a more feasible solution for integration into current systems. These include the use of semiconductor devices, bulk optical filters and various fiber components. The reported fiber-based devices have primarily been developed for FBG sensor applications as they are well adapted for use with these systems. Interferometeric schemes have been demonstrated using a variety of configurations [11, 12, 13, 14]. These devices can provide high wavelength sensitivity, but generally suffer from high temperature dependence and require moving parts or piezoelectric elements, which are expensive and prone to drift.

Passive devices utilizing the wavelength dependent transfer functions of WDM couplers [15, 16], bulk optic spectral filters [17] and biconical fiber filters [18] have also been reported. The filtering techniques commonly utilize two photodetectors placed at the ends of a fiber power splitter, with the wavelength dependent element being placed in one arm. The ratio of the two detector signals is then taken as a power independent measure of wavelength. In addition to being composed of many discrete components, these passive techniques suffer from an inherent trade-off between resolution and measurement range.

Active monitoring schemes employing tunable fiber Fabry-Perot filters [19] and acousto-optic tunable filters [20] have also been presented. These approaches rely on tuning the center wavelength of a filter to maximize the transmission of an incoming signal. They allow a large operating range to be obtained without compromising their sensitivity. However, these schemes are generally very complicated and the active filters are presently very expensive.

The numerous advantages offered by optoelectronic semiconductor devices makes them a very attractive technology for wavelength monitoring applications. Currently, there has only been a modest amount of work published on this subject, but due to the increasing complexity of WDM networks and the growing interest in FBG sensors, research activity in this area is increasing. Monitoring schemes utilizing semiconductor waveguide interferometers [21] and wavelength dependent splitters [7] have been reported for use near 1.55 μm. The first scheme requires relatively difficult fabrication procedures and is based on interference fringe counting. Fringe counting schemes are generally very temperature sensitive and are usually restricted to the measurement of wavelength shifts rather than providing absolute measurement. In the second approach, a relatively poor wavelength resolution was obtained over a limited operating range.

The unique properties of quantum well structures have also been exploited for wavelength monitoring applications [22, 23]. These approaches utilize surface-illuminated photodetectors and the quantum confined Stark effect to tune the absorption band edge of a quantum well material. Since surface-illuminated geometries are used, a large number of quantum wells is required, complicating and adding to the expense of the wafer growth. In addition, the potential for monolithic integration with waveguide-based devices is limited.

In this thesis, a compact optoelectronic device that utilizes similar principles to the previous two approaches, is presented. However, the operation of the device and its geometry are significantly different. Here, waveguide-based photodetectors containing quantum wells are utilized to function as high precision wavelength monitors over a spectral region centered near 1.55 μm. Waveguide photodetectors offer many important advantages over more conventional surface-illumination schemes, which will be described throughout this thesis. The proposed wavelength monitor uses pairs of in-line waveguide photodiodes fabricated in an InGaAsP on InP material structure. The material structure and waveguide design allow strong potential for monolithic integration with other semiconductor devices, adding to the attractiveness of the technique. Due to the simple nature of the device, it is extremely compact and can be relatively easily fabricated. In addition, the tasks of tunable wavelength filtering, power splitting and photodetection are all performed by a single semiconductor component.

This work originally began with the use of in-line waveguide photodetectors for wavelength monitoring applications near 980 nm, utilizing a GaAs/InGaAs quantum well system. These devices were first demonstrated by Wu *et al.* [24], and then further explored by Densmore and Jessop [25]. This thesis however, will focus on the development of devices for operation near 1.55 μm, where there is considerably more commercial interest. Several unique wavelength monitoring schemes are presented which use the in-line detectors for single [26] and multiple wavelength operation [27]. The critical issue of temperature sensitivity is explored, and a novel temperature compensation scheme is presented to effectively reduce the detector's thermal sensitivity. Finally, the devices are shown to successfully function as key elements in various types of FBG sensors.

1.4 Structure of The Thesis

This thesis contains seven chapters which provide an overview of the theory, design and experimental results obtained during this research project.

Chapter 2 begins with a summary of the theory and concepts needed to describe the operating principles of the proposed device. In particular, the properties of quantum well structures are described, with an emphasis being placed on energy level calculations and optical absorption characteristics. The second half of the chapter reviews basic semiconductor waveguide theory, utilized in the device design.

A review of P-I-N photodetectors is presented in chapter 3. The advantages and disadvantages of using waveguide-based photodetectors over that of more conventional surface illuminated designs, are discussed. In addition, the concept of using pairs of in-line waveguide photodiodes for wavelength monitoring applications is introduced.

Chapter 4 is concerned with the final device design including the results from the energy level and waveguide calculations, the selected semiconductor wafer structure and the chosen device geometry. The second part of the chapter contains a detailed account of the important procedures followed during the device's fabrication. These include photomask design, photolithographic processing, metallization and mounting.

In chapter 5, experimental data are presented regarding the operation of the fabricated devices. The chapter begins by examining the electrical properties and the optical waveguide characteristics of the in-line detectors. The photodetection properties are then considered and the devices are shown to function as high resolution wavelength monitors. Different operating modes and methods to improve the performance of the technique, are presented. Finally, a unique temperature compensation scheme is proposed, which is shown to be an effective means to reduce the detector's thermal sensitivity.

The application of the waveguide photodetectors to the field of fiber Bragg grating sensing is considered in chapter 6. The devices are shown to be a desirable means to provide the critical function of wavelength sensitive detection in these systems. They are used to track the induced wavelength shifts in the reflection spectrum of a FBG that result from the application of strain. Various sensor configurations are demonstrated and their performances are evaluated.

Finally, this thesis concludes with a brief summary of the important results obtained during the research project and suggestions concerning future work are made.

Chapter 2

Design Theory

2.1 Introduction

The design of an optoelectronic device entails many important steps that must be followed to achieve a desired operation. Two of the more critical procedures involve the design of the active region to generate or detect light, and the optical waveguide to direct it to a desired location. The techniques used to model these processes are presented in this chapter. In addition, some of the important physical concepts related to this thesis work are described.

2.2 The Active Region

The properties of the active region of a semiconductor heterostructure are important when one is interested in excitation processes which are usually induced by electrical or optical means. Gain, lasing and photodetection are all based on excitation of the active material. It is therefore critical to develop a clear understanding of the processes that occur in this region. This section describes in detail, the calculation of energy levels in quantum well materials. The use of intentionally introduced strain and applied electric fields are considered and their effects on a material's energy band structure are examined. Emphasis is placed on the InGaAsP quaternary system grown on InP.

2.2.1 Material Properties of InGaAsP

$In_{1-x}Ga_xAs_yP_{1-y}$ on InP has become the material system of choice for III-V telecommunication components operating near 1.3 μm and 1.55 μm. This can largely be attributed to the broad possible tuning range of its energy band gap about these wavelengths. The use of a quaternary is desirable as it offers the benefits of having two compositional degrees of freedom. This allows for the independent tailoring of both lattice constant and material band gap.

InGaAsP may be thought of as being composed of four binary constituents: InP, GaAs, InAs and GaP. The material parameters of these binary compounds have been extensively studied [28]. However, the parameters for InGaAsP have not been rigorously reported and estimation techniques are often required. A linear interpolation scheme between the binary constituents can be used to deduce certain material properties. For $In_{1-x}Ga_xAs_yP_{1-y}$, the generic material parameter Q(x,y) is estimated using:

$$Q(x,y) = (1-x)yQ_{InAs} + (1-x)(1-y)Q_{InP} + xyQ_{GaAs} + x(1-y)Q_{GaP} \tag{2.1}$$

where Q_B (B=InP, GaAs, InAs, GaP) is the corresponding binary value. Table 2.1 lists some of the important binary material parameters used in this thesis.

The accuracy of the interpolation scheme depends on the material parameter being investigated. It provides a rough estimate only and is commonly used when more detailed empirical models are not available. For a more comprehensive discussion of this method and its applicability to specific material properties see Refs. [28, 29].

A linear interpolation is not justified for properties that behave nonlinearly with alloy composition, such as the material's band gap. In this thesis, the empirical model presented by Kuphal [32] is utilized for the calculation of the band gap energy of lattice matched $In_{1-x}Ga_xAs_yP_{1-y}$ on InP. This model has been successful in accurately fitting photoluminescence data over the entire As composition range and can be summarized

Parameter	Symbol	GaAs	GaP	InAs	InP
Lattice Constant[1] (Å)	a	5.6533	5.4512	6.0584	5.8688
Direct Energy Gap[2] (eV)	E_g	1.424	2.78	0.354	1.344
Luttinger Parameters[2]	γ_1	6.85	4.05	20.4	4.95
	γ_2	2.1	0.49	8.3	1.65
Elastic Constants[1]	C_{11}	11.88	14.120	8.329	10.225
($10^{11} dyn/cm^2$)	C_{12}	5.38	6.253	4.526	5.765
Deformation Potentials[3]	a	-9.77	-9.6	-6	-6.35
(eV)	b	-1.7	-1.65	-1.8	-2
Electron Effective Mass[1]	m_e/m_o	0.067	0.17	0.023	0.077

Table 2.1: Material parameters used for binary constituents. 1, 2, 3: parameters taken from Refs. [29], [30] and [31] respectively.

as follows:

$$E_g(x,y) = 1.35 + 0.668x - 1.068y + 0.758x^2 + 0.078y^2 - 0.069xy - 0.322x^2y + 0.03xy^2 \tag{2.2}$$

where $E_g(x,y)$ represents the quaternary band gap at 300 ^{o}K and is measured in eV.

In order to model the waveguiding characteristics of a device the refractive index of all regions that significantly interact with the optical field must be known. The refractive index is strongly dependent on material composition, temperature and photon energy. Many models have been proposed to describe the refractive index of the $\mathrm{In_{1-x}Ga_xAs_yP_{1-y}}$ material system [29]. Certain techniques have strengths and weaknesses over others. Some provide greater agreement with experimental values over a given composition range, while others may be better over a certain photon energy range.

The model by Pettit and Turner [33] accurately describes the refractive index of the binary InP over a wavelength range extending approximately from 1-2 μm. Their empirical relation is given as:

$$n_p{}^2 = 7.255 + \frac{2.316\lambda^2}{\lambda^2 - 0.3922 \times 10^8} \tag{2.3}$$

at 298 ^{o}K with the wavelength λ, having units of Å.

To predict the refractive index of the quaternary $\mathrm{In_{1-x}Ga_xAs_yP_{1-y}}$, lattice matched to InP, the method of Burkhard et. al. [34] is used. This approach is based on an interpolation of atomic polarizabilities and can be expressed as:

$$n_p(\Delta E, y) = 3.425+0.94\Delta E+0.952\Delta E^2+(0.255-0.257\Delta E)y-(0.103-0.092\Delta E)y^2 \tag{2.4}$$

The energy separation ΔE, is defined as the difference between the photon energy and the energy band gap of the quaternary ($\Delta \mathrm{E} = \mathrm{E_{photon}} - \mathrm{E_g}$), and is expressed in units of eV. This method has demonstrated strong agreement with experimental data over a photon energy range satisfying the condition, -0.2 eV $\leq \Delta$E < 0.

As will be discussed in chapter 4, it will also be necessary to calculate the refractive index of strained quaternaries. The method of Burkhard et. al. is again used for this purpose, with the addition of a correction factor to account for the effects of strain. This will be discussed further in Sec. 4.1.1.

2.2.2 Quantum Well Analysis

Efficient semiconductor devices utilize potential wells to provide carrier confinement. Currently, the most widely used material systems for photonic applications form type I heterostructures. These structures consist of a smaller band gap layer sandwiched between two larger band gap materials to produce potential wells in both the conduction and valence bands (see Fig. 2.1). This type of system not only offers the advantage of carrier confinement but is beneficial for optical waveguiding as well. The smaller energy gap in the well layer provides a region of increased refractive index, which as will be discussed below, is necessary for optical confinement.

If the width of the center, low band gap region decreases to the order of an electron wavelength quantum effects become apparent and eventually dominate the

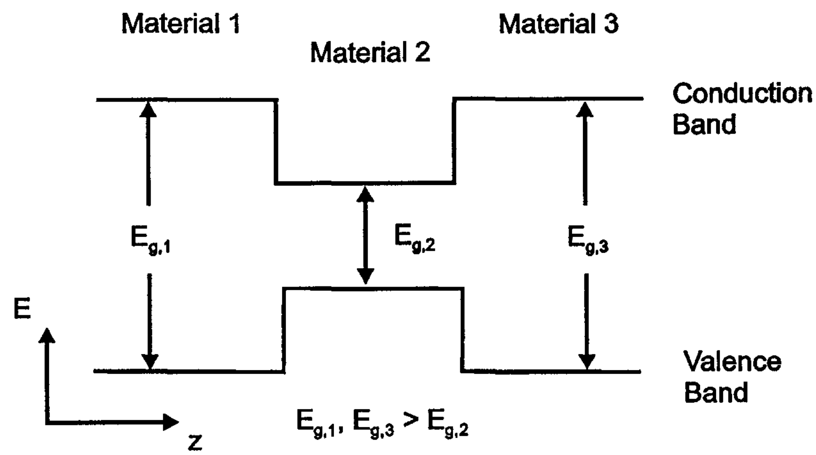

Figure 2.1: A type I semiconductor heterostructure formed by growing a smaller band gap material between two larger band gap layers. Band bending effects at the heterojunction interfaces are ignored.

electrical and optical behavior of the system. This structure termed a quantum well, is very useful for active region design and is utilized in many optoelectronic devices, including electroabsorption modulators, infra-red detectors and quantum well lasers. The analysis presented below is based on the procedures described in Refs. [30, 35].

Conduction Band Solutions

An electron trapped in a quantum well can be viewed as a charge carrier that can effectively "see" both potential barriers that define the well. It will begin bouncing off of the well walls which will create a standing wave type wavefunction. This leads to the familiar "particle in a box" type situation encountered frequently in quantum mechanics.

If the heterojunction layers are orientated to lie in the x-y plane, the z component of the electron's motion is confined to the well region (neglecting tunnelling). The effective mass equation for electrons in the conduction band, of energy E_c(z) can be expressed as:

$$[\frac{{p_x}^2 + {p_y}^2}{2m^*} + \frac{{p_z}^2}{2m^*} + E_c(z)]\Psi = E\Psi \tag{2.5}$$

where p_x, p_y and p_z are the x, y and z components of the momentum of the electron, E is the total electron energy, m^* is the average electron effective mass, and Ψ is the electron wavefunction. The carrier confinement in a quantum well is in the z-direction only. The electron's motion in the x-y plane is not confined and it behaves as a charge carrier of effective mass m^* in a constant potential. Therefore, a plane wave solution can be assumed to describe the electron in the plane of the quantum well layer. The total wavefunction can then be written:

$$\Psi = e^{i(k_x x + k_y y)}\varphi(z) \tag{2.6}$$

where $\varphi(z)$ denotes the component of the electron's wavefunction in the z-direction. Substituting this result into Eq. 2.5 yields:

$$[\frac{{p_z}^2}{2m^*} + E_c(z)]\varphi = E_z\varphi \tag{2.7}$$

and

$$E = \frac{\hbar^2({k_x}^2 + {k_y}^2)}{2m^*} + E_z \tag{2.8}$$

Eq. 2.8 expresses the result that the total electron energy can be split into two components, corresponding to the bound and unbound parts of the electron's motion. To solve Eq. 2.7, two models of the quantum well are usually examined: the infinitely deep well and the finite well.

In the infinitely deep well approximation, the solution of Eq. 2.7 is relatively straightforward, as the wavefunction must be zero in the confining layer and also at the heterojunction interface. Taking the well bottom E_c, to be zero and the layer interfaces to be located at 0 and L, the general solution in the well region is given as:

$$\varphi(z) = Ae^{ik_z z} + Be^{-ik_z z} \tag{2.9}$$

and we obtain the familiar results for a particle in a box [36]:

$$\varphi_n = \sqrt{\frac{2}{L}} sin(\frac{n\pi z}{L}) \tag{2.10}$$

$$E_{z,n} = \frac{\hbar^2}{2m^*}(\frac{n\pi}{L})^2 \tag{2.11}$$

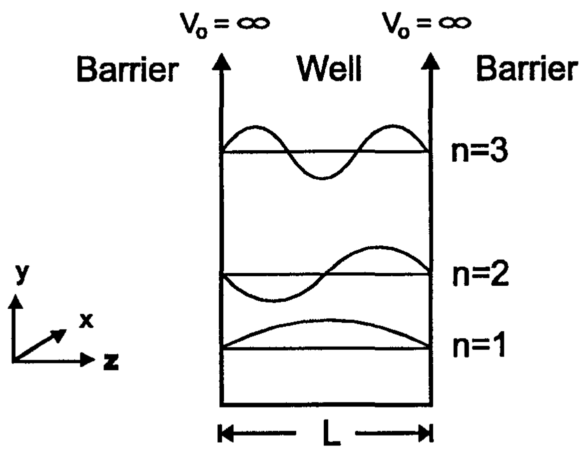

Figure 2.2: Electron wavefunctions and energy levels drawn under the infinitely deep well approximation.

where n is any integer. Eqs. 2.10 and 2.11 show the standing wave nature of the electron wavefunction and the effect of confinement upon its energy. By confining the electron, the energy spectrum will consist of a series of discrete energy levels as seen in Fig. 2.2.

In the finite well case, the well depth is taken to be a finite value V_o. It is convenient to define the origin (z=0) at the well center and the potential function V(z) is then taken to be zero within the low band gap region and equal to V_o for $|z| \geq L/2$. In the well, the electron wavefunction has a standing wave form as in the infinite well case, but now the electrons are able to penetrate the barriers. The wavefunction can be found by solving the Schrödinger equation:

$$[-\frac{d}{dz}\frac{1}{m^*}\frac{d}{dz} + V(z)]\varphi(z) = E\varphi(z) \tag{2.12}$$

where m^*=m_w in the well and m^*=m_b in the barrier regions. For bound states, the even wavefunction solutions have the form:

$$\varphi(z) = \begin{cases} Ae^{-\alpha(|z|-L/2)} & |z| \geq \frac{L}{2} \\ B\cos(kz) & |z| < \frac{L}{2} \end{cases} \tag{2.13}$$

where

$$k = \frac{\sqrt{2m_w E}}{\hbar} \tag{2.14}$$

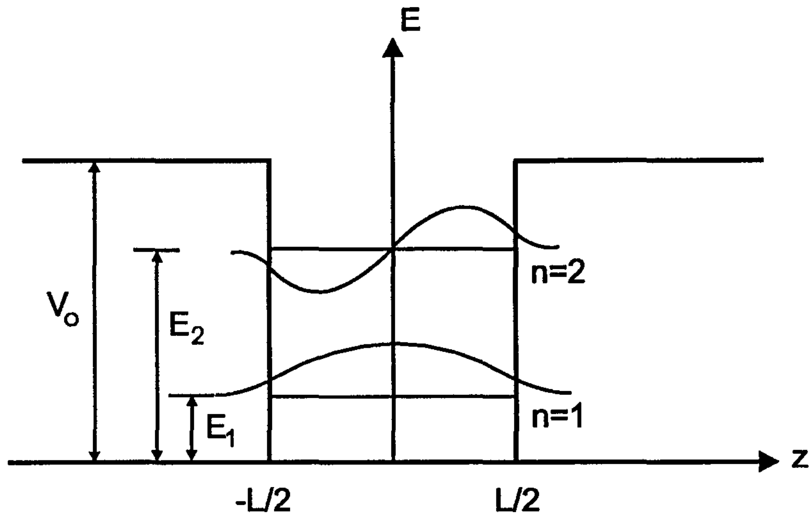

Figure 2.3: First two bound energy levels and wavefunctions in a finite barrier quantum well.

$$\alpha = \frac{\sqrt{2m_b(V_o - E)}}{\hbar} \tag{2.15}$$

and the condition that φ(z) must remain finite as $|z| \to \infty$ is used. Eq. 2.13 shows that the electron is able to penetrate partially into the well wall, where its wavefunction decays exponentially. This can be seen in Fig. 2.3 where the first two bound energy states are displayed for the finite well case. By using boundary conditions that state that φ and $(1/m^*)\ \partial\varphi/\delta z$ must be continuous across the well walls, the constants A and B can be related:

$$A = B\cos\frac{kL}{2} \tag{2.16}$$

$$\frac{\alpha}{m_b}A = \frac{k}{m_w}B\sin\frac{kL}{2} \tag{2.17}$$

The eigenvalue equation for even solutions, can then be obtained from Eqs. 2.16 and 2.17:

$$\alpha = \frac{m_b k}{m_w}\tan(\frac{kL}{2}) \qquad \textit{even solutions} \tag{2.18}$$

The odd wavefunction solutions can be found by following a similar procedure, yielding:

$$\varphi(z) = \begin{cases} Ae^{-\alpha(z-L/2)} & z > \frac{L}{2} \\ B\sin(kz) & |z| \leq \frac{L}{2} \\ -Ae^{\alpha(z+L/2)} & z < -\frac{L}{2} \end{cases} \tag{2.19}$$

The eigenvalue equation is again obtained by using the boundary conditions and can be written:

$$\alpha = -\frac{m_b k}{m_w}\cot(\frac{kL}{2}) \qquad \textit{odd solutions} \tag{2.20}$$

Eqs. 2.18 and 2.20 can be solved to find the eigenenergies E_n's, of the finite quantum well. Unfortunately, there is no exact solution to these equations and graphical or numerical methods must be used [30].

As seen in Eq. 2.5, the total electron energy can be divided into two components corresponding to the electron's motion parallel and perpendicular to the heterojunction interface. It was shown that the electron's energy in the z-direction was split into a series of discrete energy levels, which does not imply however, that the total energy of the electron is quantized. For each value of E_z, the electron has a continuous range of energies in the x-y plane which gives rise to a series of "minibands" (or "sub-bands") of allowed energies, as shown in Fig. 2.4. The energy of the sub-bands as a function of wavevector form parabolas with minima located at the quantized E_z values.

This sub-band energy structure gives rise to an important form of the density of states function:

$$\rho_{2D} = \frac{m^*}{\pi\hbar^2} \tag{2.21}$$

Eq. 2.21 expresses the density of states for a single sub-band and illustrates that this quantity is independent of energy. The total density of states at a given energy E, is then given by the product of Eq. 2.21 and the number of different k_z states at that energy. This leads to a two dimensional density of states showing discontinuities at each E_z value with a "step-wise" form. This result is compared with the well known three dimensional case,

$$\rho_{3D} = \frac{\sqrt{2m^{*3}}}{\pi^2\hbar^3} \tag{2.22}$$

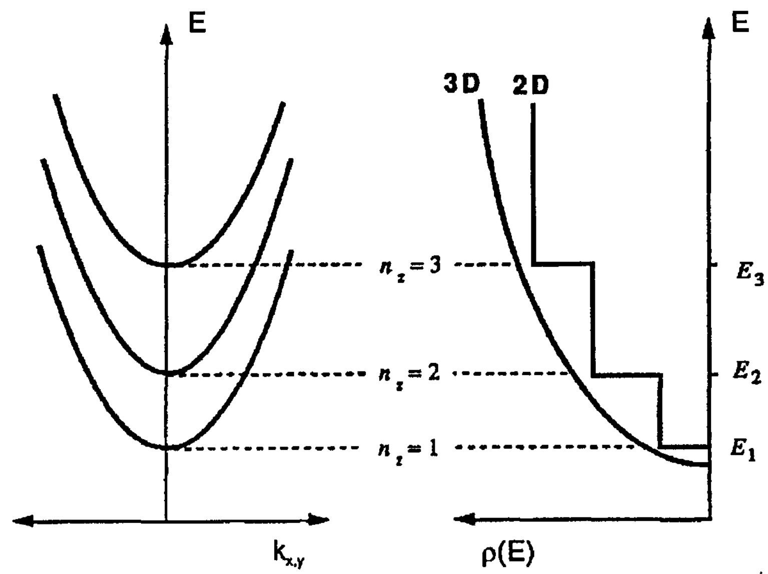

Figure 2.4: (left) The construction of the total energy of an electron in the conduction band of a quantum well with total energy E. (right) A comparison of the two and three dimensional density of states. In the case of the infinite well approximation, each step touches the three dimensional curve.

in Fig. 2.4.

The density of states function is an important factor in determining the optical absorption and emission properties of a material. Due to the rapid jump at the sub-band energies, the absorption band edge of the 2-D structure is expected to be much sharper in energy than that of a bulk material. As will be described in the next chapter, this is one of the key motivations for using devices containing active quantum wells rather than bulk layers.

Valence Band Solutions

The above discussion considered electrons bound in a quantum well formed in the conduction band. A similar problem deals with holes trapped in the well formed in the valence band. The argument in this situation can be much more complicated as the bulk light hole and heavy hole bands are degenerate at k=0, and interaction between

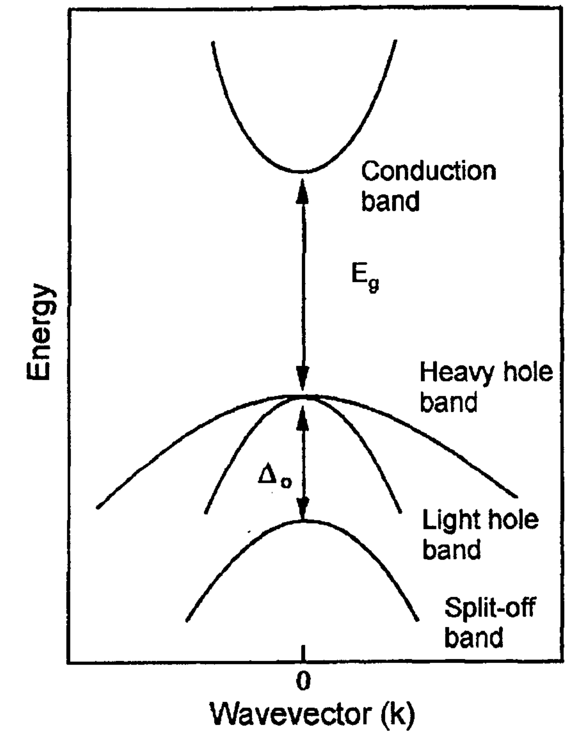

Figure 2.5: Conceptual view of a typical energy band structure of a III-V bulk semiconductor compound. The heavy and light hole bands are seen to be degenerate at k=0. The direct energy gap E_g and the split-off band are shown.

bands can be relatively strong. This is illustrated in Fig. 2.5, which displays the band diagram for a typical bulk III-V semiconductor compound. The potential well depth V_o in this case, is the valence band offset whose value is currently under considerable debate. For InGaAsP, the band offsets are taken to be 35% and 65% of the total energy gap difference between the well and barrier materials for the conduction band and valence band, respectively. These values were taken from Refs. [28, 35].

Since the energy level solutions depend on the effective mass of the trapped carriers, the effect of quantization will break the degeneracy of the heavy hole and light hole levels. The split-off band is located at an energy significantly lower than the low lying heavy and light hole levels and only needs to be considered when interested in energy levels deep into the valence band. Defining the zero energy point to be at the bottom of the valence band well, the heavy hole levels will lie at lower energy states than those associated with the light holes. This reduces the band-to-band interaction at **k**=0. As will be discussed below, the effects of using strained layers can further reduce the coupling between bands. At **k**=0, the heavy and light hole levels can then be treated independently using the same analysis presented above. The hole effective masses along the growth direction at the band edge are given as:

$$m_{hh} = \frac{1}{\gamma_1 - 2\gamma_2}$$
$$m_{lh} = \frac{1}{\gamma_1 + 2\gamma_2} \tag{2.23}$$

where the constants γ_1 and γ_2 are the Luttinger parameters of the material.

To obtain the complete dispersion relations away from **k**=0, more complex methods are required. A summary of these can be found in Refs. [37] and [38]. Since this work is primarily concerned only with the band edge energies, such methods will not be discussed here.

2.2.3 Energy Levels Under Strain

The use of strained material layers can have a drastic effect on the electrical and optical properties of photonic devices. It can be a useful means to improve and tailor device performance. The strain is introduced by growing a layer which has a slightly mismatched native lattice constant relative to that of the underlying material. If the strained layer is grown below a critical thickness h_c, the mismatch is usually accommodated through a uniform elastic deformation of its crystal structure. The underlying material is assumed to be thick enough to be unperturbed by the growth of this strained layer.

The critical thickness is estimated to be 200 Å for the devices described in this thesis, using the expression of Matthews and Blakeslee [39], [40], for a -1% compressive strain. For thicknesses greater than this value, it is energetically favorable for the lattice mismatch to be accommodated through the formation of misfit dislocations. These dislocations destroy the lattice periodicity and tend to act as non-radiative recombination centers which can be detrimental to device performance [30]. The strained layers used in this work form the quantum well regions and have ~ 50 Å thickness, well below h_c. They are therefore treated as ideal elastically strained materials. Assuming the crystal growth direction is along the z-direction, the in-plane (biaxial) strain for $In_{1-x}Ga_xAs_yP_{1-y}$ grown on InP, is given by:

$$\varepsilon = \varepsilon_{xx} = \varepsilon_{yy} = \frac{a_{InP} - a_{qw}}{a_{InP}} \tag{2.24}$$

where a_{InP} is the native lattice constant of InP and a_{qw} is the bulk lattice constant of $In_{1-x}Ga_xAs_yP_{1-y}$. For compressive strain, we have $a_{qw} > a_{InP}$, and ε is negative. The lattice constant mismatch will also induce strain perpendicular to the growth direction:

$$\varepsilon_{zz} = -2\frac{C_{12}}{C_{11}}\varepsilon \tag{2.25}$$

where C_{11} and C_{12} are the elastic stiffness constants of the quantum well layer.

Eq. 2.2 cannot be used directly to calculate the energy band gap of a strained quaternary. The effect of strain on the band structure must be considered. The strain perturbation is obtained using the interpolated values of the elastic constants C_{11} and C_{12}, deformation potentials a and b, and the lattice constant a_{InP} given in table 2.1. The band gap of the strained material can then be found by including correction terms to account for the strain induced effects. The band edge energies are [35]:

$$E_{c-hh} = E_g(unstrained) - \delta E_{hy} + \frac{1}{2}\delta E_{sh} \tag{2.26}$$

$$E_{c-lh} = E_g(unstrained) - \delta E_{hy} - \frac{1}{2}\delta E_{sh} \tag{2.27}$$

where E_g(unstrained) represents the band gap of the unstrained quaternary (having units of eV), and the correction terms δE_{hy} and δE_{sh} arise from the hydrostatic and shear components of the strain. The correction factors are defined as:

$$\begin{aligned} \delta E_{hy} &= -2a[1 - \frac{C_{12}}{C_{11}}]\varepsilon \\ \delta E_{sh} &= -2b[1 + 2\frac{C_{12}}{C_{11}}]\varepsilon \end{aligned} \tag{2.28}$$

Eqs. 2.26 and 2.27 illustrate the effects of mismatched strain on a material's band structure. The hydrostatic component of a biaxial strain shifts the positions of the conduction and valence band edges to cause an overall change in band gap, by an amount equal to δE_{hy}. This is a positive increase for compressive strain and negative for tensile strain. The partition of the hydrostatic shift between the valence and conduction bands is taken as follows: two thirds of the total band gap shift is attributed to the conduction band shift δE_c and one third to the shift of the valence band levels $\delta E_{hh}, \delta E_{lh}$, following [35]:

$$\begin{aligned}
\delta E_c &= -\frac{2}{3}\delta E_{hy} \\
\delta E_{v(hh)} &= \frac{1}{3}\delta E_{hy} - \frac{1}{2}\delta E_{sh} \\
\delta E_{v(lh)} &= \frac{1}{3}\delta E_{hy} + \frac{1}{2}\delta E_{sh}
\end{aligned} \tag{2.29}$$

Eqs. 2.26- 2.27 also illustrate the effects of the shear component of strain. It is shown to act to increase the energy level separation of the light and heavy hole bands in the quantum well layer by an amount equal to δE_{sh}. This shift is positive for the light hole band (taking zero to be the bottom of the valence band well) and to be negative for the heavy hole levels. As will be discussed in the next section, this is an important consequence of strain, as the shear component significantly separates the absorption band edges for transverse electric (TE) and transverse magnetic (TM) polarized light.

2.2.4 Optical Properties of Quantum Wells

Intrinsic Optical Properties

The nature of the interband optical transitions is fundamental for determining the optical properties of a material. In direct gap, unstrained quantum well structures, the minimum energy needed to send an electron from the valence band to the conduction band is

$$E_{g,\text{ quantum well}} = E_{g,\text{ bulk}} + E_{c,\, n=1} + E_{hh,\, n=1} \tag{2.30}$$

ignoring exciton effects (which will be discussed below). E_c and E_{hh} are the energies of the lowest confined electron and heavy hole states, respectively. The lowest heavy hole state is chosen as opposed to the lowest light hole state as its energy lies closer to the top of the valence band due to the greater effective mass. From Eqs. 2.18 and 2.20, it is seen that the energies E_c and E_{hh} are dependent on the width and depth of the quantum well. This gives wafer growers two more degrees of freedom by which to tailor the band gap.

The energy transitions in a quantum well are subject to the selection rule $\Delta n = n_h - n_e = 0$, where n_h and n_e denote the quantum numbers of the bound valence band hole levels and the conduction band electron levels, respectively [41, 37, 42]. This transition rule can be qualitatively explained by noting the similarity of electron wavefunctions of the same quantum number n. Electron states with the same n value have the same number of nodes in their wavefunction which leads to the greatest amount of wavefunction overlap. This in turn results in the greatest transition probability. To obtain a more quantitative viewpoint, time dependent perturbation theory can be applied. Such an analysis yields an expression for the transition rate of an electron between a single pair of conduction and valence band states, commonly referred to as "Fermi's golden rule" [41, 30]. The downward transition rate can be written as:

$$W_{e \to h} = \frac{\pi q^2}{m_o \omega \varepsilon} \delta(k_h - \beta - k_e) |M_T|^2 \delta(E_c - E_v - \hbar\omega) \tag{2.31}$$

where β, k_h and k_e represent the photon, hole and electron wavevectors, respectively. ω is the angular frequency of the photon and M_T is known as the transition matrix element. The delta function $\delta(k_h - \beta - k_e)$, reflects the momentum conservation that is necessary for a transition to occur. The momentum of a photon is typically much smaller than that of an electron and is commonly ignored. This leads to a restriction for allowed optical transitions known as the Δk=0 ($k_h - k_e$=0) selection rule. The second delta function in Eq. 2.31 illustrates that the created photon must have an energy equal to $E_c - E_v$ in order to conserve energy.

The transition matrix element is an important factor and can be shown to be proportional to the overlap integral of the electron and hole wavefunctions [30, 41]. This leads to the $\Delta n = 0$ selection rule described above. Fermi's golden rule can also be used to determine the polarization dependence of the allowed optical transitions. The transition probability $|M_T|^2$ can be shown to be proportional to the factors $(1 - |\hat{\mathbf{k}} \cdot \hat{\mathbf{e}}|^2)$ and $(1/3 + |\hat{\mathbf{k}} \cdot \hat{\mathbf{e}}|^2)$ for the transitions to the conduction band from the heavy hole and light hole bands, respectively [41]. $\hat{\mathbf{k}}$ represents the electron unit k-vector which is assumed to be along the z-axis (growth direction) and $\hat{\mathbf{e}}$ is a unit vector in the direction of the photon polarization. Two common polarization states are defined for optical fields travelling in a direction parallel to the plane of a quantum well layer. Transverse electric (TE) polarization is defined as light with its electric field vector pointing in a direction parallel to the quantum well plane ($\hat{\mathbf{e}} = \hat{\mathbf{y}}$) for light propagating in the x-direction). Conversely, transverse magnetic (TM) polarization is defined as light with its magnetic field vector pointing along the plane of the layer. In this situation $\hat{\mathbf{e}} = \hat{\mathbf{z}}$.

The above discussion indicates that all transitions to the heavy hole band will be TE polarized while transitions to the light hole band will be four times more likely to produce TM polarized light than TE. In terms of optical absorption, TM light will induce transitions from the light hole to conduction band only. Conversely, absorbed TE light will induce transitions to the conduction band from both the heavy and light hole bands with the heavy hole transitions being three times more likely to occur. These results are summarized in Fig. 2.6.

Transitions that do not follow the above selection rules do however, have a finite probability of occurring. This is due to the fact that the overlap integral between the electron and hole wavefunctions is not strictly zero for $\Delta n \neq 0$ in finite wells. This results from the different effective masses of the carriers which determines the penetration of the wavefunctions into the barrier material. These processes are usually weak and are termed "forbidden".

Extrinsic Optical Properties

In the above discussion, we have ignored any interaction between the excited carriers. In reality, the situation is slightly more complex as conduction band electrons can become bound with valence band holes through their attractive Coulomb poten-

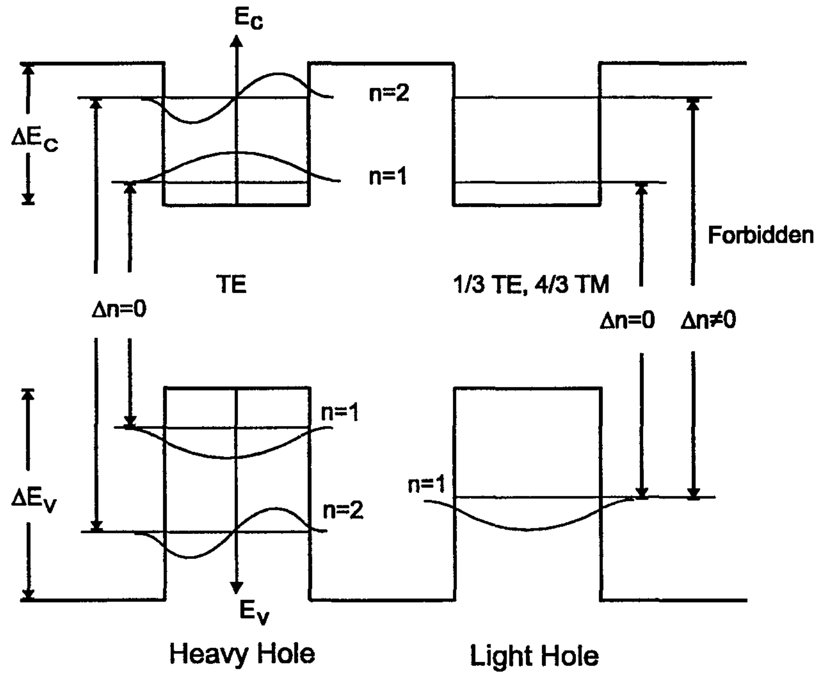

Figure 2.6: Optical transitions between conduction band electrons and valence band holes demonstrating the $\Delta n = 0$ selection rule. ΔE_c and ΔE_v represent the conduction and valence band offsets, respectively. The polarization dependence is also illustrated. For clarity, the heavy and light hole levels have been horizontally separated.

tials. The bound electron-hole pairs, known as "excitons", can significantly alter the optical properties of a material. Due to their binding energy, excitons introduce lower lying energy levels into the semiconductor band structure [43]. As a result, electrons are able to absorb photons having energies less than the band gap values calculated above. The band edge will appear "red-shifted" by an amount equal to the exciton binding energy ${E_n}^{ex}$.

In quantum well structures, the overlap integral (and consequently M_T) of the bound electron-hole states, can be very large. As a result, band-to-exciton transitions tend to dominate the 2-D absorption spectrum. Exciton states exist near the sub-band minima (k=0), which results in a series of strong absorption peaks concentrated near the sub-band energy levels. These effects are conceptually illustrated in Fig. 2.7. Fig. 2.8 displays experimental absorption data for a 100 Å thick GaAs/AlGaAs quantum well for various allowed and forbidden transitions.

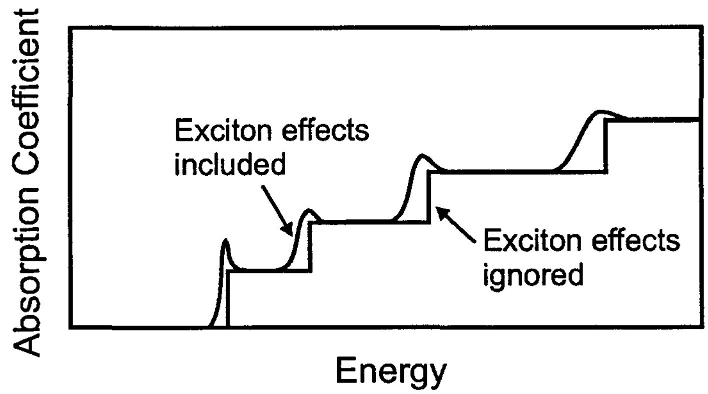

Figure 2.7: The behavior of the absorption coefficient of a quantum well sample versus energy for the cases of exciton effects included and ignored.

The three dimensional, ground state binding energy of an exciton can be written [30]:

$$E_{3D}{}^{ex} = \frac{m_r{}^* e^4}{2\hbar^2(4\pi\varepsilon)^2} \tag{2.32}$$

where ε is the permittivity of the semiconductor and $m_r{}^*$ is the electron-hole reduced mass. The reduced mass is defined as:

$$\frac{1}{m_r{}^*} = \frac{1}{m_e{}^*} + \frac{1}{m_h{}^*} \tag{2.33}$$

where $m_e{}^*$ and $m_h{}^*$ are the electron and hole effective masses. For bulk GaAs, the binding energy is estimated to be about 4 meV [37].

In bulk crystals, the exciton effects are not nearly as evident as in 2-D structures due to the small binding energy of the 3-D exciton. The reduced dimensionality of the quantum well causes the electron and hole to be held more closely together, thereby increasing the Coulomb force binding the pair. For a bulk semiconductor, the probability that an exciton is ionized is given by the Boltzmann factor $\exp(-|E_{3D}{}^{ex}|/kT)$ where $kT \approx 26$ meV at room temperature. Therefore, excitons have a high probability of being ionized in 3-D materials at room temperature and the chance of observing their emission is very small. At low temperatures, however, 3-D exciton effects become stronger and can be observed. Conversely, the increased binding energy in 2-D structures allows exciton peaks to be clearly seen at room temperature, as shown in Fig. 2.8.

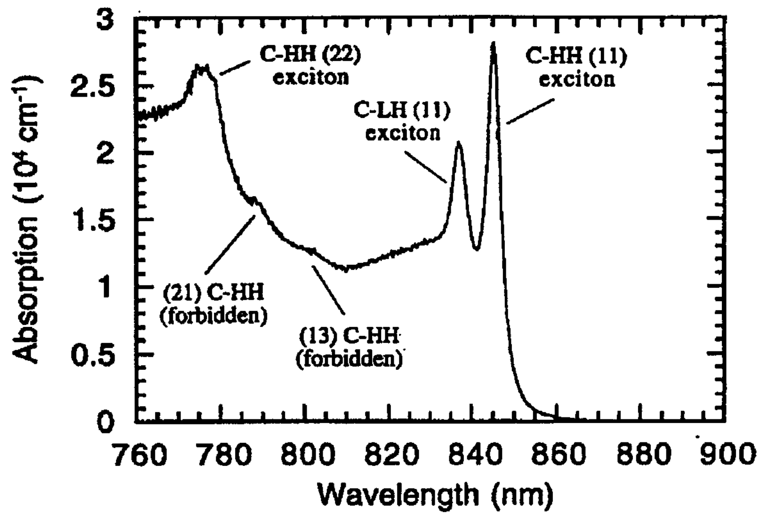

Figure 2.8: Experimental absorption spectrum for a 100Å GaAs/$Al_{0.3}Ga_{0.7}As$ quantum well sample at room temperature [41].

The 2-D binding energy, under the infinite well approximation, is given as:

$$E_{2D}{}^{ex}(n) = E_{3D}{}^{ex}\left[\frac{1}{(n-1/2)^2}\right] \tag{2.34}$$

for transitions involving quantum level n. Under this approximation, the two dimensional ground state (n=1) exciton binding energy is four times greater than the bulk value ($E_{2D}{}^{ex}(n=1) = 4E_{3D}{}^{ex}$). More accurate calculations have been reported by a number of authors [44, 45], where the well finiteness has been considered but will not be discussed here.

In Fig 2.8, the transition from the first confined heavy hole level to the n=1 exciton level is shown to be very strong. This important transition determines the absorption band edge in a compressively strained quantum well and is of primary interest to this thesis. The sharpness of the absorption edge is limited by the width of this exciton peak, which always remains finite. Factors such as phonon broadening, sample quality and layer uniformity, usually set the lower limit on this value [42].

2.2.5 The Quantum Confined Stark Effect

The strong electric field dependence of optical absorption near the band edge of a quantum well is a useful property which is exploited in such devices as electroabsorption modulators and optical attenuators [46]. This phenomenon, termed the "quantum confined Stark effect" (QCSE) in 2-D structures, is much stronger than that observed in bulk materials, via the Franz-Keldysh effect [47]. It is well understood and has been highly studied in the more commonly used material systems, such as GaAs/AlGaAs [48] and InGaAs(P)/InP [49].

The QCSE results from a distortion of the quantum well potential induced by a normally applied electric field. This effect, illustrated in Fig. 2.9, stimulates a decrease in the electron transition energies and tends to skew the electron and hole wavefunctions to opposite sides of the well, thereby increasing the exciton radius. Due to the enhanced exciton binding energy in 2-D structures, these resonances are clearly observable up to very high field values ($\sim$ 50 times the classical ionization field) [50], maintaining a relatively sharp band edge. Devices utilizing the QCSE usually have a p-i-n (p-doped, undoped, n-doped) layer structure which contains quantum wells centered in the intrinsic (undoped) region. This ensures that the majority of the applied voltage is uniformly dropped across the quantum wells. An important figure of merit for devices utilizing this effect is the change of optical absorption per unit of applied voltage. To maximize this quantity it is important for the width of the intrinsic region (d), to be thin enough for the applied voltage (V), to induce a large electric field (E=V/d). However, as will be discussed below, this region is important for optical waveguiding as well and must remain thick enough to provide effective confinement of the optical fields.

For the case of fields applied in a direction parallel to the quantum well layers, the primary effect is a broadening of the exciton resonances and consequently, the absorption band edge of the material. Higher field values lead to complete ionization of the carrier pairs, qualitatively mimicking the Stark effect observed in bulk crystals [50].

For perpendicular fields, the QCSE allows the absorption band edge to be tuned to

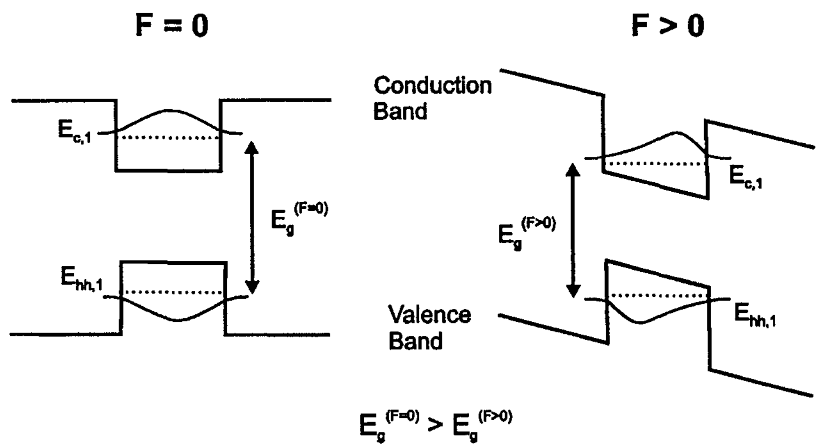

Figure 2.9: Quantum well potentials, energy levels and wavefunctions in the presence of zero applied electric field and nonzero applied electric field.

longer wavelengths with relatively little broadening. Fig. 2.10 illustrates experimental absorption data for various values of normally applied electric field. The data is seen to obey the above mentioned selection rules and polarization dependence. The energy level shifts are known to depend quadratically on the applied field and are enhanced for larger well widths [30]. For the ground state energy (n=1), the shifts are negative resulting in decreasing transition energies for increased electric fields.

The binding energy of the exciton is also dependent on the voltage applied to the device. As stated above, the exciton wavefunctions are skewed to opposite sides of the well by the electric field. This increases the bound electron-hole separation leading to a decrease in exciton binding energy which acts to reduce the overall energy level shift. However, this effect is usually small in InGaAs(P) quantum wells and tends to saturate at higher field values [49].

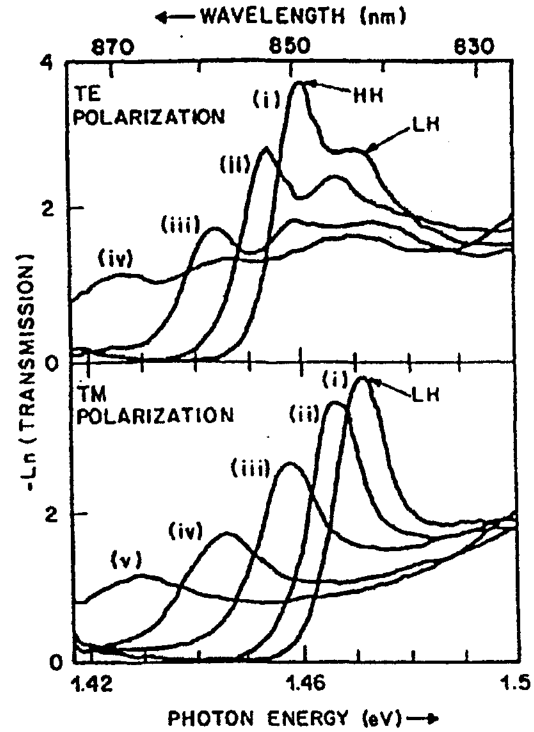

Figure 2.10: Optical absorption spectra of a GaAs/$Al_{0.3}Ga_{0.7}As$ quantum well waveguide for various values of normally applied electric field: a) TE polarization and b) TM polarization. The transitions involving heavy hole levels are observed in the case of TE data only. The curves (i)-(v) represent electric field values of 0 kV/cm, 60 kV/cm, 100 kV/cm, 150 kV/cm, and 200 kV/cm [51].

2.3 Optical Waveguide Theory

This section is concerned with the fundamentals of optical waveguide analysis. An optical waveguide is a medium that transports electromagnetic energy from one point in space to another. They are commonly used to confine optical fields near a device's active region or to interconnect elements in an optoelectronic circuit. The optical confinement is achieved by using a multilayered material structure containing a core region of higher refractive index relative to the surrounding cladding layers. As will be described below, electromagnetic radiation propagates through the waveguide as a set of discrete spatial energy distributions, known as optical modes. To calculate these allowed modes, two dimensional mode solvers are usually employed. They can be based on one of various modelling techniques, several of which are summarized in Refs. [52, 53]. This section describes one of the more common and simple approaches used, known as the effective index method.

To begin the discussion of optical waveguides, it is useful to examine Maxwell's equations which can be expressed as the following set of partial differential equations [54]:

$$\nabla \times \boldsymbol{E} = -\frac{d\boldsymbol{B}}{dt} \tag{2.35}$$

$$\nabla \times \boldsymbol{H} = \boldsymbol{J} + \frac{d\boldsymbol{D}}{dt} \tag{2.36}$$

$$\nabla \cdot \boldsymbol{D} = \rho \tag{2.37}$$

$$\nabla \cdot \boldsymbol{B} = 0 \tag{2.38}$$

where:

$\boldsymbol{E}$ is the electric field vector;
$\boldsymbol{B}$ is the magnetic displacement vector;
$\boldsymbol{D}$ is the electric displacement vector;
$\boldsymbol{H}$ is the magnetic field vector;
$\boldsymbol{J}$ is the current density;
ρ is the electric charge density.

These equations describe the behavior of electromagnetic waves in matter. For a linear isotropic medium, the displacement vectors can be expressed as:

$$\boldsymbol{D} = \epsilon \boldsymbol{E} \tag{2.39}$$

$$\boldsymbol{B} = \mu \boldsymbol{H} \tag{2.40}$$

where ϵ is the dielectric constant of the medium and μ is the magnetic permeability. For a nonmagnetic material, μ is often approximated as the permeability of free space $\mu \sim \mu_o = 4\pi\mathrm{x}10^{-7}$ H/m. If the material is considered to contain no sources of charge or current then ρ and $\mathbf{J}$ are usually neglected.

Eqs. 2.35-2.38 can be decoupled by taking the curl of Eqs. 2.35 and 2.36. By using the constitutive relations Eqs. 2.39 and 2.40, the following equations are obtained:

$$\nabla \times (\nabla \times \boldsymbol{E}) = \nabla(\nabla \cdot \boldsymbol{E}) - \nabla^2 \boldsymbol{E} = \nabla \times -(\frac{d\boldsymbol{B}}{dt})$$

$$-\frac{d}{dt}(\nabla \times \boldsymbol{B}) = -\mu\varepsilon \frac{d^2\boldsymbol{E}}{dt^2} \qquad (2.41)$$

$$\nabla \times (\nabla \times \boldsymbol{B}) = \nabla(\nabla \cdot \boldsymbol{B}) - \nabla^2 \boldsymbol{B} = \nabla \times (\mu\varepsilon \frac{d\boldsymbol{E}}{dt})$$

$$\mu\varepsilon \frac{d}{dt}(\nabla \times \boldsymbol{E}) = -\mu\varepsilon \frac{d^2\boldsymbol{B}}{dt^2} \qquad (2.42)$$

For a dielectric material $\nabla\cdot$ E $= 0$ and $\nabla\cdot$ B $= 0$, yielding:

$$\nabla^2 \boldsymbol{E} = \mu\epsilon \frac{d^2\boldsymbol{E}}{dt^2} \qquad (2.43)$$

$$\nabla^2 \boldsymbol{B} = \mu\epsilon \frac{d^2\boldsymbol{B}}{dt^2} \qquad (2.44)$$

Eqs. 2.43 and 2.44 are known as Maxwell's wave equations and are fundamental to waveguide analysis. By assuming harmonic fields, having a time dependence of $e^{i\omega t}$, Maxwell's equations are often reduced to the Helmholtz equations:

$$\nabla^2 \boldsymbol{E} + \omega^2 \mu\epsilon \mathrm{E} = 0 \qquad (2.45)$$

$$\nabla^2 \boldsymbol{H} + \omega^2 \mu\epsilon \mathrm{H} = 0 \qquad (2.46)$$

2.3.1 The Two Dimensional Slab Waveguide

The analysis of the dielectric slab waveguide is very important as it provides most of the basic principles necessary for the description of more complicated guiding structures.

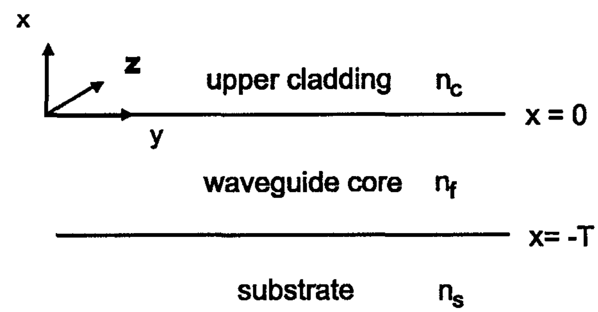

Figure 2.11: A three layer planar slab waveguide. The waveguide core region of refractive index n_f is positioned between cladding and substrate layers of refractive indices n_c and n_s, respectively. Optical confinement requires $n_f > n_c$, n_s. Light propagation is assumed to be in the z-direction.

In a 2D slab waveguide, light is guided in a central core layer of refractive index greater than the surrounding cladding layers (see Fig. 2.11). Due to the wave nature of the optical field, only certain allowed cross-sectional energy distributions can propagate down the guide. These are referred to as the eigenmodes or optical modes of the waveguide structure and can be calculated using Maxwell's equations. The electromagnetic wave must obey the following wave equation

$$\nabla^2 \boldsymbol{E} = (\frac{{n_i}^2}{c^2})\frac{d^2\boldsymbol{E}}{dt^2} \tag{2.47}$$

in all three layers, where n_i is the refractive phase index in layer i. An electromagnetic wave that propagates in the z-direction and is polarized in the y-direction has the form

$$\mathbf{E} = E_y(x)e^{i(\beta z-\omega t)}\mathbf{j} \tag{2.48}$$

in the slab guide. β represents the propagation constant of the guided mode while $\mathbf{j}$ is a unit vector pointing in the y direction. Eq. 2.48 represents TE polarized light consisting of field components E_y, H_x and H_z relative to the coordinate system in Fig. 2.11. The wave equation for the TE mode can be written as [55]:

$$\frac{d^2E_y(x)}{dx^2} + ({n_i}^2{k_o}^2 - \beta^2)E_y(x) = 0 \tag{2.49}$$

where $k_o = 2\pi/\lambda$ and λ is the vacuum wavelength of the optical field. The magnetic field components can be expressed:

$$H_x = -\frac{\beta}{\omega\mu} E_y$$
$$H_z = -\frac{1}{j\omega\mu}\frac{dE_y}{dx} \tag{2.50}$$

For a guiding layer of thickness T, we obtain the field solutions:

$$E_y(x) = \begin{cases} E_c e^{-\delta_c x} & x > 0 \\ E_f \cos(\kappa_f x + \phi) & 0 \geq x \geq -T \\ E_s e^{\delta_s (x+T)} & x < -T \end{cases} \tag{2.51}$$

with the propagation constants defined as:

$$\kappa_f{}^2 = n_f{}^2 k_o{}^2 - \beta^2$$
$$\delta_c{}^2 = \beta^2 - n_c{}^2 k_o{}^2 \tag{2.52}$$
$$\delta_s{}^2 = \beta^2 - n_s{}^2 k_o{}^2$$

By using the boundary conditions of the continuity of the tangential components of the electric and magnetic fields across the layer boundaries, the magnitudes of the above fields can be related:

$$E_c = E_f \cos\phi$$
$$E_s = E_f \cos(\kappa_f T - \phi) \tag{2.53}$$
$$\phi = tan^{-1}(\tfrac{\delta_c}{\kappa_f})$$

The value of E_f is arbitrary and is usually taken as unity for normalization purposes.

An important observation can be made at this stage. The only unknown in Eq. 2.53 is the propagation constant β. Once found, the field solutions can be easily calculated. β is commonly expressed in terms of an effective index N where $\beta = \mathrm{N}{\cdot}k_o$.

The boundary conditions yield the eigenvalue equation for TE modes which can be used to find the effective index N:

$$\kappa_f T = (m+1)\pi - \tan^{-1}(\frac{\kappa_f}{\delta_c}) - \tan^{-1}(\frac{\kappa_f}{\delta_s}) \tag{2.54}$$

where m denotes the mode number, and can take the values m = 0, 1, 2,... There is no simple solution to the above equation and graphical or numerical techniques are required [55]. Eq. 2.54 is usually written in terms of a normalized frequency V, a normalized guide index b, and an asymmetry parameter a, where

$$V = k_o T \sqrt{{n_f}^2 - {n_s}^2} \tag{2.55}$$

$$b = \frac{N^2 - {n_s}^2}{{n_f}^2 - {n_s}^2} \tag{2.56}$$

$$a = \frac{{n_s}^2 - {n_c}^2}{{n_f}^2 - {n_s}^2} \tag{2.57}$$

Using these definitions, the eigenvalue equation is written as

$$V\sqrt{1-b} = (m+1)\pi - \tan^{-1}\sqrt{\frac{1-b}{b}} - \tan^{-1}\sqrt{\frac{1-b}{b+a}} \tag{2.58}$$

By examining Eq. 2.58, it is found that to obtain a single mode waveguide, the normalized frequency must satisfy the following relation:

$$\tan^{-1}\sqrt{a} < V \leq \pi + \tan^{-1}\sqrt{a} \tag{2.59}$$

Following a similar procedure as above, the eigenvalue equation for TM polarized light having field components H_y, E_x and E_z can be obtained [56, 55]:

$$V[\sqrt{q_s}\frac{n_f}{n_s}]\sqrt{1-b_M} = (m+1)\pi - \tan^{-1}\sqrt{\frac{1-b_M}{b_M}} - \tan^{-1}\sqrt{\frac{1-b_M}{b_M + a_M(1-b_M d)}} \tag{2.60}$$

where

$$b_M = \frac{N^2 - {n_s}^2}{{n_f}^2 - {n_s}^2}(\frac{n_f}{n_s q_s})^2 \tag{2.61}$$

$$a_M = \frac{{n_s}^2 - {n_c}^2}{{n_f}^2 - {n_s}^2}(\frac{n_f}{n_c})^4 \tag{2.62}$$

$$q_s = (\frac{N}{n_f})^2 + (\frac{N}{n_s})^2 - 1 \tag{2.63}$$

$$d \equiv [1 - (\frac{n_s}{n_f})^2][1 - (\frac{n_c}{n_f})^2] \tag{2.64}$$

An important parameter known as the optical confinement factor Γ, for a given mode, can be defined as the fraction of optical power guided within the waveguide core relative to the total power contained in that mode. It is a measure of the breadth of the optical field distribution and it is usually beneficial to maximize this parameter for single mode waveguides used in active devices. Γ can be expressed as [30]:

$$\Gamma = \frac{\frac{1}{2}\int_{-T}^{0} Re(\mathbf{E} \times \mathbf{H}^*) \cdot \mathbf{z} dx}{\frac{1}{2}\int_{-\infty}^{\infty} Re(\mathbf{E} \times \mathbf{H}^*) \cdot \mathbf{z} dx} \tag{2.65}$$

2.3.2 Multi-layer Slab Waveguides

Waveguides containing more than three layers are frequently used for many semiconductor devices. Analytical solutions become very complex for these structures and alternative approaches should be followed. Walpita [57] has developed a numerical technique, commonly referred to as the zero matrix element method, which can be implemented for slab waveguides containing an arbitrary number of layers. This approach can be easily applied to the calculation of both the TE and TM modes and account for gain or loss, but for brevity only lossless TE solutions will be discussed here.

Fig. 2.12 displays an arbitrary N layer slab waveguide. Each of the layers are assumed to have a uniform thickness and refractive index profile. For TE polarized light, the electric field in the j'th layer must satisfy the wave equation (Eq. 2.49) and have the general form:

$$E_{y,j}(x) = A_j e^{-P_{x,j}(x-x_{j-2})} + B_j e^{P_{x,j}(x-x_{j-2})} \tag{2.66}$$

where

$$P_{x,j} = \sqrt{\beta^2 - n_j{}^2 k_o{}^2} \tag{2.67}$$

A_j and B_j (j=1..N) are the amplitudes of the forward and backward propagation components of the electric field, n_j is the refractive index of the j'th layer and x_j represents the position of the interface between layers j+1 and j+2.

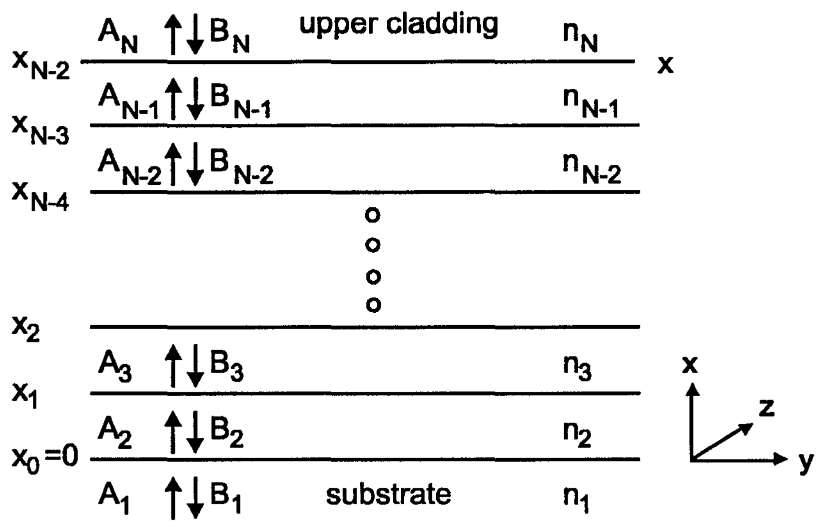

Figure 2.12: An arbitrary N layer slab waveguide structure. A_j and B_j represent the amplitudes of the forward and backward (with respect to the x-direction) propagation components of the electric field. n_j is the refractive index of the j'th waveguide layer. Light propagation is assumed to be in the z-direction.

A similar expression for the z-component of the magnetic field H_z, can be found using Eqs. 2.35 and 2.40:

$$-i\omega\mu_o H_{z,j}(x) = -P_{x,j}A_j e^{-P_{x,j}(x-x_{j-2})} + P_{x,j}B_j e^{P_{x,j}(x-x_{j-2})} \tag{2.68}$$

The tangential field components in layer j are matched at the upper and lower interfaces according to the above stated boundary conditions. At the upper interface (x=x_{j-1}) we have:

$$\begin{pmatrix} E_y \\ -i\omega\mu_o H_z \end{pmatrix} = \begin{pmatrix} e^{-P_{x,j}(x_{j-1}-x_{j-2})} & e^{P_{x,j}(x_{j-1}-x_{j-2})} \\ -P_{x,j}e^{-P_{x,j}(x_{j-1}-x_{j-2})} & P_{x,j}e^{P_{x,j}(x_{j-1}-x_{j-2})} \end{pmatrix} \begin{pmatrix} A_j \\ B_j \end{pmatrix} \tag{2.69}$$

Whereas, at the lower boundary (x=x_{j-2}):

$$\begin{pmatrix} E_y \\ -i\omega\mu_o H_z \end{pmatrix} = \begin{pmatrix} 1 & 1 \\ -P_{x,j+1} & P_{x,j+1} \end{pmatrix} \begin{pmatrix} A_{j+1} \\ B_{j+1} \end{pmatrix} \tag{2.70}$$

Equating Eqs. 2.69 and 2.70 yields:

$$\begin{pmatrix} A_{j+1} \\ B_{j+1} \end{pmatrix} = \mathbf{M}_j \begin{pmatrix} A_j \\ B_j \end{pmatrix} \tag{2.71}$$

where the transfer matrix $\mathbf{M}_j$ is defined as:

$$\mathbf{M}_j = \begin{pmatrix} 1 & 1 \\ -P_{x,j+1} & P_{x,j+1} \end{pmatrix}^{-1} \begin{pmatrix} e^{-P_{x,j}(x_{j-1}-x_{j-2})} & e^{P_{x,j}(x_{j-1}-x_{j-2})} \\ -P_{x,j}e^{-P_{x,j}(x_{j-1}-x_{j-2})} & P_{x,j}e^{P_{x,j}(x_{j-1}-x_{j-2})} \end{pmatrix} \quad (2.72)$$

Using an iteration process, the amplitudes of the field components in layer N can be related to those in layer 1. The resulting expression is given as:

$$\begin{pmatrix} A_N \\ B_N \end{pmatrix} = \begin{pmatrix} \alpha_1 & \alpha_2 \\ \alpha_3 & \alpha_4 \end{pmatrix} \begin{pmatrix} A_1 \\ B_1 \end{pmatrix} \quad (2.73)$$

where

$$\begin{pmatrix} \alpha_1 & \alpha_2 \\ \alpha_3 & \alpha_4 \end{pmatrix} = \mathbf{M}_{N-1}\mathbf{M}_{N-2}\cdots\mathbf{M}_1 \quad (2.74)$$

For guided modes, there should be no forward propagation component in the substrate layer (j=1) and no backward propagation component in the top cladding layer (j=N). This condition is equivalent to stating that the electromagnetic field must exponentially decay in these outer layers as a consequence of optical confinement. This demands that A_1 and B_N be zero:

$$\begin{pmatrix} A_N \\ 0 \end{pmatrix} = \begin{pmatrix} \alpha_1 & \alpha_2 \\ \alpha_3 & \alpha_4 \end{pmatrix} \begin{pmatrix} 0 \\ B_1 \end{pmatrix} \quad (2.75)$$

To satisfy Eq. 2.75 the following must hold:

$$\alpha_4 = 0 \quad (2.76)$$

Eq. 2.76 is an eigenvalue equation that can be used to calculate the propagation constants β for the given modes of the waveguide structure.

2.3.3 The Effective Index Method

Semiconductor waveguide devices usually require optical confinement in both the vertical and lateral directions. However, solving for the field distributions in two dimensions is not trivial. The guided modes in 3-D waveguides cannot be simply classified as TE or TM as in the 2-D case, but are hybrid in nature, containing

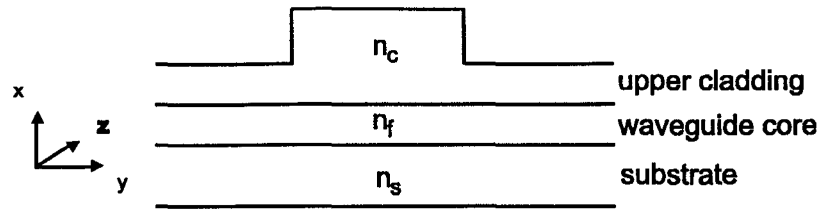

Figure 2.13: A strip loaded waveguide. Light confinement occurs beneath the etched rib in the core region of refractive index n_f. n_c and n_s are the refractive index values of the cladding and substrate layers, respectively. Light propagation is in the z-direction.

aspects of each. Generally, they are classified into one of two categories: $E_{pq}{}^x$ modes, having main electromagnetic field components E_x and H_y (resembling TM modes in the slab waveguide), and $E_{pq}{}^y$ modes, having dominant E_y and H_x components (resembling TE modes in the slab waveguide). The subscripts p and q represent the mode order or number of lobes in the field distributions in the x and y directions, respectively, where (p,q = 1,2,3...).

Exact solutions for 3-D optical waveguides are very difficult to obtain and it is necessary to resort to approximation techniques. One of the more common approaches is known as the effective index method, which offers the advantage of simplicity and has been shown to be very accurate for waveguides far above cut-off [58, 59].

The guiding structure of interest to this thesis is known as the "strip loaded" or "ridge" waveguide and is illustrated in Fig. 2.13. This type of guide is designed to allow the optical mode to evanescently penetrate into the etched ridge material. This has the effect of raising the effective index beneath the ridge, which produces lateral confinement of the optical field. The increase in effective index is dependent on the refractive index values and dimensions of the waveguide layers and is typically on the order of 10^{-4} to 10^{-5} [55]. Due to the relatively low horizontal index contrast, this type of structure is not well suited for applications requiring tight optical bending or branching. For these functions, step-index waveguides can be used which usually contain a core region surrounded in all directions by a lower refractive index cladding.

The effective index method is a technique well suited to analyze ridge waveguides.

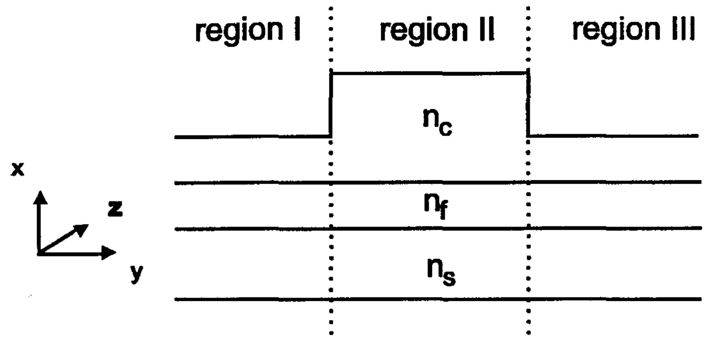

Figure 2.14: The 3-D waveguide is split into three regions. Each region can be treated as a 2-D slab waveguide.

It consists of breaking the 3-D structure into two 2-D slab waveguide problems, as seen in Fig. 2.14. First, the 3-D waveguide is broken into three distinct regions, each of which are treated as infinite 2-D slab guides. For $E_{pq}{}^{y}$ modes (having E_y as the dominant component), the procedures described above for solving 2-D slab guides can be utilized for TE modes in each of the three regions. This analysis will yield the effective indices N_I, N_{II} and N_{III} for regions I, II and III, respectively. In most ridge waveguide designs, symmetry will dictate that $N_I = N_{III}$. Defining $N_I = N_{III}$ $= N_{side}$, the condition for lateral confinement becomes $N_{II} > N_{side}$. The condition for vertical confinement is $n_f > n_c$, n_s.

The next step in the procedure is to turn the slab waveguide shown in Fig. 2.15, onto its side. The calculated effective indices are then used as the layer indices in a three layer slab waveguide problem. The eigenvalue equation 2.60 for TM modes should now be used to account for the change in waveguide orientation. The total effective index is then found and the field distributions can be obtained.

To obtain the solutions for $E_{pq}{}^{x}$ modes, a similar analysis can be followed. In this case, the effective indices for TM modes are calculated for the three slab guide regions. The waveguide is then turned onto its side and the TE eigenvalue equation 2.58 should be utilized.

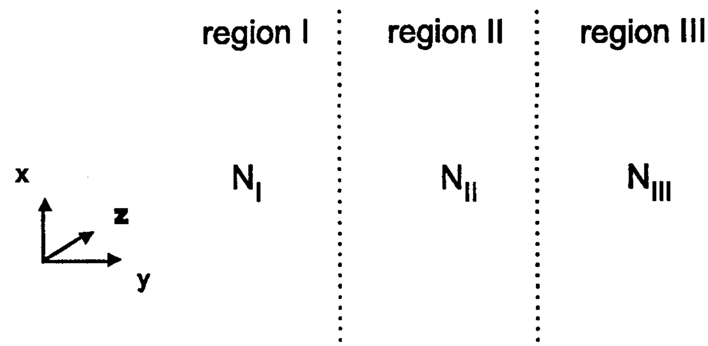

Figure 2.15: The effective indices obtained from regions I, II and III are used to construct a three layer slab guide. Since the waveguide structure is horizontally symmetric $N_I = N_{III}$.

2.3.4 Summary

In summary, an optical waveguide capable of channelling light to a desired location, is formed by growing a high refractive index layer between two lower refractive index layers. The optical radiation is found to propagate down the waveguide in discrete energy distributions, known as optical modes. By solving Maxwell's equations subject to the appropriate boundary conditions, the optical field distributions of the allowed modes can be obtained. The effective index method is an approximation technique which allows the 3-D optical waveguide to be analyzed as two separate 2-D planar waveguide problems.

Very thin heterostructures or quantum wells, provide many unique characteristics that are not offered by bulk materials. Some of the more important qualities are summarized below:

1) The geometry of the quantum well provides extra degrees of freedom (well depth and width) which allows a broad range of band gap tunability.

2)The step-wise density of states and strong 2-D exciton binding energy produce a very sharp absorption band edge in comparison to that of bulk materials.

3) By applying electric fields perpendicular to the growth direction, the absorption band edge can be tuned to longer wavelengths, while remaining sharp over a large

range of field values. This phenomenon, known as the quantum confined Stark effect, is very useful to devices such as electroabsorption modulators and tunable filters.

4) Finally, the thin quantum well layers allow strain to be introduced pseudomorphically and without the production of misfit dislocations. The lattice mismatch can be assumed to be accommodated as a homogeneous distortion of the quantum well material, which has the effect of altering its energy band structure. Strain provides another degree of freedom to tailor a material's energy gap, as well as providing a means to increase (or decrease) the absorption band edge separation for TE and TM polarizations.

These principles are very important for modern optoelectronic device technology. They have given devices utilizing quantum wells a strong advantage over those using bulk layer designs. The devices presented in this thesis exploit the benefits of all of these above mentioned effects and will be discussed further in chapter 4.

Chapter 3

Photodetectors

This chapter includes a brief introduction to p-i-n photodetector theory. The fundamental operating principles and the more commonly used figures of merit are discussed. In addition, some common detector designs are introduced, including the separated confined heterostructure.

Section 3.1 provides a general description of reverse biased p-i-n photodiodes, while section 3.2 considers the more specific case of p-i-n detectors fabricated as optical waveguides. The advantages of and motivations for using waveguide based photodetectors in this thesis work, are described. In addition, the concept of using multi-segment waveguide photodetectors for wavelength monitoring applications is introduced.

3.1 P-I-N Photodetectors

Photodetectors based on p-n junctions have become the dominant receiver technology for optical communication systems due to their high sensitivity and frequency response [1]. Some of the basic physics behind these devices will be discussed in this section.

P-n junction photodiodes are usually operated under a reverse bias where their current-voltage (I-V) characteristics are essentially independent of voltage. When p- and n-type materials are brought together to form a junction, the space charge

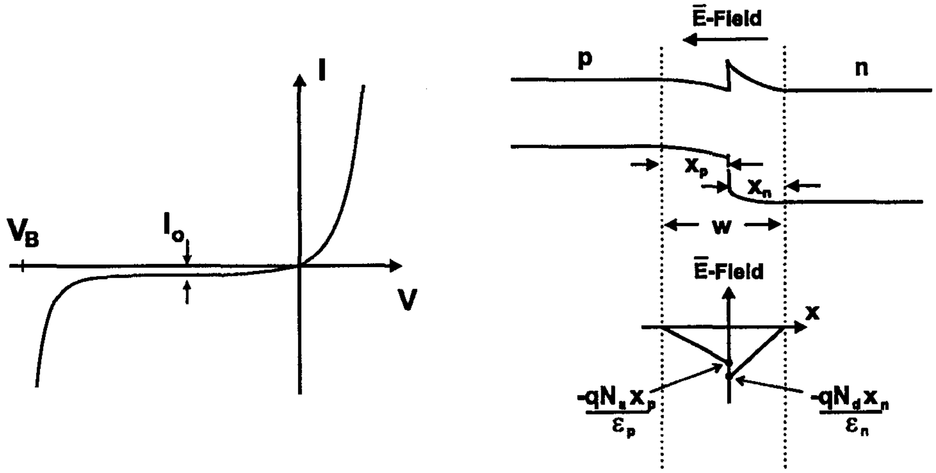

Figure 3.1: The electrical properties of a p-n heterojunction. The I-V characteristics, energy band diagram and electric field distribution are shown.

region that is created near the interface can be regarded as essentially being void of free carriers. An electric field is induced across the junction directed from the n- to the p-side. When the diode is operated under reverse bias, the effect is to increase the field (and depletion region width). This prevents majority carriers from diffusing across the junction and creates a nearly constant current with increasing bias. The energy band diagram, electric field distribution and I-V characteristics of a p-n heterojunction photodiode are illustrated in figure 3.1.

For an abrupt junction, the depletion layer width is given as:

$$w = x_n + x_p \tag{3.1}$$

where x_p and x_n represent the penetration distance into the p- and n-materials, respectively. They can be expressed as [60]:

$$x_p = [\frac{2\varepsilon_n\varepsilon_p\varepsilon_o N_d(V_{bi} - V)}{qN_a(\varepsilon_n N_d + \varepsilon_p N_a)}]^{1/2} \tag{3.2}$$

$$x_n = [\frac{2\varepsilon_n\varepsilon_p\varepsilon_o N_a(V_{bi} - V)}{qN_d(\varepsilon_n N_d + \varepsilon_p N_a)}]^{1/2} \tag{3.3}$$

where N_a and N_d are the doping concentrations of the p- and n-sides, respectively. V is the applied bias, V_{bi} is the built-in potential of the junction, and ε_n and ε_p represent the relative dielectric constants of the doped layers.

The current-voltage behavior of a p-n junction is described by the diode equation [61]:

$$I = I_o(e^{\frac{qV}{kT}} - 1) \tag{3.4}$$

I_o is referred to as the reverse saturation current which always remains finite. It is usually dominated by minority carrier extraction from the edge of the space charge region in both the n- and p-sides. For InGaAsP photodiodes, generation/recombination currents resulting from the creation and extinction of electron-hole pairs in the depletion region, are also found to be significant at low reverse bias [62]. At larger applied voltages, currents resulting from carrier tunnelling across the junction can become dominant.

An important characteristic of a p-n junction detector is the value of reverse saturation current under zero light conditions, termed the "dark current," I_d. It is important to minimize this parameter for several reasons. Firstly, the dark current shot noise is proportional to $\sqrt{I_d}$, and is usually a significant factor in determining the detector sensitivity [1]. Secondly, it is often critical to avoid excess heating of the device, and to maximize the electric field induced across the junction for a given applied bias. Several methods can be used to lower I_d including the use of small area detectors, heterojunction designs and device cooling. The breakdown voltage of the diode V_{br}, limits the operating regime of the detector. The usual breakdown mechanism for a typical photodiode structure is avalanche multiplication of carriers within the depletion region resulting from impact ionization of the lattice atoms [1]. The breakdown field can generally be increased by decreasing the intrinsic region width.

The more conventional type of photodiode involves surface illumination, in which the incident light must travel through one of the doped layers before reaching the depletion region. Light absorbed within a diffusion length of, or directly in the depletion region will increase the reverse bias current as illustrated in Fig. 3.2. The induced photocurrent is well approximated to behave linearly with optical input power for levels below detector saturation. It is important for the depletion region to be wide enough to create a large absorbing volume. If it is too thin, a significant portion of the

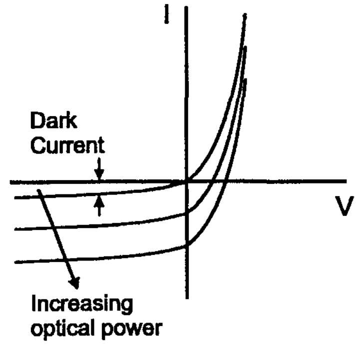

Figure 3.2: The I-V characteristics of a reversed biased p-n junction detector under various illumination levels.

incident light will propagate through the device without being detected. This will lead to a decrease in the quantum efficiency and sensitivity of the photodiode. To create a wide depletion region, one side of the junction can be lightly doped and/or a large reverse bias can be applied (see Eqs. 3.1-3.3). A more convenient and controllable way is to grow an intrinsic region between the p- and n-doped layers creating a p-i-n photodiode. The depletion region now extends over a distance of $w = x_i + x_p + x_n$, where x_i is the intrinsic layer width. The structure and electric field distribution of a p-i-n detector are shown in Fig. 3.3. The electric field strength E, is found to vary approximately linearly across the intrinsic region, with a total variation of [63]:

$$\Delta E = \frac{qN_i x_i}{\varepsilon_r \varepsilon_o} \tag{3.5}$$

where N_i is the impurity concentration of the undoped material. For structures containing lightly doped, thin i-regions, the electric field is often taken to be constant.

An important figure of merit for a photodetector is known as the "external quantum efficiency," which is a measure of the conversion efficiency from the optical to electrical domain. It can be defined as the ratio between the number of carriers producing photocurrent to the number of incident photons and can be expressed as:

$$\eta_e = (1 - R)\eta_{in}[exp(-\alpha x_1) - exp(-\alpha x_2)] \tag{3.6}$$

where x_1, x_2 represent the beginning and end of the depletion region, R is the surface reflectance, η_{in} is the internal quantum efficiency and α is the absorption coefficient

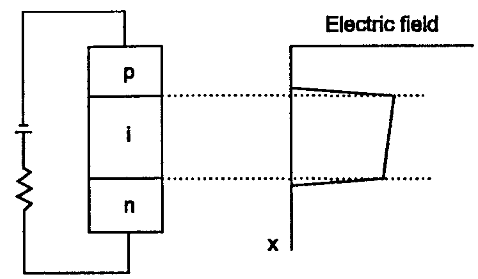

Figure 3.3: The p-i-n diode structure and associated electric field distribution in the depletion region.

of the material. Detector designers are usually concerned with the external quantum efficiency, which determines the detector output, as opposed to the internal quantum efficiency. Therefore, this term is commonly referred to as simply the quantum efficiency of the detector and this terminology will be adopted throughout this thesis.

Anti-reflection coatings are commonly applied to the detector surface to reduce R thereby, increasing η_e. The wavelength dependence of η_e is taken into account via the absorption coefficient and detector materials are usually selected to have a band gap energy slightly less than the incoming photon energy. Photons with energies much larger than the material band gap do not contribute towards photocurrent as they are strongly absorbed near the surface and the generated carriers can recombine before reaching the junction. Conversely, photons with energies less than the detector band gap cannot stimulate interband absorption.

A related quantity used to characterize detectors operating at wavelengths less than a few microns is the "responsivity". This quantity is defined as the output current produced per unit of optical input power:

$$\Re = \frac{I_{ph}}{P_o} \tag{3.7}$$

In terms of the quantum efficiency, the responsivity is given as:

$$\Re(\lambda) = (\frac{e\lambda}{hc})\eta_e(\lambda) \tag{3.8}$$

where the first term accounts for the conversion from optical power to photocurrent, and λ is the photon wavelength. $\Re$ not only depends on the absorbing material quality and photon wavelength, but strongly on the detector design as well. It is usually expressed in Amps/Watt.

3.2 Waveguide Photodetectors

High speed, surface illuminated p-i-n detectors capable of operating at frequencies well into the GHz range, are now commercially available. However, the high frequency response has been obtained at the cost of a reduced quantum efficiency. The frequency response of these detectors can ultimately be limited by the transit time of the photogenerated carriers across the depletion region. Therefore, it is important that this region be thin to minimize this delay. As discussed above, to obtain a high quantum efficiency a wide intrinsic region is required. This leads to a trade-off in design and becomes even more important to detectors using indirect band gap semiconductors, such as silicon and germanium, which have a much smaller absorption coefficient. One way to overcome this problem is to use a waveguide photodetector, in which the optical signal propagates in a direction parallel to the absorbing layer. For this design, the intrinsic region can be made thin in the direction of carrier collection for speed considerations, while the interaction distance of the optical field and absorbing material is independently determined by the waveguide length.

There are many other advantages of waveguide photodetectors over surface illuminated devices. For high speed operation of conventional p-i-n detectors, a large reverse bias is required. The bias is chosen to sweep the electrons (holes) out of the depletion region at their scattering limited velocities, thereby minimizing the carrier transit time. Due to the thin intrinsic region in waveguide photodetectors, high speed operation can be obtained even at zero bias. This is advantageous not only for power conservation and simplified receiver design, but also for minimization of the detector dark current, resulting in negligible shot noise [64]. If a reverse bias is applied to the waveguide photodiode, the thin intrinsic region allows a relatively small voltage to induce a large electric field. This enhances the electroabsorption effect or QCSE described in the last chapter. Finally, a double heterostructure waveguide photodetector has a similar material structure to that of a conventional laser diode, allowing

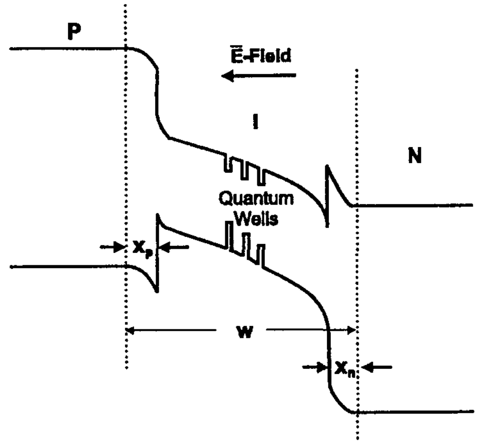

Figure 3.4: The energy band diagram for a separate confined heterostructure containing three quantum wells under reverse bias.

the potential for monolithic integration, or fabrication of the devices on the same wafer.

Due to the numerous benefits offered by waveguide based photodetectors, significant interest has been generated in their development. Currently, the majority of work has focussed on the application of the devices to high speed detection in optical communication systems. In this thesis work, however, the primary motivation for using waveguide based photodetectors, is the desire to use quantum wells as absorbing regions. Quantum well thicknesses are usually on the order of nanometers and very little absorption will occur for light propagation normal to the layer structure, unless a large number of quantum wells are used (10's to 100's). Conversely, the increased interaction length offered by the waveguide photodetector allows a high quantum efficiency to be obtained for detectors containing as few as one quantum well.

A separate confined heterostructure (SCH) is used in this work. It contains three undoped InGaAsP quantum wells, centered in an intrinsic region that has a smaller band gap energy than the surrounding p- and n-regions. The energy band diagram of the structure is illustrated in Fig. 3.4. This design is chosen as it offers the benefits of both carrier and optical confinement. Quantum wells are used for reasons summarized in chapter 2. Their sharp absorption band edge, large band gap tunability with voltage bias, and strain induced splitting of the valence bands are beneficial for the device design proposed in this thesis. These aspects will be discussed in detail, in chapter 4.

The external quantum efficiency of a quantum well waveguide photodetector can be expressed as [64]:

$$\eta_e = \frac{\Gamma\alpha^{int}}{\alpha}\eta_{in}(1 - e^{-\alpha L}) \tag{3.9}$$

where Γ is the optical confinement factor for the active layer, α^{int} represents the interband absorption coefficient of the quantum well at the excitation wavelength, L is the waveguide length and α is the total attenuation coefficient of the propagating optical mode. α can be written as:

$$\alpha = \Gamma\alpha^{int} + \Gamma\alpha_{fc,q} + (1 - \Gamma)\alpha_{fc,c} + \alpha_o \tag{3.10}$$

where α_o is the scattering loss coefficient of the waveguide, $\alpha_{fc,q}$ and $\alpha_{fc,c}$ represent the free carrier absorption in the quantum well and barrier layers, respectively. The free carrier absorption becomes significant for photon energies well below the absorption band edge in a highly doped material and is usually several orders of magnitude less than the interband absorption in p-i-n detectors [28]. Therefore, this contribution is often ignored and α reduces to $\alpha = \Gamma\alpha^{int} + \alpha_o$. The interband absorption coefficient α^{int}, is dependent on the applied detector bias via the QCSE, whereas the scattering loss coefficient α_o, is not.

One drawback of using a waveguide photodetector is the difficulty of efficiently coupling the input light into the optical waveguide. For this reason, an optical lens or tapered fiber is usually used to assist in the coupling. For InGaAsP devices, typical tapered fiber-to-waveguide coupling efficiencies of $\gamma \sim 0.3-0.6$ are routinely achieved. In a practical situation, this effect should be taken into account as well as the losses due to the reflection R, at the waveguide facet. Eq. 3.9 can be modified to include these effects [64]:

$$\eta_e = \gamma(1 - R)\frac{\Gamma\alpha^{int}}{\alpha}\eta_{in}(1 - e^{-\alpha L}) \tag{3.11}$$

The photocurrent generated in the waveguide photodetector is given by the product of the optical input power P_o and the detector responsivity defined in Eq. 3.8.

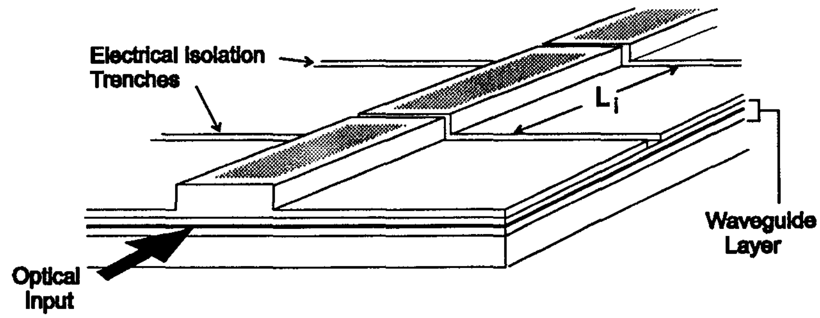

Figure 3.5: A multi-segment ridge waveguide structure orientated in an in-line geometry.

Using Eqs. 3.8 and 3.11 the photocurrent is given as:

$$I_{ph} = \frac{e\lambda}{hc} P_o \gamma (1 - R) \eta_{in} \frac{\Gamma \alpha^{int}}{\alpha} (1 - e^{-\alpha L}) \tag{3.12}$$

3.3 Multi-Segment Waveguide Photodetectors

Waveguide structures containing multiple in-line segments are useful for devices that require electrical isolation between two or more active elements. Fig. 3.5 illustrates such a design. Segmented waveguides have been used for a variety of applications including tunable diode lasers [41], polarization sensors [65] and wavelength division demultiplexing detectors [66]. To predict the photocurrent in a given section of a multi-element waveguide detector, a screening factor accounting for the absorption in the preceding elements, must be included. The optical power reaching the i'th segment of a multi-segment waveguide is given as:

$$P_i = P_o e^{(-\sum_{k=1}^{i-1} \alpha_k L_k)} \tag{3.13}$$

where α_k and L_k are the absorption coefficient and length of the k'th segment, respectively. Using Eqs. 3.12-3.13, the photocurrent produced in the i'th segment can be expressed as [67]:

$$I_{ph} = \frac{e\lambda}{hc} P_o \gamma (1 - R) \eta_{in} \frac{\Gamma {\alpha_i}^{int}(\lambda)}{\alpha_i(\lambda)} e^{-\sum_{k=1}^{i-1} \alpha_k(\lambda) L_k} (1 - e^{-\alpha_i(\lambda) L_i}) \tag{3.14}$$

It is seen that the generated photocurrent is dependent on many factors, some of which are difficult to calculate or measure precisely. If the ratio of photocurrents between two consecutive in-line waveguide sections of equal segment length and applied voltage bias is taken, many of these parameters will factor out. From Eq. 3.14, the ratio of the photocurrents in two adjacent elements can be written as:

$$\frac{I_2}{I_1} = e^{-\alpha_i(\lambda)L} \tag{3.15}$$

ignoring any scattering between detector ridge sections. Eq. 3.15 indicates that the measurement of I_2/I_1 can be used as a simple technique to obtain the total absorption coefficient. The strong wavelength dependence of α near the detector band edge allows the ratio of photocurrents to act as a sensitive measure of wavelength over this range, which remains independent of the optical input power and coupling efficiency. In this thesis, we demonstrate a high precision wavelength monitor based on this principle.

Chapter 4

Design and Fabrication

The past two chapters have described the theory and modelling techniques used in this thesis to design the proposed optoelectronic device. This chapter presents the final wafer and detector design and the important modelling results.

Section 4.1 describes the chosen structure, active region and energy level calculations, while the waveguide parameters including the ridge width, etch depth and optical mode profiles, are presented in section 4.1.1. Finally, the fabrication procedures including the photolithographic processing, deposition of the metal electrodes and the mounting of the finished devices are described in section 4.2.2.

4.1 Device Structure

The material used to fabricate the in-line waveguide photodetectors was grown in the molecular beam epitaxy (MBE) facility located at McMaster University. The layer composition of the wafer is shown in Fig. 4.1. The material structure consists of twelve epitaxially grown layers on an n^+-InP substrate. The highly doped substrate provides a low series resistance electrical path, as well as allowing high quality ohmic contacts to be formed with the selected metal. Two InP buffer layers are then grown, with the second having a lower doping level to reduce free carrier absorption loss. The waveguide core contains three 50 $\AA$ undoped quantum wells compressively strained by approximately -0.93 %, centered between two 2500 $\AA$ intrinsic

$In_{0.758}Ga_{0.242}As_{0.525}P_{0.475}$ quaternary layers. The quantum wells are separated by 100 $\AA$ wide barrier regions which are thick enough to effectively isolate the wells. 5000 $\AA$ p-doped InP buffer layers are grown to create a symmetrical waveguide structure. Finally, a highly doped p^+ InGaAs cap layer is added for improved electrical contact with the p-side metal.

The wavelength monitor design is illustrated in Fig 4.2. Two waveguide segments of equal length are patterned along a shared ridge waveguide channel. The ridges are etched through the InGaAs cap layer and partially into the p-InP buffer layers to a total depth of 0.95 μm. To ensure electrical isolation between waveguide sections, 5-10 μm wide trenches are etched through the doped layers to the intrinsic waveguide core material. Metal is deposited on the top of the ridge segments and the bottom of the substrate to form the electrical contacts.

The quantum well and barrier compositions were chosen such that the absorption band edge would extend across a wavelength of 1550 nm. The energy level calculations were performed based on the procedures introduced in chapter 2. Binary interpolation described in section 2.2.1, was used to estimate the values of bulk lattice constants, conduction band effective masses, Luttinger parameters, elastic constants and deformation potentials. Eqs. 2.2 and 2.23 were used to find the valence band masses and the bulk energy gap of the well and barrier compounds, respectively. The correction factors to account for the hydrostatic and shear components of strain were found by solving Eq. 2.28, using the interpolated constants. These calculated parameters are summarized in Table 4.1.

As described in section 2.2.2, the conduction band offset is taken to be 35 % of the total energy gap difference between the well and barrier materials after being corrected for strain, while the offset in the valence band accounts for the remaining 65 %. The heavy and light hole exciton binding energies are estimated to be 5.3 meV and 6.5 meV respectively, using the method of Mathieu et al. [44]. The first order transition energies from the heavy and light hole levels to the conduction band are then calculated using the analysis in section 2.2.2, and Eqs. 2.26 - 2.27.

InGaAs	p - 6 x10^{18}	2000 A	Cap
InP	p - 1 x10^{18}	5000 A	Buffer
InP	p - 4 x10^{17}	5000 A	Buffer
$In_{0.758}Ga_{0.242}As_{0.525}P_{0.475}$	undoped	2500 A	Waveguide
$In_{0.758}Ga_{0.242}As_{0.81}P_{0.19}$	undoped	50 A	QW
$In_{0.758}Ga_{0.242}As_{0.525}P_{0.475}$	undoped	100 A	Barrier
$In_{0.758}Ga_{0.242}As_{0.81}P_{0.19}$	undoped	50 A	QW
$In_{0.758}Ga_{0.242}As_{0.525}P_{0.475}$	undoped	100 A	Barrier
$In_{0.758}Ga_{0.242}As_{0.81}P_{0.19}$	undoped	50 A	QW
$In_{0.758}Ga_{0.242}As_{0.525}P_{0.475}$	undoped	2500 A	Waveguide
InP	n - 4 x10^{17}	5000 A	Buffer
InP	n - 1x10^{18}	5000 A	Buffer
InP	n^+		Substrate

Figure 4.1: The wafer structure used to fabricate the in-line waveguide photodetectors.

Parameter	Symbol	Unit	Barrier	Quantum Well
Bulk Energy Gap	E_g	meV	1000.2	718.1
Bulk Lattice Constant	a	Å	5.8689	5.9238
Luttinger Parameters	γ_1		11.23	14.77
	γ_2		4.22	5.77
Elastic Constants	C_{11}	$10^{11} dyn/cm^2$	10.13	9.56
	C_{12}	$10^{11} dyn/cm^2$	5.28	4.95
Deformation Potentials	a	eV	-7.01	-6.95
	b	eV	-1.84	-1.80
Effective Mass	m_c	m_o	0.066	0.047
	m_{hh}	m_o	0.358	0.309
	m_{lh}	m_o	0.051	0.038
Strain	ε	%	0.002	-0.932
Hydrostatic Component	δE_{hy}	meV	0.2	-62.5
Shear Component	δE_{sh}	meV	0.2	-68.4

Table 4.1: Calculated material parameters using the analysis of section 2.2.

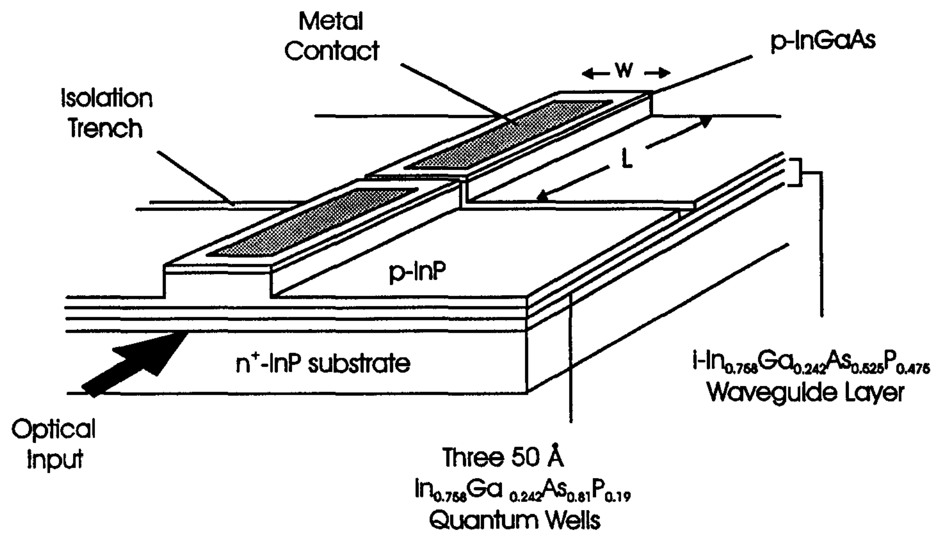

Figure 4.2: The wavelength monitor design.

They are found to be:

$$\begin{aligned} E_{e1} &\rightarrow E_{hh1} = 811.1meV \\ E_{e1} &\rightarrow E_{lh1} = 923.2meV \end{aligned} \tag{4.1}$$

The exciton absorption peak for TE polarization corresponds to a wavelength of 1529 nm, while the TM band edge is located at a significantly higher energy, corresponding to 1343 nm.

4.1.1 Waveguide Modelling Results

The optical waveguides were designed assuming a rectangular ridge shape and step index contrasts between material layers. The second assumption is well satisfied for epitaxially grown materials, while the first approximation is not always valid. As will be discussed in section 4.2.2, the ridge profiles vary significantly for different fabrication techniques. As a consequence, slight deviations from the model may result, depending on the fabrication procedure used. These issues are discussed further in chapter 5.

The accuracy of the waveguide calculations is limited by the knowledge of the refractive index values of the materials composing the layer structure. As discussed in chapter 2, there have been several models proposed to predict the refractive index for a given material at a given photon energy. The model of Pettit and Turner (Eq. 2.3) was used to calculate the index of refraction for the InP cladding and substrate layers. The layers composing the waveguide core region were treated using the method of Burkhard et al. [34]. It is not a straightforward problem to calculate the refractive index of the strained quantum well regions. The models described in chapter 2 are only valid for lattice matched compounds, as are most other established techniques. Therefore, an estimate was made by obtaining a correction factor to account for the lattice mismatch using a binary interpolation. This factor was taken as the difference between the interpolated indices for the strained quaternary and a lattice matched quaternary of the same bandgap energy, using Eq. 2.1. This value was then used as an offset by adding it to the result obtained from the model of Burkhard et al. for the lattice matched composition. As will be discussed below, the quantum well regions compose a very small fraction of the active region volume, and therefore do not significantly influence the waveguiding properties. Table 4.2 summarizes the calculated results.

Using the analysis presented in section 2.3, the mode solutions for the multi-layer waveguide structure were obtained. It was decided that a 3 μm wide ridge etched to a height of 0.95 μm would provide suitable results. The modal solutions for this design are shown in Figs. 4.3 and 4.4 for TE and TM polarizations, respectively. The right axes display the refractive index profile of the layer structure in the y (growth) direction and the effective indices along the x (transverse) direction.

To study the effects of waveguide geometry on device operation, three different ridge widths of 2, 3 and 5 μm were designed. The modelling results are listed in table 4.3. All of the waveguide widths remain single mode for TE polarization, whereas the 5 μm ridge can support two TM modes. The confinement factors vary significantly for the different dimensions and polarizations, ranging from 0.34 to 0.71, with the TM modes being more strongly confined to the waveguide core region. The confinement factor between the optical fields and the quantum wells ranges from approximately 1.2 - 2.6 %. Therefore, their influence is slight on the optical mode. The effective indices of the guides were found to only vary by approximately 0.06 % when the

Layer #	Function	Material	Refractive Index
1	Cap	$p^+ - In_{0.53}Ga_{0.47}As$	3.6131
2	Outer Cladding	p-InP	3.1651
3	Inner Cladding	p-InP	3.1656
4	Core	$i - In_{0.758}Ga_{0.242}As_{0.525}P_{0.475}$	3.4002
5	Quantum Well	$i - In_{0.758}Ga_{0.242}As_{0.81}P_{0.19}$	3.4650
6	Barrier	$i - In_{0.758}Ga_{0.242}As_{0.525}P_{0.475}$	3.4002
7	Quantum Well	$i - In_{0.758}Ga_{0.242}As_{0.81}P_{0.19}$	3.4650
8	Barrier	$i - In_{0.758}Ga_{0.242}As_{0.525}P_{0.475}$	3.4002
9	Quantum Well	$i - In_{0.758}Ga_{0.242}As_{0.81}P_{0.19}$	3.4650
10	Core	$i - In_{0.758}Ga_{0.242}As_{0.525}P_{0.475}$	3.4002
11	Inner Cladding	n-InP	3.1641
12	Outer Cladding	n-InP	3.1614
13	Substrate	n^+-InP	3.1438

Table 4.2: The calculated refractive indices of the material layers used in the waveguide mode calculations. Free carrier effects are included [56].

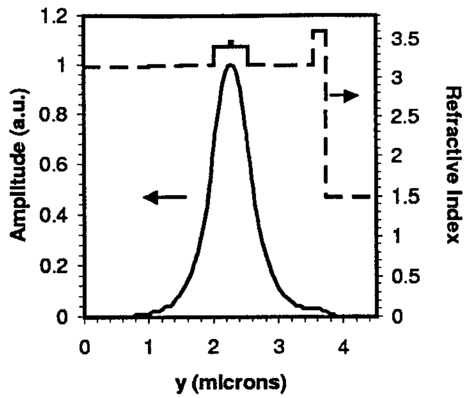

Figure 4.3: The calculated TE mode profiles (left) in the growth direction and (right) in the transverse direction. The refractive index profiles are also shown.

refractive index correction for the quantum wells was ignored in the simulations.

4.2 Device Fabrication

This section describes in detail the fabrication procedure followed to develop the in-line waveguide photodetectors. The photolithographic processing, chemical etching, metallization, wafer dicing and mounting are discussed.

4.2.1 Photomask Design

The fabrication process begins with the design of a suitable photomask, which contains the desired device features. It usually consists of a glass or quartz plate which is chrome coated on one side. The chrome is removed using a collimated electron beam to define the designed features, usually of micron dimension. It is then used to pattern a semiconductor wafer through photolithographic processing.

The original photomask in this work was designed based on the modelling results presented in Sec. 4.1.1. Variations in device dimensions were added to study their effects. Ridge widths of 2, 3 and 5 μm were patterned in combination with various waveguide segment lengths ranging from 100 to 500 μm. In addition, two trench widths of 5 and 10 μm were included to study the effects of scattering and electrical

Ridge Width	Polarization	Supported Mode #, m	n_{eff}	Γ_{WG}	Γ_{QW}
2 μm	TE	0	3.3044	0.3367	0.0120
	TM	0	3.2946	0.4704	0.0171
3 μm	TE	0	3.3052	0.5288	0.0190
	TM	0	3.2964	0.6106	0.0221
5 μm	TE	0	3.3061	0.6862	0.0247
	TM	0	3.2978	0.7052	0.0258
	TM	1	3.2919	0.4500	0.0163

Table 4.3: The calculated waveguide parameters for ridge widths of 2, 3 and 5 μm. Γ_{WG}, Γ_{QW} and n_{eff} are the optical confinement factor in the waveguide core region, confinement factor in the quantum well region, and the effective index of the mode, respectively.

isolation between detectors. Straight waveguides with no isolation trench etched along their length, were also added to examine the optical guiding qualities of the material structure. The photomask layers are shown in appendix B.

The in-line detector fabrication involves a four step process, requiring four separate masks. The mask sets in order of their use consist of ridge definition, isolation trench patterning, dielectric window etch, and metallization (lift-off) preparation. Several alignment features were added on the photolithographic plates for precise alignment of the subsequent mask layers.

4.2.2 Photolithographic Processing

The fabrication process is critical in determining wafer yield and device performance. The steps followed to fabricate the waveguide photodetectors are described in this section.

All of the processing steps were performed in the class 10 000 clean room facilities located at McMaster University (class 1000 wet bench), with the exception of the thinning and dicing of the devices. In the laboratory environment, the detectors are operated as "bare chip," meaning that they are not hermetically sealed or packaged.

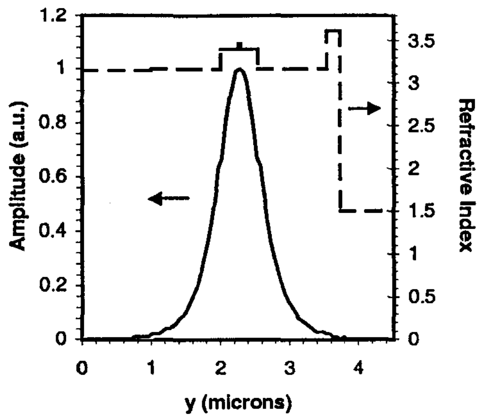

Figure 4.4: The calculated TM mode solutions for a 3 μm wide, 0.95 μm high ridge (left) in the growth direction and (right) in the transverse direction.

Therefore, dust contamination is not an issue for these former two procedures.

Wafer Cleaning

The first step in the fabrication process involves cleaning the wafer to remove surface contamination. This was found to be a very important step as particles left on the wafer surface can significantly decrease the wafer yield by causing nearby devices to be improperly processed. Also, larger unremoved contaminants prevent the photomask from making direct contact to the wafer surface, decreasing the photolithographic resolution.

After removing loose particles from the sample with compressed nitrogen, the wafer is immersed in an acetone bath heated to 80° C for approximately 5 minutes. It is then soaked in heated methanol for the same length of time and rinsed with deionized water. An ozone clean follows in which the sample is placed in a UV ozone chamber for 10 minutes to oxidize any residual organics or greases. A 45 second dip in a buffered hydrofluoric acid solution is then used to remove any oxides. It was observed that the samples were sufficiently clean to be processed after undergoing this procedure.

Photolithography

The cleaned wafer is spin coated with an organic silicate glass (Accuglass 111, made by Allied Signal Inc.) and baked for approximately 24 hours at 250°C. The baking allows the glass to form and harden, preparing it to withstand the acids used for the semiconductor etching. The spin-on glass was measured to be approximately 0.12 μm thick and to be very uniform for a spinning speed of 3000 r.p.m for 30 seconds. The glass was then patterned using standard photolithography. Positive photoresist (Shipley 1808) was spun onto the wafer surface using a speed of 4000 rpm and soft baked at 100° C for 2 minutes to remove solvents and prepare it for exposure.

The photomask pattern is transferred to the photoresist using a Karl Suss MJB-3 mask aligner. The first step for the photodetector fabrication is the patterning of the waveguide ridges. The mask is horizontally centered above the sample and aligned in one of two orientations. The first set of detectors were fabricated with the ridges running in a direction parallel to the major flat of the wafer ($(0\bar{1}1)$ crystal direction). In the next set of devices the ribs were etched 90° to this direction. Once aligned, the mask is placed in direct contact with the sample using a vacuum seal. The photoresist is then exposed through the openings in the photomask using a 365 nm mercury ultraviolet lamp, incorporated into the mask aligner. An exposure time of approximately 3.5 seconds at an intensity of 9.6 mW/cm^2 was found to provide the best results. After exposure, the photoresist was developed using a 5:1 deionized water/developer (Shipley 351 positive photoresist developer) solution to remove the exposed photoresist. If the above procedures do not produce a clean, sharp pattern, all of the photoresist is removed using acetone and the stages are repeated. The wafer was then baked at 150° C for 2 minutes to harden the photoresist and increase its resistance to the acids used below.

The next step in the procedure involves using the photoresist as a mask to pattern the spin-on glass. The spin-on glass is etched with a buffered 10:1 deionized water, hydrofluoric (HF) acid solution. The hardened photoresist is resistant to this acid and the areas directly beneath the patterned resist will not be etched, although some undercutting may occur. It is therefore important not to over etch the sample. The sample is manually agitated in the HF solution for approximately 25 seconds. Since HF attacks glass, Teflon coated beakers and tweezers were used. The wafer is then placed under the optical microscope to verify that the etching is complete. If so, the photoresist is then removed using a stripper compound (EMT 130 TX positive photoresist stripper) heated to 80°C. The patterned glass now acts as a mask for the semiconductor etch.

The InGaAs cap layer is first "wet" etched using a sulfuric acid solution consisting of 1:8:160, $H_2SO_4 : H_2O_2 : H_2O$. A 90 second agitated dip was performed to remove the 0.2 μm layer. The timing in this case was not critical, as the lower InP buffer layer acts as an "etch-stop" since the etching rate of InP using this solution is extremely small. A Tencor Alphastep 200 machine was used to profile the wafer surface allowing a determination of the rib height to be made. The InP buffered layers are then patterned using a 1:3, $HCl : H_3PO_4$ solution. The InP was etched to a depth of 0.75 μm, and the timing for this step was critical as there was no stop-etch layer incorporated into this wafer. To make sure the proper depth was achieved, the wafer was soaked in the acid solution for short time periods ranging from 10 to 30 seconds and alpha stepped frequently. Once the ridge definition was complete, the spin-on glass was removed with a 60 second HF dip. The wafer was then recoated with 111 spin-on glass and baked following the above procedure to prepare it for the next mask step.

When orienting the waveguides to lie in a direction parallel to the major flat of the wafer the InP preferential chemical etch produces ridges with sloped sidewalls. The angle of the slope was measured to be approximately 122°, with the top of the ridges being thinner than their bottom. In the case of ridges orientated 90° to this direction, the chemical etch will produce undercut ridges. Scanning electron microscopy (SEM) was used to study the ridge profiles as shown in Fig. 4.5. For the case of the in-line photodetectors, it was found that the ridge profile was not critical, as will be discussed more in the next chapter. If more vertical sidewalls are desired, a reactive ion etching (RIE) technique can be used which bombards the sample with etching radicals to produce nearly vertical sidewalls [1]. However, RIE is a much more involved process and typically produces a much larger degree of sidewall "roughness,"

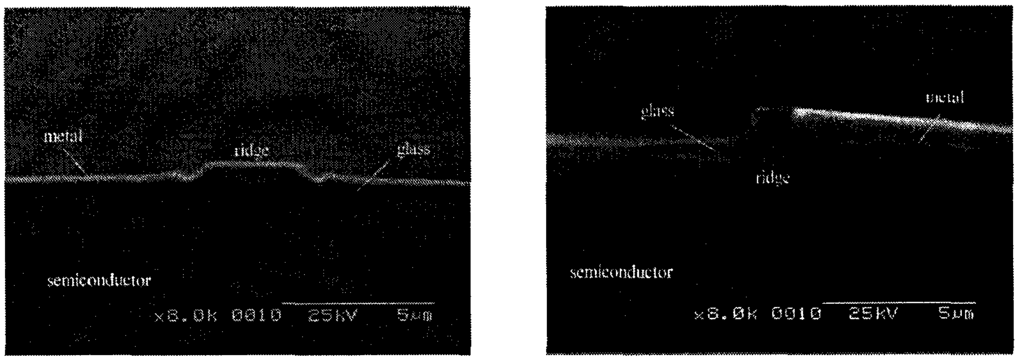

(a) (b)

Figure 4.5: SEM images of ridge waveguide profiles using a preferential HCl : H_3PO_4 etching solution with (a) the waveguides orientated parallel to the major wafer flat and (b) the waveguides oriented perpendicular to the major flat.

leading to increased waveguide propagation loss.

The next step in the fabrication process involves the patterning of the electrical isolation trenches. The previous mask was used to remove the InGaAs and 0.75 μm of the InP materials everywhere except at the locations of the segmented ridges. To define the trenches, only the remaining 0.25 μm of InP needs to be removed in the selected areas. To provide high electrical isolation, the trenches are etched completely through the doped semiconductor layer to the intrinsic InGaAsP core region. The intrinsic material also acts as a stop-etch to the acid used to remove the InP layer. Following the above procedure, the trench etch is performed. The wafer is then recoated using Accuglass 311 spin-on glass which has a higher viscosity than the 111 glass, and is specified to be approximately 3 times thicker. It is spun onto the wafer at 3000 rpm for 30 seconds and was measured to be 3.2 μm thick. It is then baked at 250°C for 24 hours.

After completing the semiconductor patterning, the sample is ready to be prepared for metallization. The first step in this process is to etch contact windows through the 311 silica glass over the top of the ridges. The "windows" mask was designed to contain openings above the waveguide segments that were slightly narrower and shorter in length than the etched ridges. When properly centered, a 0.5 μm border of spin-on glass should encircle the ridges to prevent the deposited metal from making direct contact to the lower semiconductor layers. The wafer is again coated with positive photoresist and patterned. The 311 spin-on glass is slightly over etched with HF to ensure that all of it is removed above the ridges. The photoresist is then removed and a new layer is applied and soft baked.

The final stage for the photolithography is to prepare the wafer for the "lift-off" process. The photomask containing the electrode pattern is aligned to the wafer and vacuum contacted. The photoresist is then slightly overexposed to ensure lift-off (described below) for approximately 4 seconds at 9.6 mW/cm^2. The sample is then soaked in toluene for 7 minutes before being developed.

Metallization

After completing the above described procedures, the sample is placed in an e-beam evaporator for metal deposition on the top surface. The top contact metals used are titanium, platinum and gold of thickness 250, 500 and 1200 $\AA$, respectively. The back surface metals for contact to the n^+ substrate were selected to be nickel, germanium and gold of thickness 250, 450 and 1200 $\AA$, respectively. These metals are chosen as they have been shown to provide excellent ohmic contacts to p-InGaAs [68] and n-InP [69].

After deposition of the top surface contact metals, the wafer is soaked in acetone for approximately 10 minutes. During this process the acetone causes the patterned photoresist to lift off, removing the metal above it. This defines the electrode pattern. It is important that this process is successful. If unwanted metal remains devices may be shorted or not properly isolated. If the metal lifts off where it shouldn't, then contacts may be broken leading to open circuits or lower carrier collection lengths along the ridge. An SEM image of the metallized device after the lift-off process is shown in Fig. 4.6.

Before deposition of the contact metals on the back surface of the wafer, the sample is thinned from approximately 375 μm to 150 μm. This is primarily done for

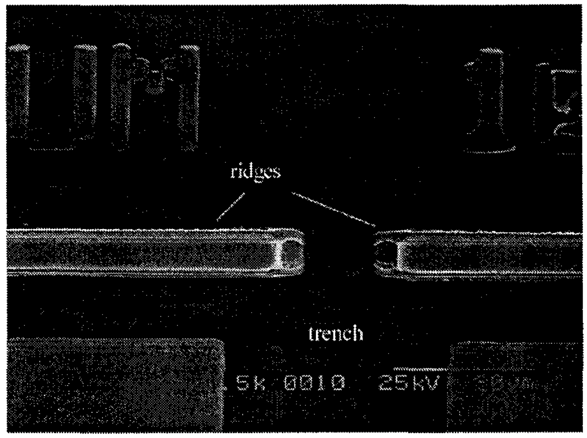

Figure 4.6: An SEM image illustrating the metallized ridges and electrical isolation trenches.

two reasons. Firstly, the thinned wafers will have a lower electrical series resistance due to the reduction in semiconductor material. This is more important to forward biased devices where I^2R heating is significant. The second reason deals with the ability to cleave the wafer into individual devices. It is difficult to obtain good cleaves with an "unthinned" wafer when dicing it into devices of sub-millimeter dimensions. The wafer is thinned using various types of sand paper ranging from 400 to 2400 grit, with the finer sandpapers being used last. Once thinned to 150 μm, the wafer is placed in the metallization chamber to deposit the back surface metals.

After the metallization process the wafer is annealed to improve the electrical contacts. The devices are placed in a rapid thermal annealer at 410° C for 30 seconds. The annealing process helps the n- and p-metals alloy with the semiconductor layers lowering the contact resistance. The physical mechanisms of this process are described in [68] and [69].

Dicing and Mounting

After annealing, the wafer is ready to be cleaved into smaller segments. The in-line photodetectors are too small to be diced into individual detectors so chip sizes of approximately 1x1 mm were cleaved, which contained between 6-12 sets of detector

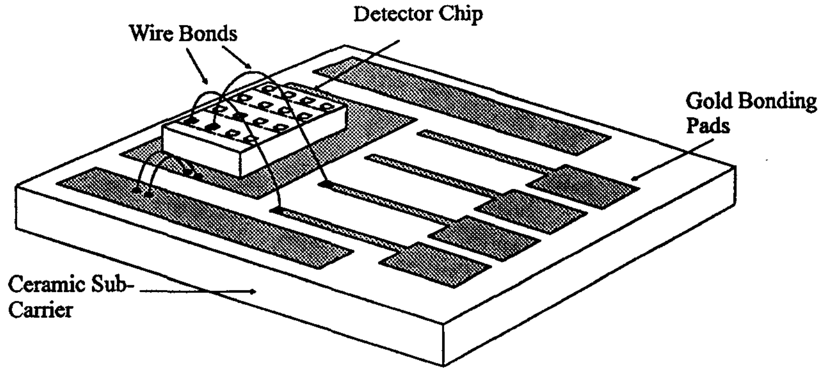

Figure 4.7: An in-line waveguide detector device mounted to a gold plated ceramic carrier with wire bonds attached.

pairs.

Once cleaved, the devices were ready to be tested. As mentioned above, the devices were operated as "bare chip," not being packaged. This is suitable for the laboratory setting but for deployment of these components into external environments, they should be hermetically sealed in a properly designed package. However, a few of the devices were mounted on ceramic carriers containing gold contact pads. The devices were fixed to the mounts using silver conductive paste contacting the n-side metal to the central contact pad on the carrier. The p-side contacts were wire bonded to the outer carrier pads as illustrated in Fig. 4.7. This type of mount offers the advantage of allowing electrical connections to be made to the device without physical contact of the voltage probe to the semiconductor surface, which helps prevent damage and also provides a more reliable connection.

Chapter 5

Experimental Results

In this chapter, a simple wavelength monitoring system based on the electroabsorption properties of InGaAsP quantum wells, is demonstrated. The experimentally obtained results and a detailed characterization of the fabricated devices are provided.

Section 5.1 contains electrical data including the measured dark current, breakdown voltage and electrical isolation between devices. The optical properties are examined in section 5.2, including the waveguide characteristics and the detector responsivities. The performance of the wavelength monitor and the proposed operating modes are described. In addition, the quantum confined Stark effect is shown to be a useful means to significantly extend the device's operating range.

In section 5.2.3, the temperature dependent properties of the technique are discussed and an effective temperature compensation scheme is proposed. Finally, the use of the in-line detectors to monitor multiple incoming wavelengths is examined.

5.1 Electrical Characterization

The current-voltage (I-V) characteristics of p-i-n diodes are critical in determining their behavior and performance. For photodetectors, the reverse bias features are of greater importance as this is the regime in which they operate.

Using a Hewlett Packard 4145A semiconductor parameter analyzer, the electrical properties were measured. The voltage is delivered to the diode via two electrical

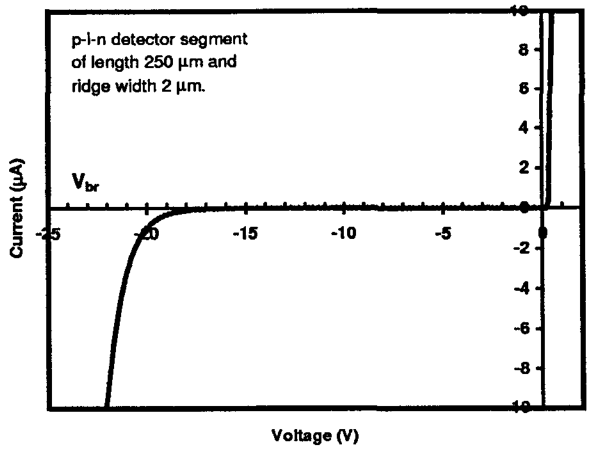

Figure 5.1: The measured I-V characteristic of the waveguide photodetector.

probes used to contact the p- and n-sides of the device. To accurately determine the reverse bias current, it is important to avoid direct exposure of the diode to ambient light due to the effect illustrated in Fig. 3.2. For this reason, the sample is placed in a black box and the external room lights were turned off during the measurement. Approximately 40 devices were tested with varying results. Approximately 10 % of the diodes exhibited very poor reverse bias behavior with premature voltage breakdown and dark currents in excess of 5 μA at - 5V. This can most likely be attributed to localized problems in the device fabrication due to the inevitable presence of surface contaminants that could not be removed during the wafer cleaning process. Particulates composed of hardened photoresist, spin-on glass and dust in the clean room environment add to the contamination. Devices processed near these regions will often exhibit a degradation in performance or total failure. In addition, defects introduced as part of the chemical etching process, excess moisture and poor contact metal adhesion further decrease the wafer yield.

Of the remaining devices, an average dark current of 1.0 $\pm$ 0.5 nA at -5 V reverse bias was observed. The precision of the measurement is limited to the resolution capability of the parameter analyzer. A typical I-V curve for a 250 μm long waveguide segment with a 2 μm wide ridge is illustrated in Fig. 5.1. The measured breakdown voltage of the diode is -24 $\pm$ 1 V defined for a reverse current of 0.1 mA. Taking the impurity concentration of the intrinsic region to be 5×10^{15} cm^{-3}, corresponding to the estimated background doping level for the MBE system used to grow the material, Eqs. 3.1-3.3 can be solved to find the depletion region width. Assuming a uniform electric field in the intrinsic region, a breakdown field of $F_b = 423 \pm 17$ kV/cm is obtained. The relatively large value of F_b and the sharp "knee" observed near breakdown, indicate that the material quality is high, containing few defects, and that the diode has been well processed.

Avalanche breakdown occurs when electrons and/or holes acquire enough field induced kinetic energy to impact ionize other atoms in the lattice producing additional carriers which can participate in the ionization process. The condition for avalanche breakdown in a p-i-n doped diode structure can be written [70]:

$$\frac{\beta}{\alpha} = e^{(\beta-\alpha)w} \tag{5.1}$$

where β and α are the impact ionization coefficients for holes and electrons, respectively, and w is the width of the depletion region. The ionization coefficients represent the average number of ionizing collisions per unit length and have been reported to be:

$$\begin{aligned} \alpha &= 3.37 \times 10^6 e^{-2.29\times10^6/F} \qquad (cm^{-1}) \\ \beta &= 2.94 \times 10^6 e^{-2.40\times10^6/F} \qquad (cm^{-1}) \end{aligned} \tag{5.2}$$

for InGaAsP ($E_g \sim 0.92$eV) [71]. Solving Eqs. 5.1 and 5.2 results in a predicted breakdown field of F = 452 kV/cm which is within 7 % of the experimentally measured value. The quantum wells are ignored in this calculation.

To examine the electrical isolation between detector segments the voltage probes are connected to the tops of two consecutive ridge contacts. The leakage current between segments is then measured as the bias voltage is varied. The I-V characteristic of two 250 μm long waveguides, separated by a 10 μm wide trench, is shown in Fig. 5.2. It is seen that the curve is nearly symmetric about the zero voltage point indicating that the I-V characteristics of the two detector segments are similar. The leakage current is measured to be 1.0 ± 0.5 nA at $\pm$ 5 V which is equal to the measured leakage current of a single detector element (within the instrument resolution).

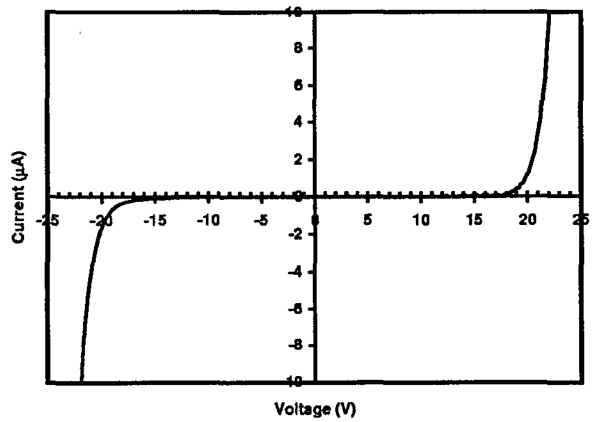

Figure 5.2: The measured leakage current between two in-line waveguide segments separated by a 10 μm wide isolation trench.

This indicates that the etched trench provides a very high degree of electrical isolation with no measurable leakage occurring between waveguide elements. Segments separated by 5 μm wide trenches were also designed and displayed similar results.

5.2 Optical Characterization

The characterization set-up used to examine the optical properties of the fabricated devices is illustrated in Fig. 5.3. It was constructed on a "floating" optical bench to shield against vibration. A New Focus 6200 series tunable laser system with a 1525-1575 nm tuning range was chosen as an optical source. The laser output was directed to pass through a free space optical isolator before being coupled into a 1550 nm single mode optical fiber. The fiber is wound around three pivoting circular paddles which allows the in-fiber polarization to be controlled. 90 % of the coupled light was then tapped off using a 90:10 fiber y-splitter and directed to an optical power meter which monitored the light level in the fiber. The remaining 10 % of the signal was coupled into the semiconductor device utilizing a tapered fiber patch cord, purchased from Namiki Precision Jewel Co., whose end is mechanically polished to produce a very fine circular tip of a 5 μm radius. The fiber tip acts as a lens to increase the coupling efficiency into the semiconductor waveguide. The devices were

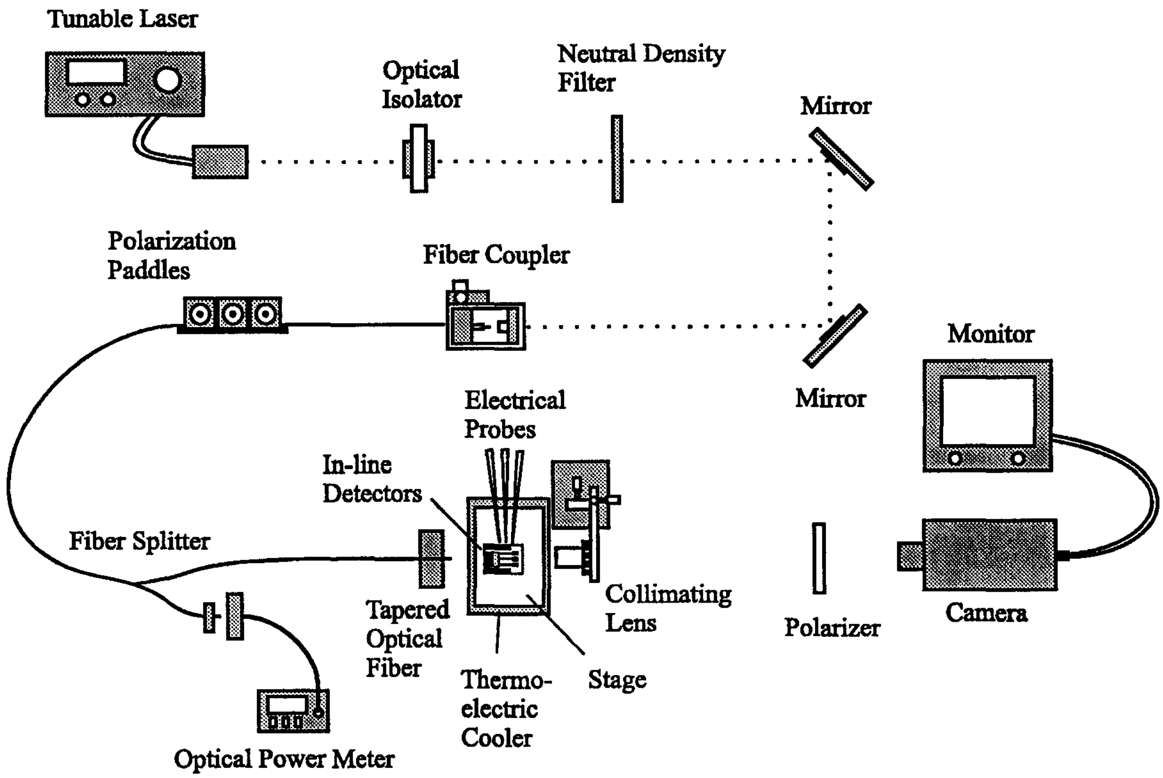

Figure 5.3: The optical characterization set-up used to test the in-line detectors.

mounted on a copper stage with a built-in thermistor and thermo-electric cooler to monitor and control the temperature. Finally, a collimating lens and an infra-red camera were used to observe the near field output of the rear waveguide facet.

The first qualities investigated were the optical waveguide characteristics. Single and segmented waveguide outputs were observed on the infra-red camera for both TE and TM polarizations. All of the devices exhibited single mode behavior in the growth direction, agreeing with the modelling results.

For devices with ridges etched perpendicular to the major wafer flat, all of the waveguides were found to be single mode in the x-direction (lateral direction). However, the 2 μm wide ridges were observed to provide poor optical confinement for the TE mode. This is believed to be due to the decrease in ridge width at the base of the waveguide, resulting from the undercutting effect observed in Fig. 4.5. The 3 and 5 μm waveguides, exhibited better mode profiles, being more strongly confined to the core region.

For the waveguides etched in a direction parallel to the major wafer flat, the sloped sidewalls increased the average ridge width relative to the value used in the simulations. It was observed that the 2 μm wide waveguides were single mode and provided strong optical guidance for both TE and TM polarizations, whereas the 3 and 5 μm guides were found to support two transverse TE and TM modes. These results were encouraging as the performance of the wavelength monitor could be examined for both single and multi-mode waveguides. Unless otherwise stated, the data presented below pertains to devices with ridges etched parallel to the major wafer flat. The observed near field TE mode images for a waveguide containing a 5 μm wide ridge, are shown in Fig. 5.4.

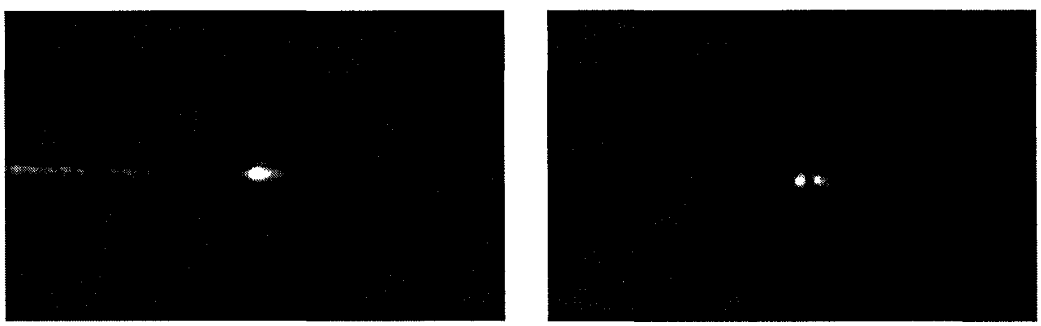

(a) (b)

Figure 5.4: Near field camera images of TE waveguide modes for a 5 μm ridge width: (a) excitement of the first order mode (b) excitement of the second order mode.

5.2.1 Single Wavelength Operation

A two stage amplifying circuit was designed to examine the photodetection properties of the device. The circuitry essentially consists of a transimpedence amplifier followed by a low noise voltage amplifier with a combined gain of 10^7 V/A. The photodetector output was directly connected to the input of the transimpedance amplifier which converted the small photocurrent to a voltage. The voltage was then amplified by the voltage amplifier and measured on a DC multimeter. Two identical amplifying paths were used, one for each of the in-line detector segments. The electronic circuit is described in detail, in appendix A.

Using a tunable diode laser, the front and rear detector responses to wavelength were measured. Fig. 5.5a shows the obtained results for a device containing two 500 μm long waveguide segments, each with a 3 μm wide ridge. The measured photocurrents are converted to detector responsivities by normalizing to the input power delivered to the device, which had a mean value of 5 μW across the laser's tuning range. The fiber coupled laser power was measured using an Newport optical power meter placed behind a fiber y-splitter. The maximum detector responsivity was measured to be 0.22 A/W near 1535 nm, which is relatively low compared to that of receivers optimized for optical communications (typically $\Re \sim 0.4 - 0.8$ A/W). However, this value is more than sufficient for the current application. At a wavelength of 1535 nm, Eq. 3.8 yields the maximum upper limit of $\Re$ to be 1.24 A/W, assuming a 100 % external quantum efficiency. If Fresnel reflections are taken to be 30 % and the quantity defined in Eq. 3.9 to be 1, a fiber-to-waveguide coupling efficiency of 25 % is estimated. This value is typical for a tapered fiber used with common InGaAsP/InP waveguide structures. If an increased value of $\Re$ is desired, anti-reflection coatings can be applied to the device facet or improved fiber-to-waveguide coupling methods can be utilized. Furthermore, a small increase may be obtained by increasing the number of quantum wells in the layer structure, altering the waveguide design to obtain a larger optical confinement factor, or by the use of longer waveguide segments.

The front detector displays a typical semiconductor quantum well absorption band edge, centered near 1.55 μm, which matches the original target wavelength. The measured band edge is sharp, extending over an approximately 35 nm range indicating that the material quality is high and the quantum well layers are very uniform. Fig. 5.5a also illustrates the filtering action of the front detector. When the absorption coefficient is large, the front detector is highly absorbing and little optical power can reach the second detector segment. At longer wavelengths, where the front detector becomes less absorbing, more light is able to reach the rear segment and its photocurrent increases. It continues to increase with wavelength until the effect of

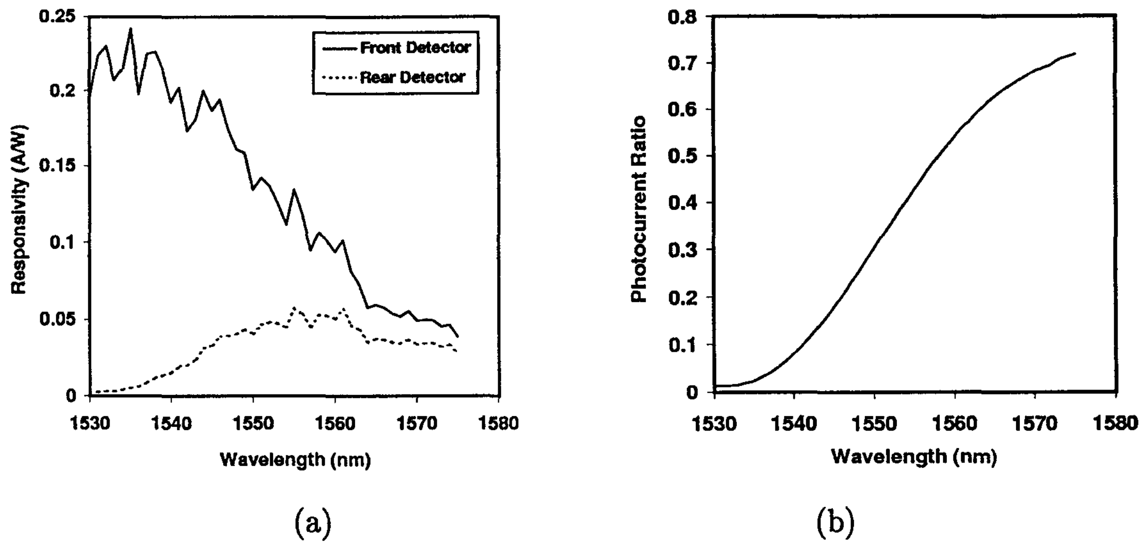

Figure 5.5: (a) The individual detector segments response to wavelength for TE polarized light. (b) The ratio of the rear to the front detector element's photocurrent verses wavelength. Both detector elements are held at zero voltage bias.

the decreasing absorption coefficient becomes dominant. The fluctuations observed in Fig. 5.5a are due to the power instability of the tunable diode laser source used to characterize the devices.

By adding a voltage divider chip to the amplifying circuit, the photocurrent ratio response was measured. Fig. 5.5b displays the ratio of the rear to front detector photocurrents when both elements are held at zero voltage bias. It can be seen that this is a smooth function of wavelength and despite the laser power fluctuations observed in Fig. 5.5a, the ratio remains unaffected, illustrating its independence of optical input power. The photocurrent ratio response is a rapidly increasing function of wavelength exhibiting a slope of 2.5 %/nm at 1.55 μm. The useful operating range of the device is approximately 35 nm, being limited by the extent of the absorption band edge. This covers a significant portion of the C-wavelength band (1530-1565 nm) used in fiber communication systems. At longer wavelengths, the device response saturates, being limited by the waveguide and scattering losses.

The wavelength sensitivity of the technique was found to be very high. The gain in the divider circuit was set so that an output of 10 V corresponded to a photocurrent ratio of 1. Near 1.55 μm, the measured divider circuit output rms noise was 0.55 mV. Based on the measured wavelength dependence of the photocurrent ratio, this corresponds to a wavelength sensitivity of 2.2 pm. The rms noise varied from 0.38 mV to 1.5 mV across the device's operating range, being lowest near the center. A mean rms noise value of 0.74 mV was measured which corresponds to an average wavelength sensitivity of 3 pm. Approximately 5 μW of optical input power and an electrical averaging time of 0.2 s, was used for the measurement. The demonstrated wavelength sensitivity ranks very highly among other reported monitoring schemes based on the use of optoelectronic semiconductor components.

A laser's output power usually fluctuates rapidly over time and in many cases, the light intensity exiting a given port in a fiber network is unknown. It is therefore essential that a wavelength monitor function independently of optical input power. By taking the ratio of photocurrents, the power dependence of the individual detector signals factors out, as illustrated by Eq. 3.15. By attenuating the optical input power using a variety of neutral density filters, the power dependence of the photocurrent ratio was measured. The results are shown in Fig. 5.6 for a fixed wavelength of 1548 nm. It was observed that the device's output varied by less than 0.4 % when attenuating the input signal from 30 to 1 μW and by 3.7 % over the entire designated range. The exhibited power dependence is thus very low, but the photocurrent ratio's noise level increases with increasing signal attenuation. A wavelength sensitivity of 22 pm is obtained at 1.55 μm with the signal attenuated to 0.1 μW. It was also found that the power dependence of the technique was sensitive to the fiber-to-waveguide coupling conditions. Light not coupled into the waveguide mode can induce unwanted photocurrents due to scattering and reflections from the layer surfaces, influencing the measurement. Therefore, a high quality tapered fiber is required to achieve the specified performance.

Several devices of varying dimensions and locations on the wafer were tested. There was a 3 nm wavelength variation in the location of the band edge, observed for devices grown at extreme ends of the 2 inch wafer. This is believed to be due to slight variations in layer thicknesses, doping concentrations and etch depths.

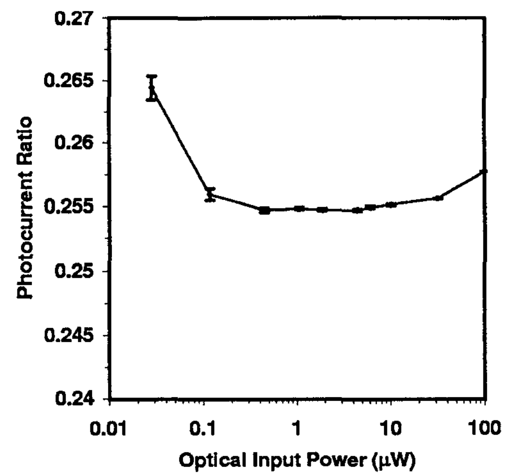

Figure 5.6: The measured power dependence of the photocurrent ratio.

Measurements were made for detectors containing different isolation trench widths, segment lengths and ridge widths. Devices with 5 and 10 μm wide trenches were fabricated, and no substantial differences in their performance could be observed. Waveguides having ridge widths of 2, 3 and 5 μm were also examined. It was found that the ridge width was not critical in determining device performance, but the fiber-to-waveguide coupling conditions were significant. Despite the ridge width or number of lateral modes supported by the waveguide, the devices functioned with a performance similar to that observed in Fig. 5.5b. However, the multi-mode waveguides were found to be more strongly influenced by the optical coupling conditions from the fiber into the waveguide. By varying the position of the input fiber, the partition of the optical energy into the two supported TE modes can be altered. This effect can be viewed as a change in the combined optical confinement factor between the optical field and the quantum wells, leading to a change in the total attenuation coefficient. A variation of 21 $\pm$ 6 % in the photocurrent ratio value was observed when the coupling was moved from the center of a 5 μm ridge waveguide, where the excitement of the first order mode is at a maximum, to a position to maximize the coupling to the second order mode. For the 2 μm single mode waveguides, the photocurrent ratio varied by only 4 $\pm$ 2 %, when the fiber was displaced horizontally from the waveguide center to its edge. Therefore, it is important to maintain consistent optical coupling into the waveguide detectors, especially for multi-mode structures. This can be accomplished by fixing or "pigtailing" the input fiber to the device using a suitable epoxy compound.

The influence of varying the length of waveguide sections was also investigated. Detector segments of lengths 100, 250 and 500 μm were fabricated. It was observed that the photocurrent ratio response was shifted to longer wavelengths for longer detector segment lengths. This effect is predicted by Eq. 3.15 which illustrates the ratio's exponential dependence on this parameter. A wavelength shift of 17 $\pm$ 3 nm was measured for a segment length change from 100 to 500 μm. This effect is useful to optimize the detector response for a given wavelength range and will be discussed further in section 5.2.4.

Polarization Sensitivity

The polarization state of light emerging from a fiber cable is usually unknown. This can be due to bending and twisting of the cable or from irregularities in the fiber which have the effect of scrambling the signal polarization. Therefore, when designing optical components for use in fiber systems, it is critical that they function with low polarization dependence.

To accomplish this, the wavelength monitor was designed to absorb a single polarization only, over the wavelength range of interest. As discussed in chapter 2, the use of compressively strained quantum wells can induce a significant wavelength separation between the absorption band edges for TE and TM polarizations. For the current structure, the absorption band edge for TE polarized light is in the vicinity of 1.55 μm. TM light near this wavelength will not contribute towards photocurrent since the TM band edge is located at a much shorter wavelength of 1.34 μm. Therefore, the ratio of photocurrents is solely determined by the TE component within the optical signal. The effect of varying the input polarization is then to stimulate a change in the amount of absorbed optical power. Since the photocurrent ratio is power independent, it will be polarization independent as well. However, the signal-

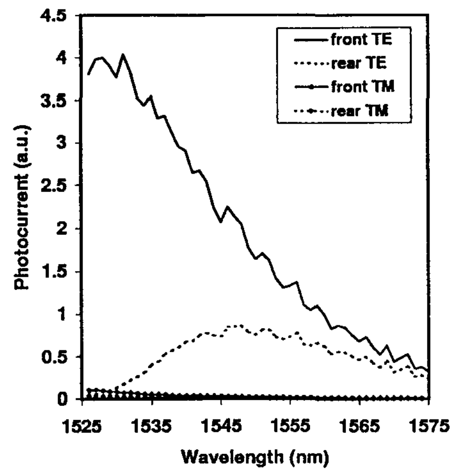

Figure 5.7: Photocurrent generated in the front and rear waveguide segments for both TE and TM polarizations.

to-noise ratio of the detector will vary, being a maximum for pure TE polarization at a given optical power level.

Fig. 5.7 illustrates the generated photocurrents for two 250 μm long in-line detector segments for TE and TM signals. It is seen that the absorption data labelled TM is small, being over 45 times less than that of the TE signal. This nearly corresponds to the highest degree of polarization obtainable using the fiber polarization control paddles. Therefore, the measured TM absorption results almost completely from residual TE light within the signal that cannot be removed. This was confirmed by observing that the band edge of the TM labelled signal was located in the same position as that of TE. By taking the long wavelength limit of the TM labelled photocurrent (where TE absorption is assumed to be zero), the photocurrent generated by TM light was found to be over three orders of magnitude less than that of the maximum TE signal.

5.2.2 Reverse Bias Tuning

The above sections have described a compact, simple and potentially low cost device capable of providing high resolution wavelength discrimination over an approximately 35 nm operating range. The obtained results were very encouraging as

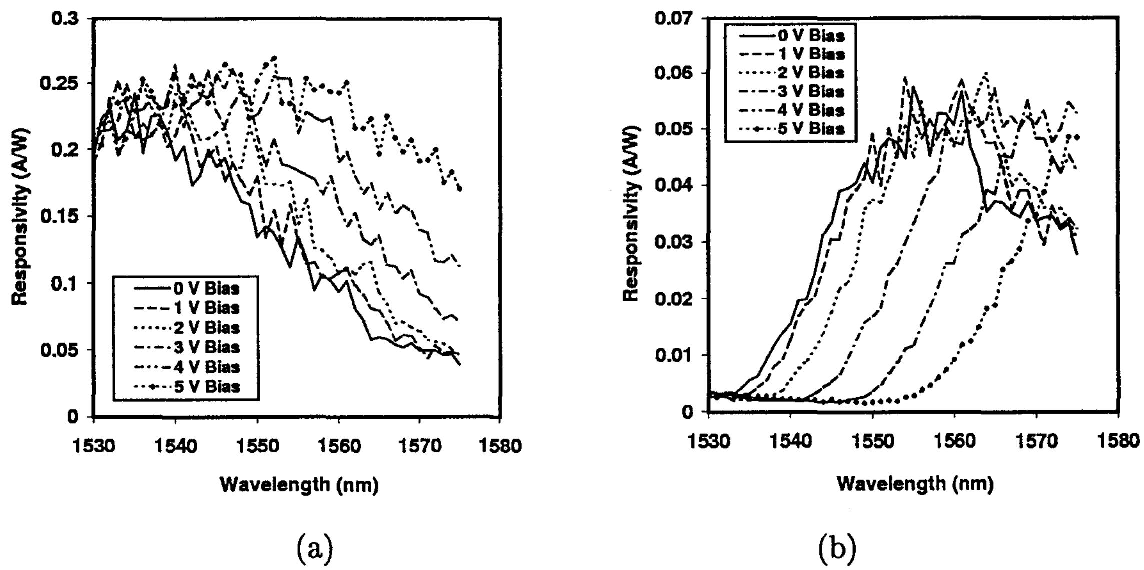

Figure 5.8: (a) Front detector responsivity near the band edge for several values of reverse bias. (b) Rear detector responsivity for several values of reverse bias.

the sensitivity of the technique was demonstrated to provide near pm wavelength resolution for optical input powers as low as a few μW. The operating range is determined by the extent of the absorption band edge and is suitable for many potential applications. However, applications such as wavelength monitoring in WDM systems may require a larger working range of up to, and exceeding 50 nm.

To accomplish this, electroabsorption tuning of the quantum well band edge via the QCSE can be utilized. This effect is commonly used to modulate the transmission of electroabsorption modulators and is described in chapter 2. By applying a reverse bias to the individual waveguide segments, the detector responsivities are shifted to longer wavelengths due to the induced distortion of the quantum well potentials. This effect is seen in Fig. 5.8 for both the front and rear detector elements for five different values of reverse bias voltage, varying between 0 and -5 V. In practice, a positive voltage is used and applied to the n-type substrate of the detector to act as a reverse bias. It is seen that the absorption band edge shifts by 25.0 $\pm$ 0.5 nm and remains sharp when reversed biased at -5 V.

By biasing both detector elements at the same value, the photocurrent ratio re-

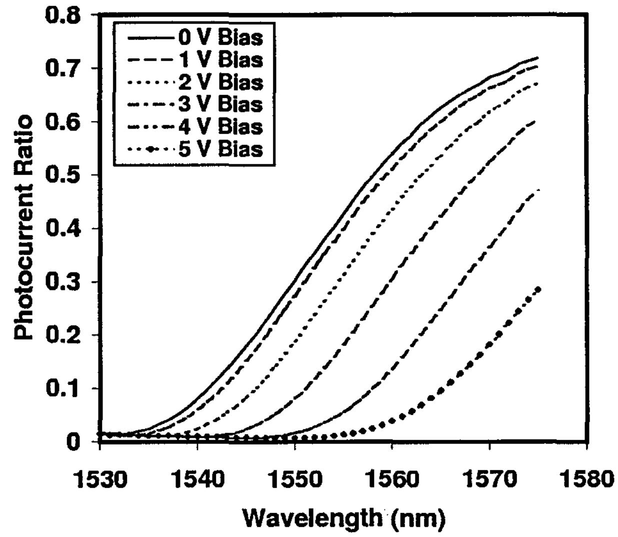

Figure 5.9: Ratio of the rear-to-front detector element's photocurrent for several values of reverse bias.

sponse can be tuned in a similar way. This is illustrated in Fig. 5.9. Thus, to monitor a given wavelength an appropriate reverse bias can be chosen to optimize the device's response. In this manner, the operating range of the wavelength monitor has been extended by 25 nm.

Active Locking Mode

The normal operation of the wavelength monitor involves measuring the ratio of photocurrents generated between two in-line waveguide segments and tuning the detector band edge with reverse bias to select the device's operating range.

An alternative method involves using a comparator circuit and actively locking the device to a fixed photocurrent ratio by controlling the reverse bias voltage. In this configuration, one of the detector amplifiers is selected to have a variable gain while the other remains fixed. By changing the gain of one of the detector amplifiers, the locking point can be varied. The amplified photocurrent signals are fed into the inputs of a difference amplifier which generates a feedback voltage that is proportional to their difference. The feedback voltage is then applied as the bias voltage to both

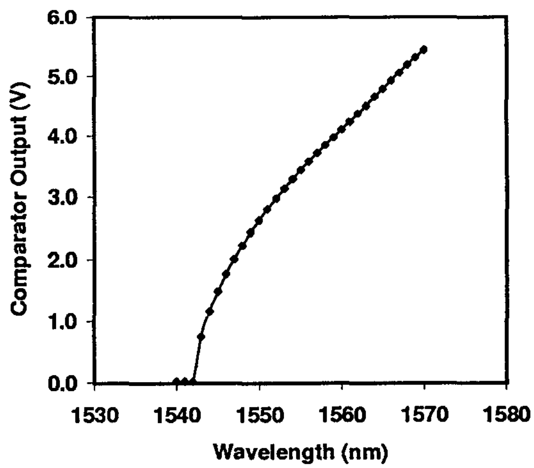

Figure 5.10: Comparator output to lock the photocurrent ratio to a set value of 0.12.

segments of the wavelength monitor, locking the photocurrent ratio to a preset value. In reality, a positive feedback voltage is used and applied to the n-type substrate of the detector to act as a reverse bias. As the wavelength changes, so must the comparator output to maintain the set locking point. The feedback voltage is highly dependent on wavelength near the detector band edge, and becomes the measured parameter. A more detailed description of the comparator circuit is provided in appendix A. Fig. 5.10 shows the comparator output as a function of wavelength when the photocurrent ratio is locked to a value of 0.12. An average rms noise level of 0.87 mV was recorded across a 30 nm operating range. This corresponds to an average wavelength resolution of 5 pm for this mode of operation. 5 μW of TE polarized input light was utilized for this measurement.

5.2.3 Temperature Compensation

The demonstrated wavelength monitoring technique is based on the sharp transition in optical absorption near the band edge of a quantum well material. Therefore, the approach is dependent on the thermal sensitivity of the material band gap. The temperature dependence (dE_g/dT) for $In_{1-x}Ga_xAs_yP_{1-y}$ has been reported to be -4.0 + 0.3y ($\times 10^{-4}$eV/°K), which is obtained from a linear interpolation [28]. For the

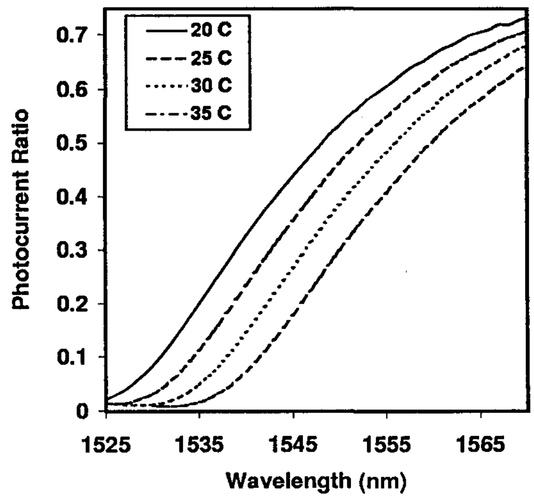

Figure 5.11: The measured photocurrent ratio response for several values of device temperature.

current material structure (x=0.81), a shift of -3.76 $\times 10^{-4}$eV/°K is obtained which corresponds to a wavelength shift of 0.73 nm/°C at 1.55 μm. This agrees well with the measured shift of the photocurrent ratio response which was observed to tune at approximately 1.8 $\pm$ 0.1 %/°C, corresponding to a wavelength shift of 0.72 $\pm$ 0.03 nm/°C. The photocurrent ratio taken between two 250 μm long detector segments for various temperatures is shown in Fig. 5.11. It is seen that the absorption band edge remains sharp over this temperature range with no significant change in slope.

The detector's thermal sensitivity is relatively large and precise temperature control is required for high resolution monitoring. A control of a few mK's is needed for the device to operate with picometer precision. The temperature dependence of the wavelength monitor hinders its ability to provide absolute measurement and can be detrimental for applications where high precision temperature control may not be practical. To overcome this problem, a unique self-correcting temperature compensation scheme was developed which makes use of a fixed reference wavelength and active locking of the photocurrent ratio. Fig. 5.12 illustrates the principle. One channel of an array of in-line detectors is dedicated to a fixed reference wavelength and the comparator circuit described above, is used to lock the photocurrent ratio to a

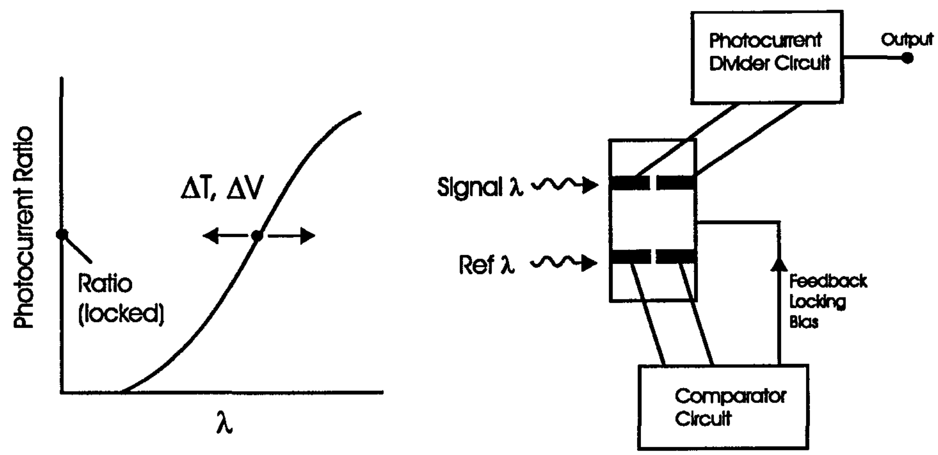

Figure 5.12: A schematic of the temperature compensation scheme using a minimum of two sets of in-line detectors and a single reference wavelength.

set value. As the temperature changes, the comparator output must change to maintain the fixed ratio. This has the effect of electrically shifting the absorption band edge by an amount that almost exactly cancels any thermally induced shift. A 1555 nm distributed feedback laser was used to provide the reference wavelength, and the photocurrent ratio was locked to a value of 0.12. To accomplish this, the comparator must output a reverse bias of 3.5 V at room temperature. As the device temperature increases, the comparator feedback bias drops to maintain the locking condition. For negative temperature changes the feedback voltage must increase. The comparator output as a function of temperature for a device containing 500 μm long detector segments and a 2 μm wide ridge, is shown in Fig. 5.13a. All other sets of in-line detectors in the array are monitored using standard photocurrent divider circuits. By applying the same comparator output bias to all sets of in-line detectors in the array, the photocurrent ratio outputs are simultaneously self corrected for temperature fluctuations using a single reference wavelength. The temperature compensated detector results are shown in Fig. 5.13b. For these data, two sets of 500 μm long detector pairs, with a lateral separation of 250 μm, were used with a reference wavelength of 1555 nm and a signal wavelength of 1560 nm. The temperature compensation method reduced the temperature dependence of the device to less than 2% of its uncompensated sensitiv-

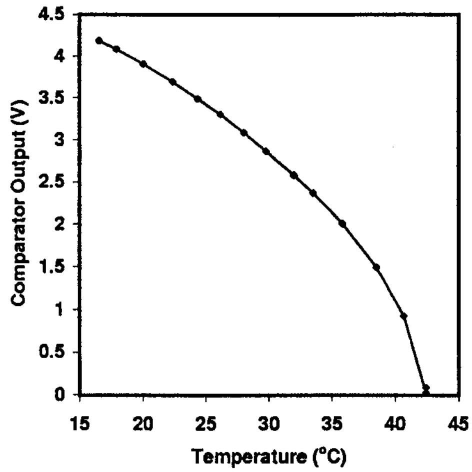

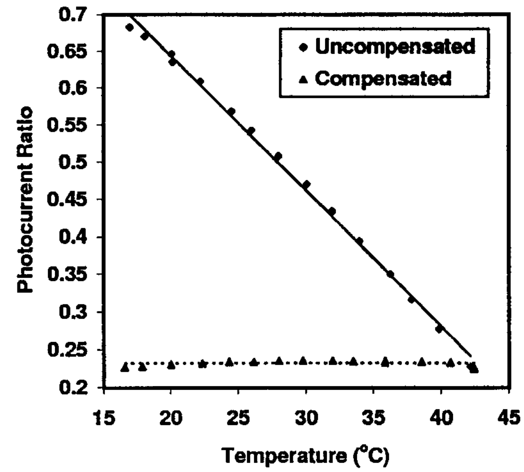

Figure 5.13: (a) Comparator output to lock the photocurrent ratio to a set value as a function of device temperature. (b) The photocurrent ratio's thermal dependence for compensated and uncompensated operation.

ity. However, the noise level increased at a given temperature, to limit the average wavelength resolution of the measurement to 10 pm.

5.2.4 Multi-Wavelength Operation

Single wavelength operation is suitable for applications such as back facet laser monitors and single channel wavelength meters. However, for multiplexed systems several wavelengths must be monitored simultaneously. For multi-channel operation, an array of detector elements can be combined with a wavelength demultiplexer. The demultiplexer separates the various channels so that each element in the array receives only a single wavelength. Due to the large operating range of the devices an array of detectors (fabricated on the same wafer) is able to cover a significant portion of the currently used WDM wavelength spectrum. Since the devices consist only of straight waveguide segments, arrays containing a large number of elements can be fabricated while the chip size remains relatively small. The detectors may be placed behind fiber demultiplexers or monolithically integrated with InP based arrayed waveguide gratings. They could potentially monitor the signal wavelengths within each demultiplexer channel. This function is becoming increasingly important for WDM systems as the channel spacings are continually becoming smaller over time and tighter control of the channel wavelengths is required.

Several different modes of operation are possible. One possibility involves holding all of the detector pairs in the array at the same bias voltage, and the wavelength at each pair is then determined by a measurement of the photocurrent ratio. One detector pair can be used in combination with a fixed frequency reference laser to temperature compensate the entire array, as described above. The overall optical bandwidth of a system operating in this mode is 35 nm, being limited by the extent of the absorption band edge. In the second mode of operation, the reverse bias voltage is varied from one detector pair to the next within the array. Since the response curve tunes with the bias voltage (see Fig. 5.9), this permits optimization of each channel for its particular wavelength range. This makes it possible for the overall operating range of the array to be extended past 60 nm, but it becomes more difficult to use the active locking technique to temperature stabilize the device since all sets of detectors are held at different biases.

An alternative way to shift the response curve from one detector pair to the next is to vary the length of the detector segments rather than varying the bias voltage. As the waveguide segment length was increased, the photocurrent ratio response was found to shift to longer wavelengths due to the $e^{-\alpha L}$ dependence illustrated in Eq. 3.15. A photomask was constructed containing sets of detector pairs of successively increasing lengths, as illustrated in Fig. 5.14a. The photocurrent ratio behavior for in-line detector pairs of segment lengths 293, 445, 596, 750 and 900 μm at 0 V bias is displayed in Fig. 5.14b. It is seen that the wavelength monitor response has been shifted by 15 $\pm$ 1 nm over this length variation.

Light may be simultaneously coupled into the multiple detector pairs using an array of incoming fibers (see Fig. 5.15). Such an array was purchased from Wave Optics Inc., containing four lensed fibers set in silicon v-grooves and covered with a glass plate. The fiber ends were positioned to protrude an equal distance from the silicon wafer and have a horizontal separation of 250 μm. The photomask was

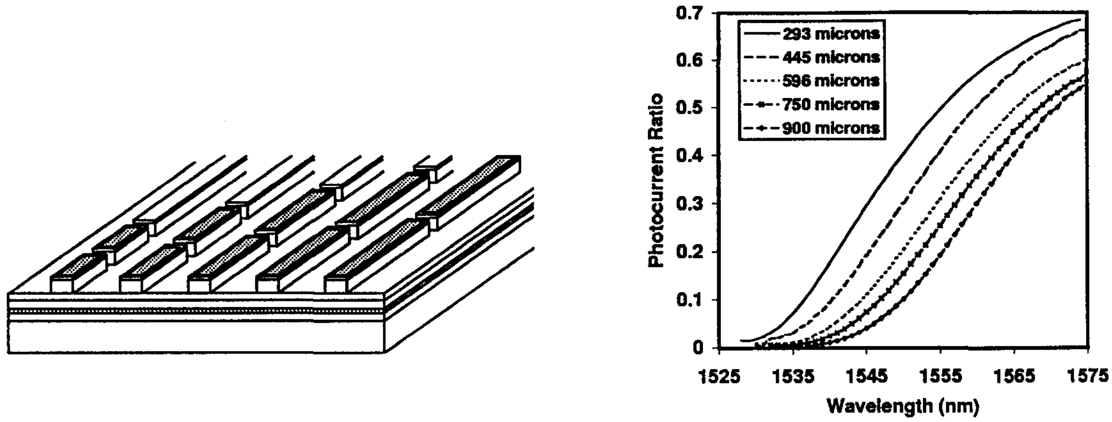

(a) (b)

Figure 5.14: (a) Detector array consisting of in-line waveguide pairs of varying length. (b) Measured photocurrent ratio response at 0 V bias, for various detector segment lengths.

designed based on the fiber array dimensions, having adjacent detector pairs separated by 250 μm. The detector chip size remained relatively small, being limited by the incoming fiber separation. To monitor 11 wavelengths, a chip size of 2 x 3 mm is required. To monitor N-wavelengths, a chip size of 2 x [0.25(N+1)] mm is needed.

By selecting the proper lengths of elements in the detector array, the individual sets of wavelength monitors can be optimized for a specific wavelength channel. In this manner, all sets of detectors in the array can be held at the same bias voltage, which is either preset or determined by the comparator circuit. Since all detector pairs are held at a common bias, the temperature compensation procedure can straightforwardly be applied.

With equal amounts of optical power coupled into 2 adjacent waveguide segments, the crosstalk between them was determined. Ten independent trials were made, each attempting to optimize the fiber-to-waveguide alignment visually on the infra-red camera. The average measured crosstalk was -33 $\pm$ 8 dB which is very low and sufficient for most applications. If desired, it can be decreased further by improved optical coupling to the device or by increasing the adjacent detector distance. The

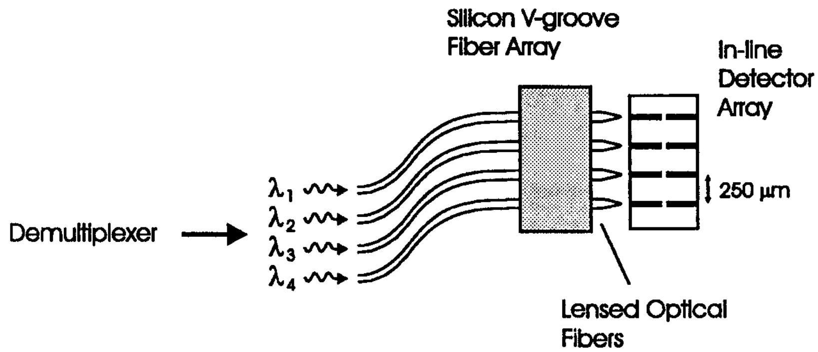

Figure 5.15: Lensed fiber array used for optical coupling to an array of in-line detectors.

crosstalk is dominated by stray light that does not couple into, or is scattered by the adjacent waveguide segments. Multi-wavelength operation will be examined further in chapter 6.

5.3 Summary

In summary, a simple wavelength monitor for use near 1.55 μm has been demonstrated which is based on the electroabsorption properties of InGaAsP quantum wells. The devices simply consist of two waveguide photodiodes of equal segment length fabricated along a common ridge waveguide channel. The ratio of the photo-generated currents is taken as a measure of the input wavelength. High resolution operation was exhibited with a wavelength sensitivity of better than 3 pm for optical input powers as low as 5 μW. This technique offers the advantages of wavelength filtering, power splitting and photodetection all in one compact and simple device. By applying a reverse bias to the detectors, the absorption band edge of the quantum wells can be tuned over a range exceeding 25 nm. This allows the total operating range of the device to extend past 60 nm.

Two modes of operation were presented. The standard method consists of monitoring the photocurrent ratio between two in-line waveguide photodetectors as a measure of wavelength. The detectors are biased to select an appropriate operating range. In the second operating mode, the photocurrent ratio is fixed to a set value by using an active locking technique. This is accomplished with the use of a comparator circuit that generates a feedback bias to shift the detector's absorption band edge via the quantum confined Stark effect. This feedback signal then becomes the measured parameter.

The dependence of the technique on optical input power was examined and the photocurrent ratio was found to vary by less than 4% over a power variation of 2.5 orders of magnitude. Between 1 and 30 μW, the ratio varied by only 0.4 %.

The polarization dependence of the devices was found to be very low. The transition selection rules for the quantum wells allow the device to absorb only one polarization over the wavelength range of interest. The current detector structure was designed to absorb TE polarized light near 1.55 μm while remaining transparent to TM. The photocurrent ratio is then exclusively determined by the TE component of the incoming optical signal, allowing it to function independently of the polarization state.

The detectors were originally designed for single wavelength operation. This is desirable for many applications, but for others the simultaneous monitoring of several wavelengths is necessary. The use of the devices for these purposes was investigated. By using an array of in-line detectors and a wavelength demultiplexer, which separates the incoming wavelengths and directs them to the individual detector pairs, the wavelength monitors can track the positions of the wavelengths within each of the demultiplexer's pass bands. Since the operating range of the devices is large, an array of in-line detector pairs fabricated on the same wafer can be used to monitor several incoming channels simultaneously. The simplicity of the device's geometry allows large detector arrays to be fabricated while maintaining a relatively small chip size and a large wafer yield. The dimensions of the array are limited by the separation of the incoming fibers.

Since the technique involves working near the absorption band edge of the incorporated quantum wells, its thermal sensitivity is determined by the temperature coefficient of the material's band gap. This value is relatively large for InGaAsP, corresponding to a shift of -0.73 nm/°C. An effective temperature compensation scheme was developed to overcome this limitation. It consists of dedicating one detector pair in an array of in-line detectors to a fixed reference wavelength. A comparator circuit is used to generate a reverse bias feedback signal to actively lock the the photocurrent ratio to a set value by electrically shifting the absorption band edge by an amount to cancel the thermally induced shift. All sets of detectors in the array can then be compensated for temperature fluctuations by applying the comparator output to their common base electrode.

The effects of varying the isolation trench width, the waveguide width and the segment lengths were investigated. By increasing the length of the detector sections, the photocurrent ratio response curve could be shifted to longer wavelengths. It was found that the processing tolerances were very relaxed for the devices as the effects of doubling the isolation trench width and varying the waveguide dimensions did not significantly impact their performance.

Chapter 6

Applications to Optical Sensing

6.1 Introduction

Optical strain sensors based on intra-core Bragg gratings provide many important advantages over more conventional resistive strain gauges including an immunity to electromagnetic interference, passive operation, light weight and a high resistance to corrosion [9]. Significant interest has been generated in the application of these elements to "smart structure" development. This has been a rapidly expanding field in which sensors are implemented in civil or mechanical structures to provide an internal monitoring network. Fiber Bragg gratings (FBGs) are well suited for these applications as they can be easily adhered to, or embedded within composite materials, have an inherent self-referencing capability and offer the ability for distributed sensing. Using this technology and a communications link, parameters such as strain, temperature, vibration and the general condition of a structure may be remotely monitored, eliminating the need for costly on-site inspections.

This chapter explores the application of the wavelength monitors to the area of fiber Bragg grating strain sensing. In particular, the devices are used to monitor the back reflection of a FBG which is bonded to a mechanical structure subjected to static and dynamic strains. Section 6.2 briefly discusses the important fundamentals of FBGs including their spectral characteristics and fabrication, while the basic principles outlining the use of these components as sensing elements are described in section 6.3. An experimental demonstration of the wavelength monitors acting as key elements in these systems is presented. Two main configurations are explored including a broadband illumination scheme, and a tunable laser approach.

6.2 Fiber Bragg Gratings

The photosensitive properties of germanium doped fibers have been exploited to develop new and useful components for fiber optic systems. One such component is the fiber Bragg grating which can function as a highly reflective narrowband optical filter of subnanometer bandwidth [10]. They are commonly used for optical add/drop filtering of WDM system channel wavelengths, optical routing, dispersion compensation and for fiber sensing. By varying numerous physical parameters during the fabrication process, the grating's spectral features including the center wavelength, optical bandwidth, peak reflectivity and spectral lineshape can be tailored to suit a desired application.

A fiber Bragg grating consists of a periodic variation of refractive index photoinscribed within the core of an optical fiber. Presently, the most common production method employed in their fabrication is the optical phase mask technique [72]. This is illustrated in Fig. 6.1. A phase mask consists of a silica plate in which a surface relief grating is defined using photolithographic methods. Ultraviolet (UV) light produced from a coherent source such as an excimer laser, is directed normally through the phase mask whose etched corrugations are designed to suppress the zeroth order diffraction and to channel the optical power into the +1 and -1 orders. The first order beams interfere producing a periodic UV intensity pattern. The fiber is subjected to the interference pattern by placing it immediately behind the phase mask. Before exposure, the fiber jacket is chemically or mechanically removed near the point where the grating is to be written and the areas of the germanium doped core material subjected to the constructive interference regions undergo a permanent change in refractive index. The magnitude of the refractive index change is related to the UV source intensity, wavelength, total exposure time and the material composition of the fiber. Refractive index changes ranging between $10^{-5} - 10^{-3}$ can be routinely

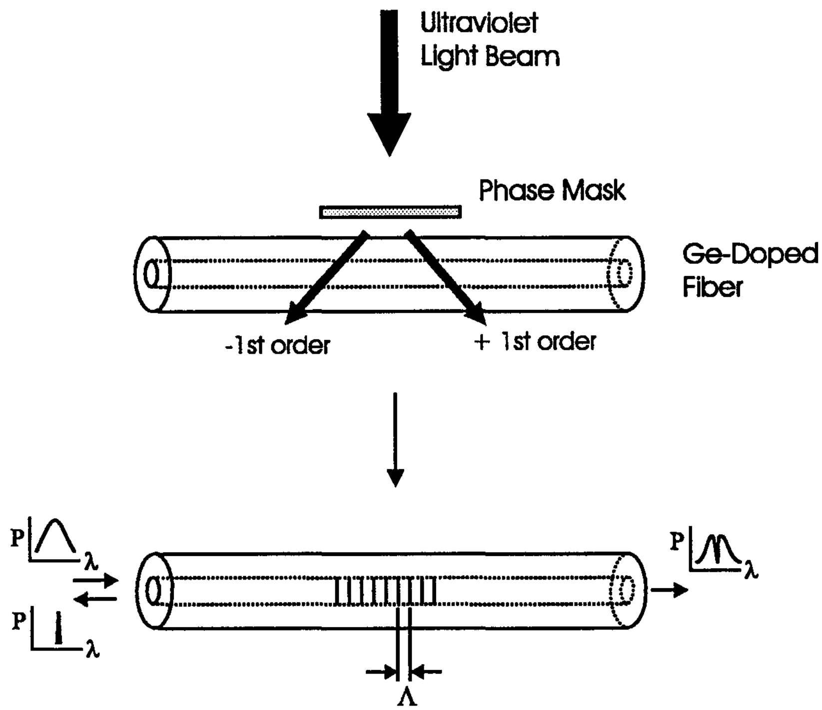

Figure 6.1: A fiber Bragg grating written within the core of a single mode optical fiber using a common phase mask technique.

obtained in germanium doped silica fibers. By using specialized techniques to increase the fiber's photo-sensitivity such as "hydrogen loading," an index change of 10^{-2} can be achieved [10].

The periodic index perturbation inscribed within the fiber acts as a stop-band filter which reflects a narrow band of the incident optical field. The peak reflection occurs at the Bragg wavelength given by:

$$\lambda_B = 2n_{eff}\Lambda \tag{6.1}$$

where Λ is the period of the grating and n_{eff} is the effective modal index of the fiber. The strength of the photo-induced index changes and the length of the grating are important in determining the total reflectivity and bandwidth. For gratings consisting of a uniform index modulation written along their length, higher order maxima of significant magnitude occur on both sides of the main reflection peak. This is undesirable for many applications such as WDM, as the effective reflection bandwidth is large and nonuniform. To overcome this problem, apodization techniques are commonly used [10]. An apodized fiber grating consists of a slowly varying envelope function (usually of Gaussian or raised-cosine character) which governs the magnitude of the refractive index profile. Using this method, the higher order reflections can be suppressed by typically -20 to -40 dB below the main Bragg resonance peak.

6.3 Fiber Bragg Grating Sensors

Most of the work involved with fiber Bragg grating sensors has been focussed towards the area of strain sensing. If strain is applied to the grating portion of the fiber, the Bragg wavelength will shift. When the grating section of a sensing fiber is bonded to a mechanical structure, the strain in that structure can be measured by precise monitoring of the center wavelength of the grating reflection. The strain response results from two main effects; the strain-induced change in the grating period due to physical elongation of the fiber, and the change in the waveguide's effective index due to photoelastic effects. The shift of the Bragg wavelength for a homogeneous, isotropic strain can be expressed as [9]:

$$\frac{1}{\lambda_B}\frac{\delta\lambda_B}{\delta\varepsilon} \approx 0.78 \times 10^{-6} \mu\varepsilon^{-1} \tag{6.2}$$

for common single mode silica fibers. ε is the applied strain, usually expressed in units of microstrain ($\mu\varepsilon$), which represents an induced length change of 1 part in 10^6. For a Bragg wavelength of 1550 nm, this equation predicts a wavelength shift of 1.21 pm/$\mu\varepsilon$. This value gives a "rule-of-thumb" estimate of the grating's sensitivity and varies slightly for various fiber types.

The center wavelength of the fiber grating is also sensitive to temperature changes. The thermal response for silica fibers is dominated by the temperature dependence of the refractive index, which accounts for approximately 95% of the total induced wavelength shift. For a constant strain, the thermal sensitivity is given as [9]:

$$\frac{1}{\lambda_B}\frac{\delta\lambda_B}{\delta T} \approx 6.67 \times 10^{-6} \quad {}^{\circ}C^{-1} \tag{6.3}$$

In terms of wavelength, this corresponds to a shift of ~ 10 pm/ °C at 1550 nm. The sensitivity to both temperature and strain poses a problem for fiber Bragg grating sensors as temperature variations throughout a structure can lead to anomalous strain readings. Thus, extensive work has been performed to establish techniques capable of demodulating the strain and temperature induced effects. One of the more common approaches involves the use of two separate fiber cables containing gratings. Both gratings are placed in thermal contact with a structure, while only one of them is fixed to it and affected by strain changes. In this way, the temperature induced wavelength shifts can be separately monitored and subtracted from the measured wavelength shift of the grating bonded to the structure. An apparent disadvantage of this method is that two separate fiber paths are required, adding to the overall cost and complexity of the system.

A critical component for fiber Bragg grating sensors is a wavelength sensitive element, which is capable of tracking the small strain and temperature induced wavelength shifts. Typical sensor applications require a resolution of a few $\mu\varepsilon$ over a range of a few thousand $\mu\varepsilon$. To accomplish this, a wavelength monitor must provide a wavelength sensitivity of a few picometers over a range of a few nanometers. Optical spectrum analyzers and relatively complex wavelength meters have been used for this purpose, but they dominate the overall cost of the system and cannot generally be used for dynamic measurement. Wavelength detection schemes based on fiber interferometers [14], fiber Fabry-Perot filters [19] and bulk optic filters [17] are just a few of the recently reported "low cost" solutions. In general, the fiber-based techniques tend to suffer from high temperature dependence, while methods that use bulk components such as spectral filters, are comprised of multiple elements adding to the overall size and cost of the approach. The lack of compact, reliable and low cost devices capable of providing high resolution wavelength discrimination has been a major factor in impeding the progress of this technology.

The general configuration of a fiber Bragg grating strain sensor is illustrated in Fig. 6.2. A broadband optical source is used to illuminate the fiber grating, which is fixed to a chosen structure. The source should be spectrally broad enough to cover the entire strain induced tuning range of the grating (typically a few nm), but should

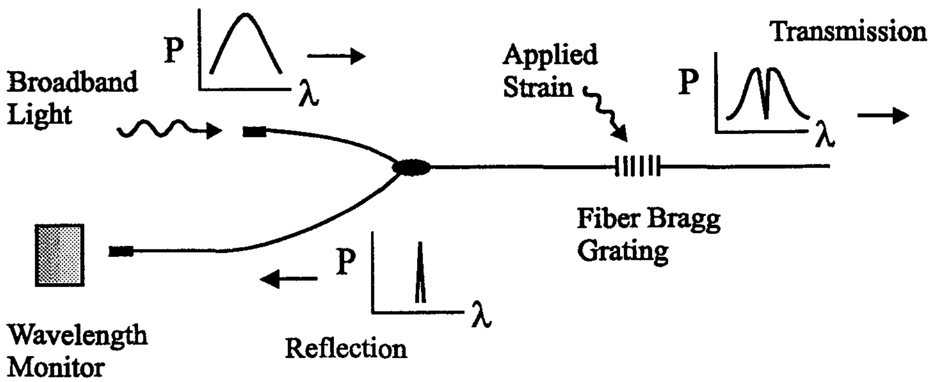

Figure 6.2: Basic fiber Bragg grating-based sensor.

not be too broad, to limit the amount of "wasted" optical power being transmitted through the grating. The reflected signal wavelength is then monitored and converted to a strain reading.

There are several choices for a broadband source including: light emitting diodes (LED's), superluminescent diodes (SLD's) and optically pumped, doped fibers. LED's and SLD's offer the advantage of low cost as they require only a single semiconductor device, whereas fiber sources require multiple components including: an optical pump source, a WDM coupler, filters and isolators. LED's are typically very broadband, having an optical bandwidth of hundreds of nanometers. The grating reflects only a narrow band out of the incident light, so the total power reflected is low. The power spectral density of a SLD is significantly higher as its output is much narrower in wavelength, being on the order of 10's of nanometers. Therefore, SLD's are ideal candidates for sensing applications. However, high performance 1.55 μm superluminescent diodes are not widely commercially available at this time.

Erbium (Er) doped fiber sources have become a popular choice for sensing applications near 1550 nm due to their maturity and commercial availability. The demand for Er-doped fiber amplifiers (EDFA's) for telecom applications has been the main driving force behind this technology, and the cost of components comprising these systems has dropped significantly over the past few years. Two popular pump wavelengths are used with these fibers: 980 nm and 1480 nm, which are now readily

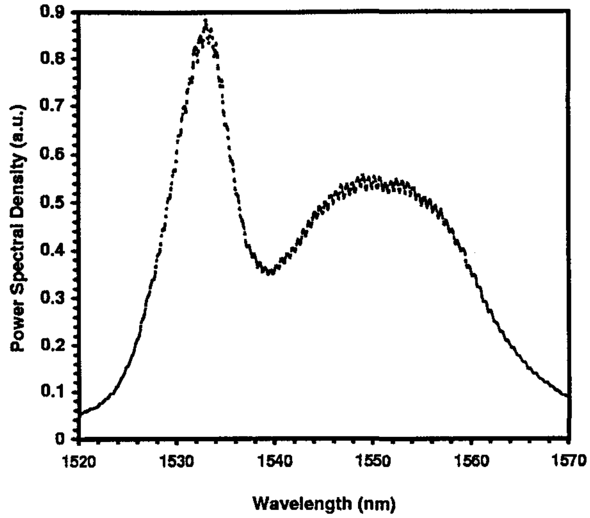

Figure 6.3: Amplified spontaneous emission spectrum of an optically pumped Er-doped fiber source.

available as high power laser diodes. When optically pumped, the Er-doped fiber can produce a stable amplified spontaneous emission (ASE) output over an approximately 35 nm wavelength band, as shown in Fig. 6.3.

6.4 Strain Sensor Demonstration

In this section, various types of fiber Bragg grating strain sensors are demonstrated which utilize the wavelength monitors as key measuring elements. Schemes are presented which involve a broadband source, a tunable fiber laser and a multiplexed sensor system containing four FBGs of varying center wavelength. The operation, characteristics and performance of each of the designs are discussed.

6.4.1 Broadband Sensor

The first sensor examined is similar to the design proposed in Fig. 6.2. It makes use of a superfluorescent Er-doped fiber source set in a backward-pumped configuration (see Fig. 6.4). In this arrangement, the amplified spontaneous emission generated in the fiber is taken in a direction opposite to that of the pump laser radiation.

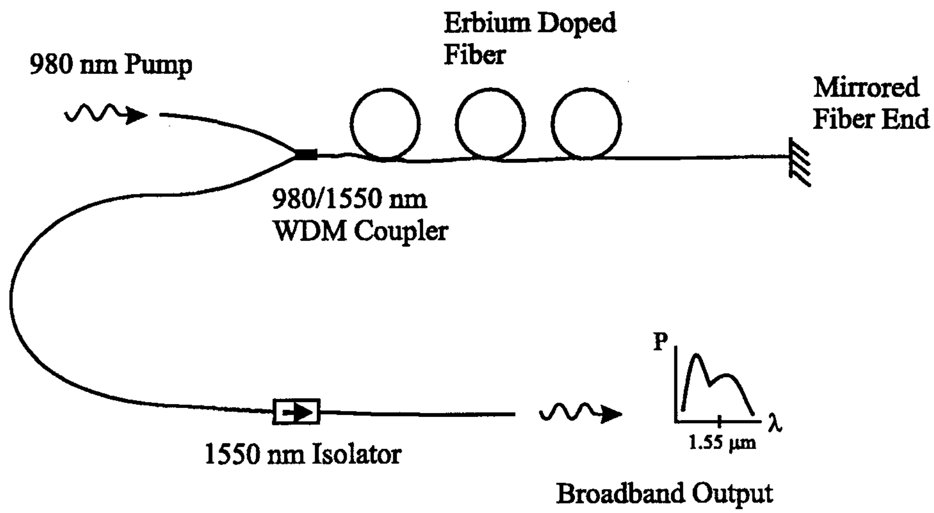

Figure 6.4: Backward pumped Er-doped fiber source used for strain sensor.

This design has been shown to provide superior output characteristics compared to those of forward pumped schemes, in which the ASE is taken in the direction of the pump signal [73]. Both configurations were attempted and it was observed that the backward pumped source exhibited a higher degree of power stability and could provide approximately double the maximum output power. Therefore, this geometry was chosen for the final sensor application.

The fiber source was constructed from a 100 mW fiber-coupled 980 nm diode pump laser purchased from Nortel Networks, a 1550 nm fiber isolator, a 980/1550 nm WDM coupler, a fiber patch cord with an aluminum coated end and a 1.5 m, high concentration (5000 ppm) single-mode Er-doped fiber. The absorption coefficient of the fiber was large, being specified at 23 dB/m at 980 nm, allowing a 1.5 m length to effectively absorb all of the pump signal. The 980 nm light was efficiently coupled into the Er-doped fiber using a 980/1550 nm fiber WDM coupler. A 1550 nm fiber isolator, quoted with a -46 dB isolation, was added to the design to reduce optical feedback from the unterminated fiber end to prevent lasing from occurring within the system. A fiber patch cord with an aluminum coated end was placed behind the Er-doped fiber to reflect the forward travelling ASE signal, which allowed the overall output power of the source to be increased. Typically, the Er-doped fiber

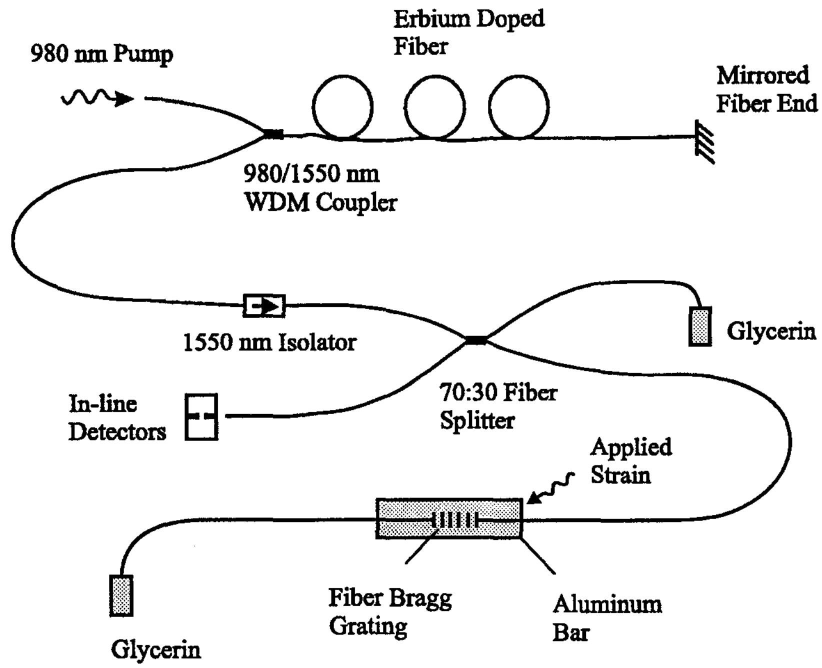

Figure 6.5: Strain sensor configuration using a superfluorescent Er-doped fiber source.

end is immersed in an index matching fluid such as glycerin, to reduce reflections that may induce lasing, in such designs. However, it was found that the optical isolator provided sufficient protection to prevent this problem from occurring. The maximum output power of the source was increased by a factor of approximately 1.4 with the aluminum coated fiber in place. Index matching gel was used with all fiber connections to reduce reflections at the fiber interfaces.

It was observed that the 980 nm pump laser was more stable when operated at power levels below 60 mW. With 60 mW of pump power, the broadband source produced a total ASE output power of 0.84 mW, which is relatively low compared to that of other reported high power Er-doped sources [73], [74]. This can be attributed in part, to the reduced conversion efficiency of the fiber due to the very high Erbium concentration [75]. Nevertheless, the performance of the source was sufficient for the proposed demonstration. The spectral output of the fiber is shown in Fig. 6.3.

The broadband sensor design is illustrated in Fig. 6.5. A 1 cm long fiber Bragg grating written within a SMF fiber cable was used as the sensing element. The

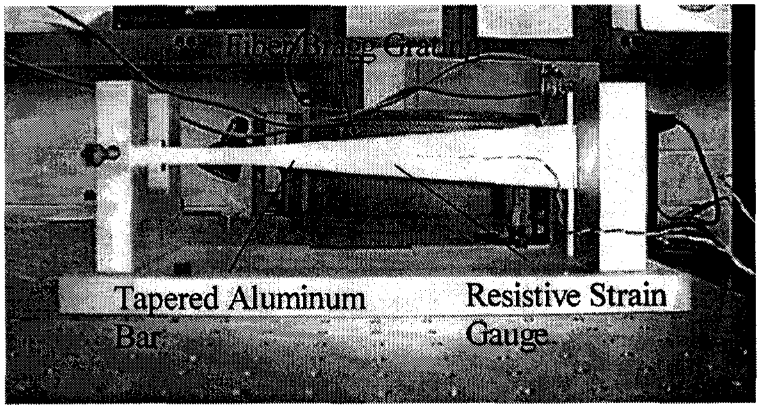

Figure 6.6: Tapered aluminum beam in which strain is monitored. A conventional resistive strain gauge is located on its front face for calibration purposes. Directly on the opposite side of the bar a fiber Bragg grating is bonded.

grating had a center wavelength of 1548.8 nm, a peak reflectivity of 98% and a 0.30 nm reflection bandwidth. It was illuminated with the Er-doped fiber source and the reflected signal was monitored using a single set of in-line waveguide photodetectors. The grating portion of the sensing fiber was attached to a cantilevered aluminum beam using a high quality epoxy (EPO-TEK 353ND) purchased from Epoxy Technology, which was specially designed for use with optical fibers. The aluminum beam was tapered to allow a uniform strain to be created along its length when a force is applied to its end, as shown Fig. 6.6. The beam was clamped at its base and force was applied to its free end using two adjustable bolts, which permitted positive and negative strains to be applied. A conventional resistive strain gauge, purchased from Omega Engineering Inc., was bonded to the other side of the beam directly opposite to the grating for calibration purposes.

When strain is applied to the cantilevered beam the reflection peak of the Bragg grating will shift, as shown in Fig. 6.7. A positive strain indicates a tensile force on the grating causing the Bragg wavelength to shift to a longer wavelength, whereas a negative strain denotes a compressive force on the fiber, shifting the peak to a shorter wavelength. The grating reflection is observed to tune linearly with strain and no "chirping" (spectral broadening) effects can be seen. The grating's center wavelength

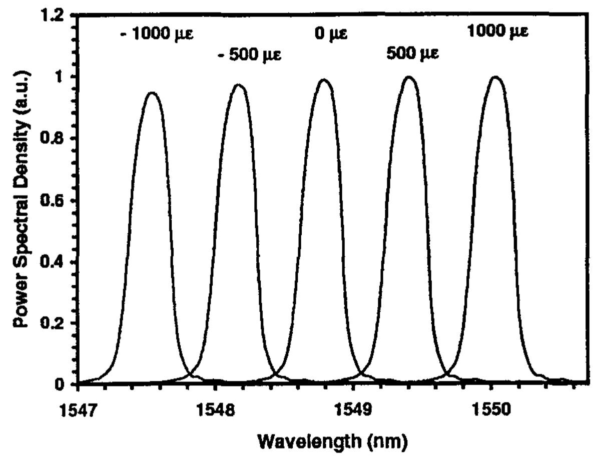

Figure 6.7: The reflection of a fiber Bragg grating subjected to various strains.

as a function of strain is illustrated in Fig. 6.8. A least squares fit to the data was performed having a slope of 1.241 $\pm$ 0.001 pm/$\mu\varepsilon$ with a correlation coefficient of R = 0.99996. The measured strain sensitivity is within 2.5% of the value predicted by Eq. 6.2, and the large value of the correlation coefficient R (being close to one) implies that the Bragg wavelength behaves very linearly with strain over the examined range.

It is important to minimize any background reflections in the system as they will influence the strain reading by inducing undesired photocurrents in the wavelength monitors. Since the background light level is broadband ($\sim$ 35 nm), even a low to moderate reflected power will significantly mask the signal from the narrowband FBG. To reduce this effect, the unterminated fiber ends were immersed in glycerin and index matching fluid was used between all fiber connections, which lowered the background level to -29.5 $\pm$ 0.2 dB relative to the grating's peak reflected power at 1548.8 nm.

A single set of 500 μm long in-line detector segments was used to monitor the reflection from the grating. The photocurrent ratio becomes a direct measure of the strain in the aluminum beam, assuming that the strain is fully transferred to the FBG. This is a valid assumption if a suitable epoxy is used. Fig. 6.9 displays the photocurrent ratio taken from the in-line detectors as a function of the applied strain. The strain is determined from an electrical foil gauge bonded to the opposite side of

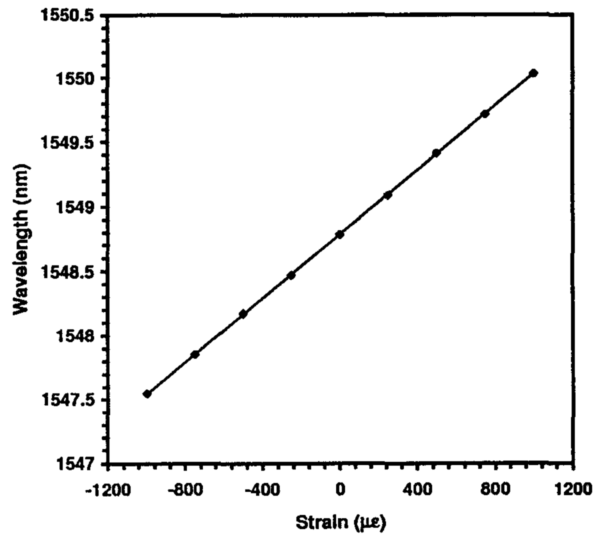

Figure 6.8: The reflected center wavelength of a fiber Bragg grating as a function of the applied strain.

the beam. It is seen that the wavelength monitor output exhibits a linear dependence on strain over a $\pm$ 1100 $\mu\varepsilon$ range. A least squares fit to the data was performed, having a slope of $2.964 \times 10^{-3} \pm 0.004 \times 10^{-3}$ %/$\mu\varepsilon$, with a correlation coefficient of R = 0.9997.

By recording the rms noise level taken from the divider circuit output, a mean strain sensitivity of 3.4 $\mu\varepsilon$ was determined, over a 2200 $\mu\varepsilon$ range. This result was obtained with an average measured reflected power of less than 0.5 μW reaching the in-line detectors. The photocurrent divider circuit, described in section 5.2.1, was used for the measurement with a 0.2 second electrical averaging time. The observed strain sensitivity is high, despite the fact that only a small portion of the total operating range of the wavelength monitor is used. As will be seen in section 6.4.4, this property is exploited in the design of a multiplexed sensor network. The obtained performance of the sensor is comparable to other more complex reported systems, and is suitable for most common precision sensing applications. However, if an increased sensitivity is required, a higher power broadband optical source can be used, or the electrical averaging time for the measurement can be increased.

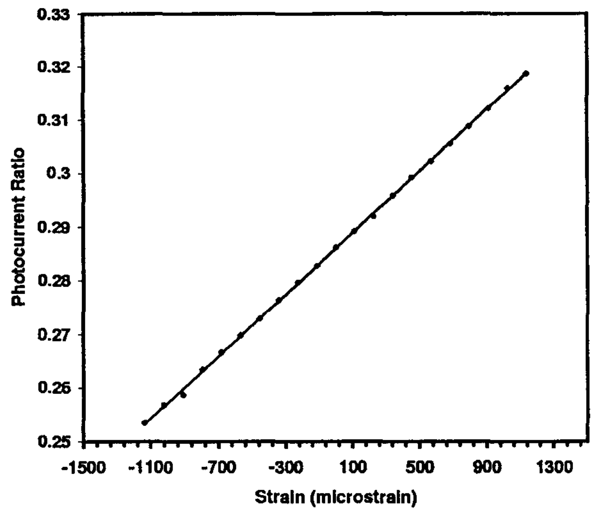

Figure 6.9: The broadband sensor results.

6.4.2 Laser Sensor

An alternative sensor design involves the use of a tunable fiber laser whose lasing wavelength is taken as a measure of strain. Such a system has been demonstrated in [17], where two discrete photodetectors and a bulk-optic spectral filter were utilized to perform the wavelength monitoring function. In this section a similar design is presented in which the in-line waveguide photodetectors are utilized to track the induced wavelength shifts.

The laser sensor was constructed using components similar to those of the broadband sensor with a slight change in configuration. Standard laser sources employ a gain medium, two reflecting surfaces and some form of electrical or optical pumping. For the current laser system, the Er-doped fiber provides the gain medium which is optically pumped by the 980 nm laser diode. The FBG and aluminum coated fiber end compose the mirrors of the cavity and the total cavity length was measured to be 2.11 $\pm$ 0.02 m. The sensor layout is shown in Fig. 6.10.

The 980 nm pump signal is coupled into a 1550 nm single mode fiber using the 980/1550 nm WDM coupler. The pump light then passes through the FBG which is fixed to the cantilevered beam, and reaches the Er-doped fiber where it is absorbed.

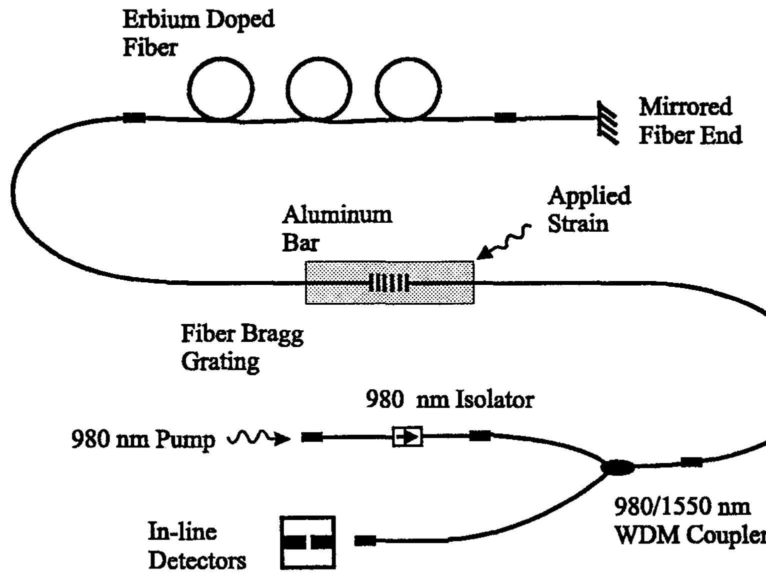

Figure 6.10: Laser sensor design.

The aluminum coated fiber end functions as a broadband mirror, reflecting the forward travelling light in a direction back through the cavity. The FBG acts as a wavelength selective mirror which reflects a narrow band of wavelengths. With sufficient pump power, the system will begin to lase near the peak of the Bragg grating reflection, as this is the wavelength of maximum optical feedback. If strain is applied to the aluminum beam, the grating's reflection spectrum will shift, thereby tuning the system's lasing wavelength. In this way, a tunable fiber laser is created whose wavelength can be utilized as a signature of strain.

The threshold pump power required to induce lasing in the fiber cavity, is highly dependent on the losses in the system. Therefore, significant care was taken to minimize the losses at all fiber connections by thoroughly cleaning the fiber ends and connectors, careful alignment, and by using index matching gel. When optimized, the threshold pump power of the system was measured to be 14 $\pm$ 3 mW. The fiber laser output was found to be heavily multi-mode, as the resonant cavity can theoretically support over 790 modes within the spectral range of grating's FWHM. Near threshold, the laser output was very unstable containing significant mode partition

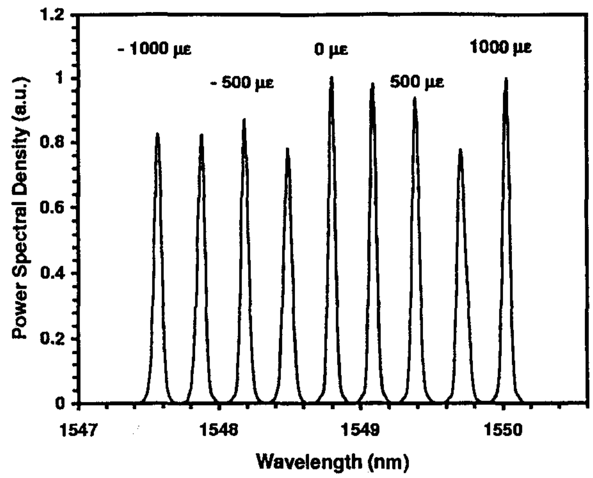

Figure 6.11: Laser Wavelength as a function of strain.

noise and large output power fluctuations, but at higher pump powers the laser stability appeared to improve.

The tuning characteristics of the laser system were examined as force was applied to the aluminum bar. The fiber output spectrum for several values of strain at a constant optical pump power of 36 mW, is shown in Fig. 6.11. The wavelength is observed to tune at a rate of 1.23 ± 0.01 pm/$\mu\varepsilon$, similar to that measured in Fig. 6.8. Comparing Figs. 6.7 and 6.11, it is evident that the laser spectrum is substantially narrower in wavelength than the signal obtained using broadband illumination. The apparent laser linewidth of 0.07 nm in Fig. 6.11 corresponds to the resolution limit of the optical spectrum analyzer used to record the output.

The output power generated by the laser system was observed to be much larger than that of the reflected ASE signal produced by the broadband sensor. For a pump power of 36 mW, the fiber laser output was measured to be approximately 0.32 mW, which is over 600 times greater than that of the maximum obtained power using broadband illumination. Above 25 mW of pump signal power, the slope efficiency of the fiber laser, defined as the slope of the laser output power as a function of the fiber-coupled pump power, was measured to be 1.41 ± 0.06 %.

Using a set of 250 μm long in-line detector segments, the laser wavelength was

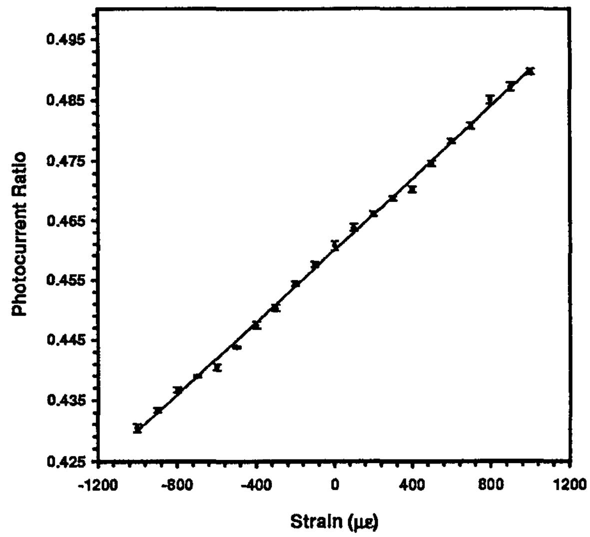

Figure 6.12: Laser strain sensor results.

monitored as strain was applied to the cantilevered beam. The wavelength monitor output is shown in Fig. 6.12 as a function of strain recorded by the electrical gauge. A least squares fit to the data yields a slope of 2.97×10^{-3} %/$\mu\varepsilon$ and a correlation coefficient of R = 0.998. A mean strain sensitivity of 19 $\mu\varepsilon$ over a 2000 $\mu\varepsilon$ range was demonstrated using 36 mW of optical pump power. An average laser power of 0.28 mW was measured at the tapered fiber output used to couple the signal into the in-line detectors.

The narrower linewidth and increased output power of the laser sensor are beneficial for fiber Bragg strain sensing, as they both facilitate higher precision wavelength determination. However, it is evident that the laser sensor performance is inferior to than that of the broadband sensor. This can be attributed to the undesirable characteristics of the system such as multi-mode behavior, large mode partition noise and output power instability. These problems are generally inherent to fiber laser sources and can therefore not easily be solved. However, small improvements may be gained through the use of a stabilized pump laser and a thermally insulated fiber jacket.

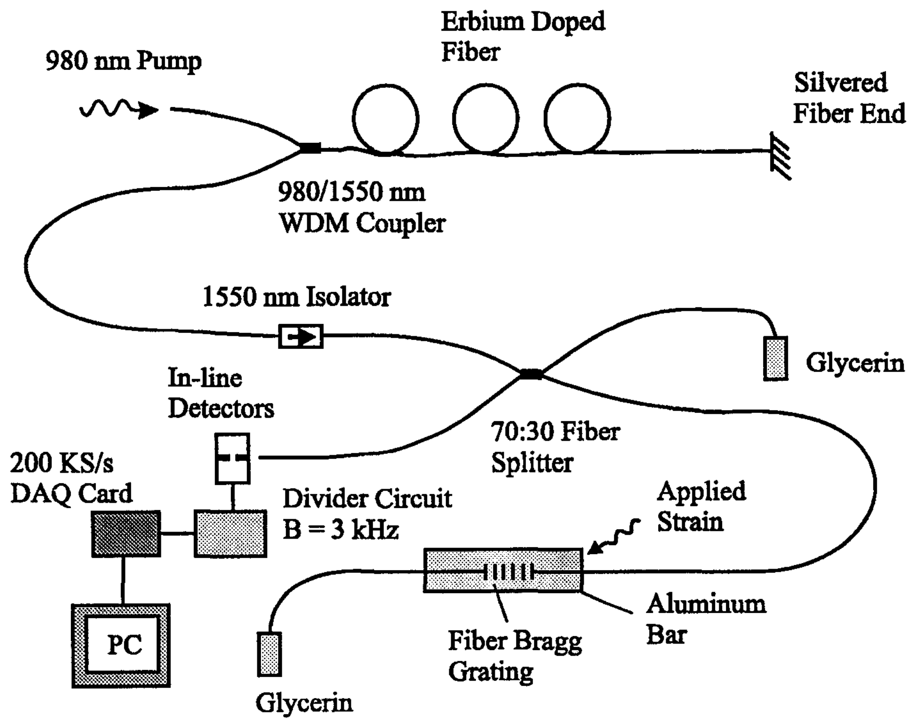

Figure 6.13: Set-up used for the dynamic strain measurement.

6.4.3 Dynamic Measurements

The monitoring of "static", or slowly varying strains, is important for applications concerned with the long term stability of a structure. For applications in which the dynamic response of an object or its vibrational properties are of interest, a monitoring system capable of tracking rapid strain variations is required. Wavelength meters requiring wavelength scanning functions or moving parts such as optical spectrum analyzers, monochromators and tunable filter-based methods are typically very slow and cannot be used to track signal oscillations at frequencies greater than a few Hz. Therefore, alternative wavelength monitoring techniques are required for these applications.

A sensor design similar to that of Fig. 6.5 was constructed to examine the performance of the wavelength monitors for dynamic strain sensing. The set-up is illustrated in Fig. 6.13. A 1548.8 nm FBG mounted on a tapered aluminum cantilever was illuminated with a backward-pumped Er-doped fiber broadband source. On the opposite side of the beam an electrical strain gauge was mounted for comparison purposes. The grating reflection was coupled into a single set of 250 μm long in-line waveguide photodiodes. To track the rapidly varying center wavelength of the grating reflection, a photocurrent divider circuit similar to that of Fig. A.1, was constructed having a -3 dB electrical bandwidth of 3 kHz. The frequency response of the HP multimeters used above, to record the wavelength monitor output, was not sufficient for the proposed application. Therefore, a high speed data acquisition (DAQ) card, purchased from National Instruments Inc., was used to sample the divider circuit output. The DAQ card had a maximum sampling rate of 200 kS/s and contained 16 separate input channels (8 with independent grounds). The sampled data from the DAQ card was then stored on a PC, with one of the input channels configured to record the photocurrent divider circuit output, while another was set to monitor the analog output voltage of the electrical strain gauge controller.

A rubber mallet was used to provide a step input excitation to the aluminum bar containing the fiber Bragg grating. The outputs of the electrical and optical strain gauges were monitored as a function of time and are shown in Fig. 6.14. The top image displays the calibrated output of the electrical foil strain gauge. For this data, it is seen that a peak-to-peak strain amplitude of 330 $\mu\varepsilon$ was induced by the rubber mallet and that the aluminum beam had a resonant frequency of 196 $\pm$ 2 Hz. The bottom figure displays the time dependence of the wavelength monitor output and clearly shows that the optical sensor is capable of tracking the induced vibration at this frequency. A strain sensitivity of 16 $\mu\varepsilon$ was demonstrated using the higher bandwidth divider circuit.

The main sources of noise present in the system were found to result from thermal noise in the detector circuit electronics and from electro-magnetic pick-up. The divider circuit was originally constructed on an electrical breadboard. To minimize the electromagnetic interference, the circuit components were transferred and soldered onto a planarized vector board, while attempting to minimize the wire lead lengths. The vector board was then placed in a shielded aluminum box with coaxial cable input and output connectors installed. It was found that the noise level was significantly

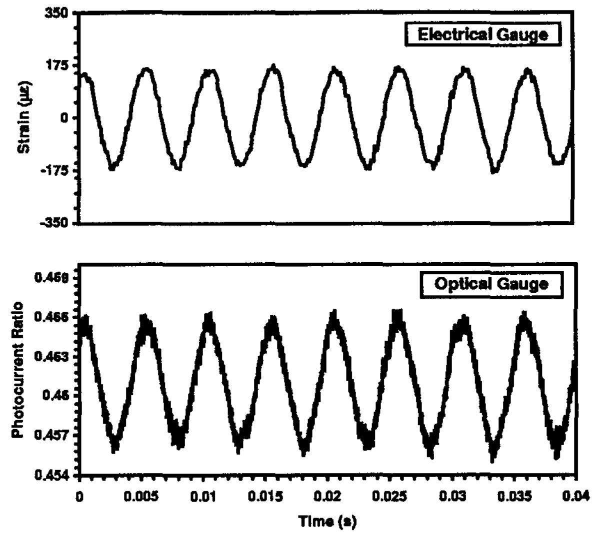

Figure 6.14: Dynamic strain sensor performance as monitored by: (top) a resistive foil electrical strain gauge; and (bottom) the FBG sensor utilizing the in-line waveguide detectors. A shielded electronic divider circuit was used for the measurement.

reduced when using the shielded circuit.

Alternative methods which may be followed to improve the performance of the optical sensor include the use of a higher power broadband optical source, and/or a lowpass or bandpass electrical filter to limit the electrical bandwidth of the system. However, the increase in sensitivity using the latter method is gained at the price of a decreased frequency operating range.

Fig. 6.14 also demonstrates the high performance operation of the electrical gauges. These devices are relatively inexpensive and can provide high sensitivity over a large range of strain values (over a few thousand $\mu\varepsilon$), but they do not offer the previously stated advantages inherent to fiber-based sensors.

6.4.4 Multi-Point Sensing

One of the important benefits offered by fiber Bragg grating sensors is their natural ability to be multiplexed along a single fiber path. The multiplexing issue is critical for applications that require a sensing capability at several different locations within a structure. Multiplexing schemes based on time division multiplexing (TDM) [76] and wavelength division multiplexing [11], have been successfully demonstrated. TDM systems are relatively complicated, requiring a pulsed source, precise fiber lengths between sensing elements and high speed detection and switching electronics. Systems based on WDM have become popular due to the rapid advancement and the increased commercial availability of high quality demultiplexing components.

In this section, a multi-point sensor system utilizing four multiplexed FBGs and a WDM component is demonstrated. An array of wavelength monitoring photodiodes is shown to be an effective means of simultaneously tracking the center wavelengths of multiple gratings subjected to strain. The characteristics and performance of the sensor network are described.

The four-point fiber optic strain sensor illustrated in Fig. 6.15, was constructed for the demonstration. It utilizes four FBGs of varying center wavelengths written in series along a single optical fiber (purchased from QPS Technologies Inc). The four grating portions of the sensing fiber were epoxied to individual, tapered aluminum beams, as shown in Fig. 6.16. Conventional electrical strain gauges were bonded to the opposite sides of the aluminum bars for calibration purposes.

A broadband illumination scheme was chosen for this application over that of a laser design for two main considerations: firstly, as demonstrated above, the broadband sensor displayed superior performance over that of the laser configuration; and secondly, the Er-doped fiber is a homogeneously-broadened gain medium, making it difficult for several lasing wavelengths to stably coexist within the cavity. However, specialized techniques have been demonstrated to accomplish multi-wavelength laser operation in these fibers (for example see [77]). Nevertheless, these schemes are usually complicated and less practical compared to that of broadband sensor designs.

The backward pumped Er-doped fiber source illustrated in Fig. 6.4, was selected as a broadband optical source. The ASE generated by the Er-doped fiber was used to illuminate the fiber gratings of unstrained center wavelengths 1535.7, 1542.5, 1548.7 and 1554.4 nm. All unterminated fiber ends in the system were submerged in glycerin to suppress back-reflections. The light reflected by the gratings passed through the 70:30 fiber splitter and entered the broadband wavelength demultiplexer, purchased from JDS-Uniphase. The demultiplexer contained four 5-nm wide channels, centered

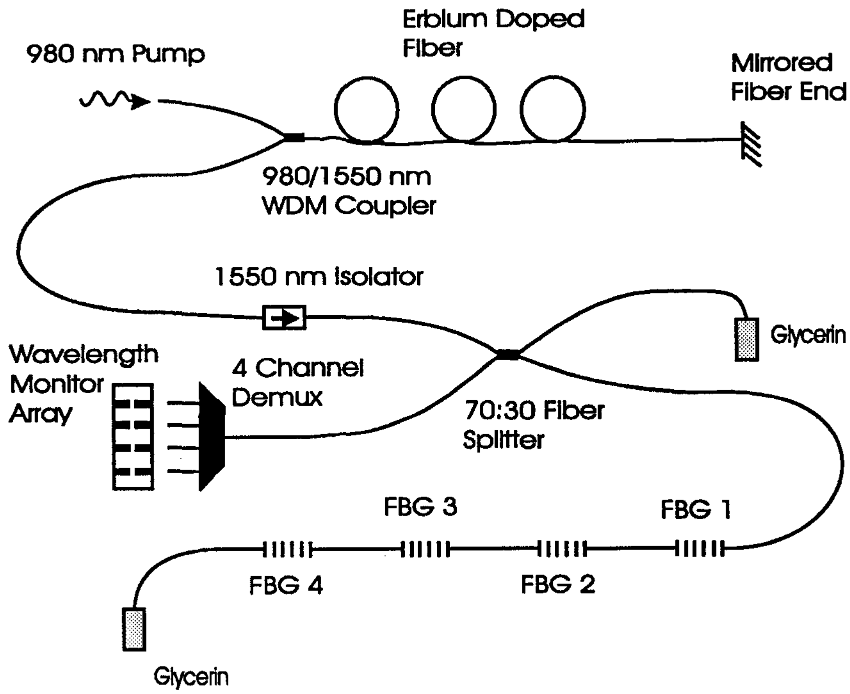

Figure 6.15: Set-up used for the demonstration of a four-point multiplexed Bragg grating sensor.

at wavelengths 1538, 1545, 1551 and 1557 nm, with the insertion loss at the center of the passbands being less than 0.5 dB. The demultiplexer separated the reflected grating signals and sent them to an array of in-line detectors. When strain was applied to the corresponding aluminum beams, the gratings were wavelength tuned within their respective WDM channel bands. It was therefore important that the wavelength demultiplexer contained channels spectrally broad enough to contain the grating reflection over its entire strain induced tuning range. It was also critical that the center wavelengths of the gratings were spaced sufficiently far apart to maintain low crosstalk between reflected signals. For a typical operating range of $\pm$ 1000 $\mu\varepsilon$, Eq. 6.2 predicts a wavelength shift of 2.4 nm. Using an Er-doped fiber source producing a useable ASE signal over a $\sim$35 nm wavelength range, a maximum of 14 gratings can be multiplexed in this fashion. Since the proposed wavelength monitoring system can operate over the entire wavelength range of the Er-doped fiber gain spectrum, it is an ideal candidate for this application. The spectral properties of the components

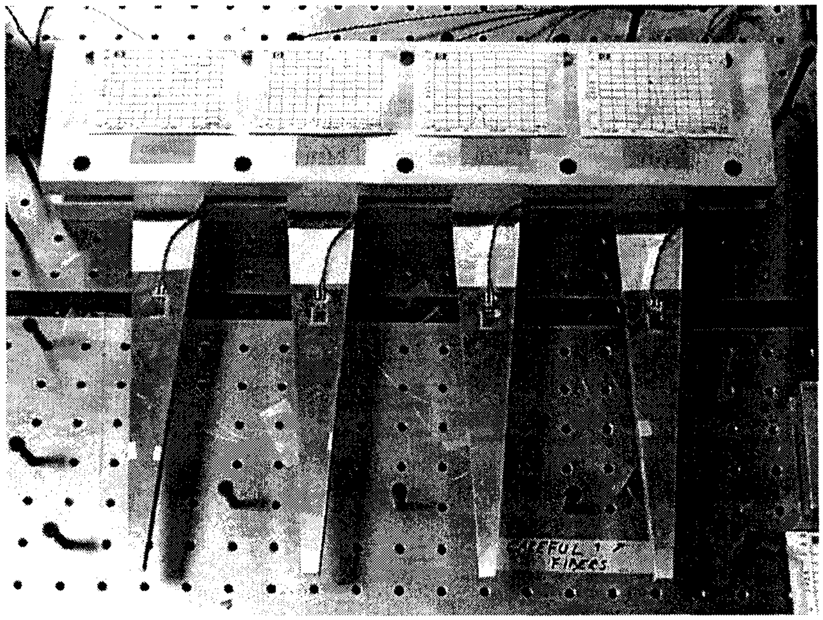

Figure 6.16: Aluminum bars used in the multiplexed sensor with fiber and electrical strain gauges attached.

utilized in the sensor design are shown in Fig. 6.17.

The grating center wavelengths were selected to lie within the center of the demultiplexer channels, such that positive and negative strain shifts could be monitored. Unfortunately, due to the contraction of the epoxy upon curing (used to bond the FBGs to the aluminum bars), the grating wavelengths were shifted to the short wavelength side of the demultiplexer's channel bands. Nevertheless, positively induced wavelength shifts due to tensile strains could still be effectively examined.

The wavelength tuning characteristics of the four FBGs were characterized as a function of the applied strain. The reflection spectrum of the 1554.4 nm FBG subjected to varying amounts of tensile force is shown in Fig. 6.18. Similar to the single sensor case, it is seen that the grating's reflection spectrum shifts linearly with strain with no significant chirping effects. The other gratings tuned in a similar manner, and an average wavelength shift of 1.171 $\pm$ 0.001 pm/$\mu\varepsilon$ was observed.

To track the grating wavelengths, an array of wavelength monitors was used which contained various lengths of detector segments (see Fig. 5.14). In-line detector pairs

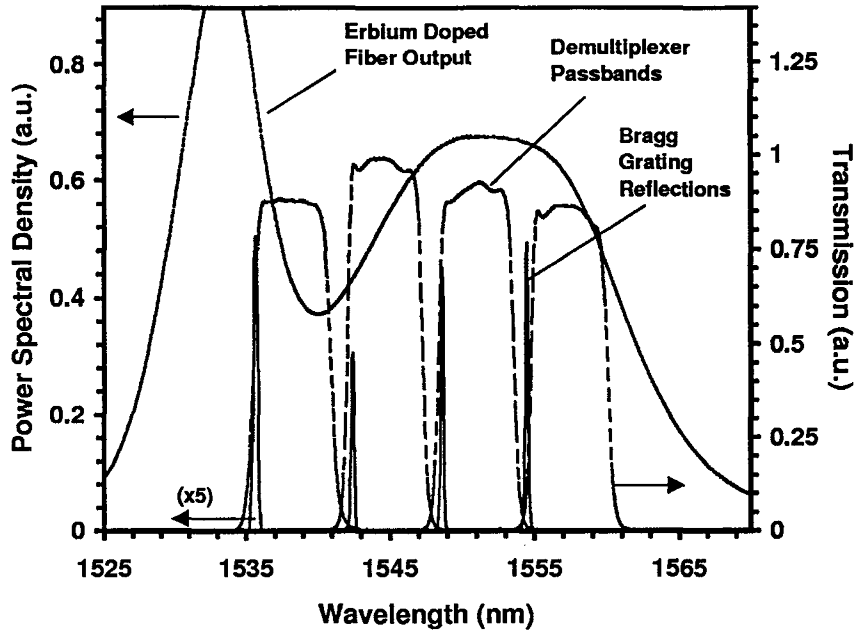

Figure 6.17: The components used in the construction of the multiplexed sensor network. The reflected grating spectra are for the case of zero applied strain to all aluminum bars.

of waveguide lengths 293, 445, 596 and 750 μm were used to monitor fiber gratings of center wavelengths 1535.7, 1542.5, 1548.7 and 1554.4 nm, respectively. The various dimensions were selected to demonstrate the length tuning technique described in section 5.2.4, to optimize and extend the detector's operating range. The individual grating signals were separated by the demultiplexer and a four-element tapered fiber array was used to deliver light to the detectors. The in-line waveguide pairs were spaced 250 μm apart and the total chip size was approximately 1.5 $\times$ 1.5 mm. The measured crosstalk between detectors was found to be -22.0 $\pm$ 0.5 dB, which is dominated by optical scattering from adjacent elements. This value can be lowered by improved optical coupling to the device.

The performance of the sensor is shown in Fig. 6.19, with all sets of detectors held under zero voltage bias. The output of the array behaves very linearly with strain with an average correlation coefficient of R = 0.9987, obtained from a least squares fit. An average strain sensitivity of 6 $\mu\varepsilon$ (corresponding to a wavelength sensitivity of

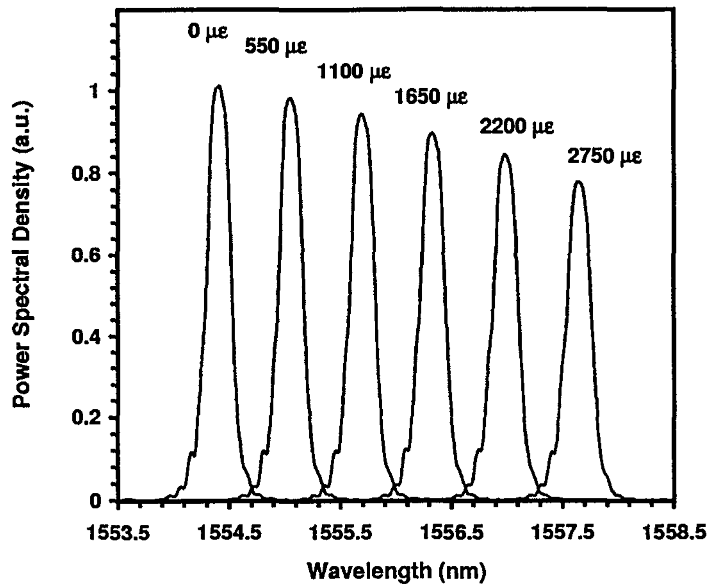

Figure 6.18: Reflection of a 1554.4 nm Bragg grating for various applied tensile strains.

7 pm) was achieved with a back reflected power of approximately 0.3 μW per grating reaching the detector array.

The use of the in-line detectors in the multiplexed sensor scheme offers many advantages over that of more common wavelength monitoring techniques, such as the use of optical spectrum analyzers and interferometric-based methods. In addition to requiring no moving parts, having a compact size and offering a potentially lower cost, the in-line detector array allows grating signals to be monitored simultaneously. This is an important property for the monitoring of strains that vary rapidly with time.

If temperature compensation is required, the active locking technique described in section 5.2.3, can be utilized with a temperature stabilized FBG to provide the reference wavelength. Such stabilized gratings are now commercially available at standard telecommunication wavelengths.

The sensor demonstration is very similar to the application of wavelength channel monitoring in WDM systems. For this application, it is important to monitor the system wavelengths to insure that they stay near the center of their designated

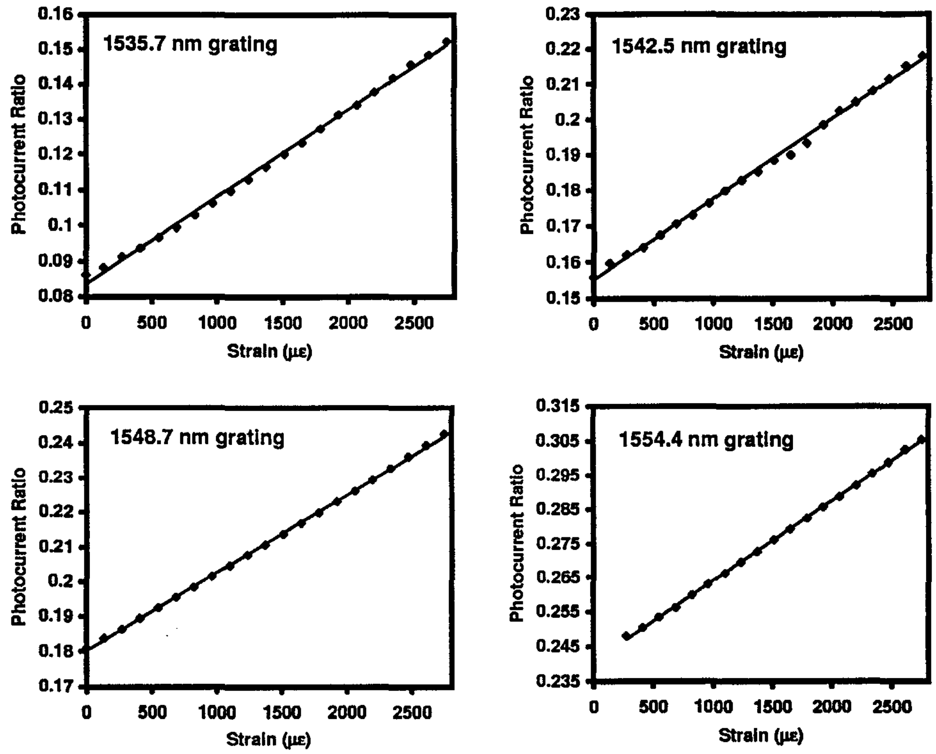

Figure 6.19: The performance of the multi-point sensor network.

wavelength bands. Due to temperature variations and aging of laser transmitters in a system, the channel wavelengths are observed to drift over time. Typically, a wavelength shift of 10% of the system channel spacing is permitted, to keep inter-channel crosstalk from becoming significant. Similar to the multiplexed sensor, an array of wavelength monitoring photodiodes placed behind a demultiplexer, may be used to track the positions of the laser wavelengths within their designated channels. The possibility for monolithic integration with III-V based demultiplexers adds to the attractiveness of the technique.

6.5 Summary

In conclusion, various types of fiber Bragg grating strain sensors have been demonstrated using a new technique to provide the critical function of wavelength sensitive detection. They make use of in-line waveguide photodiode pairs to track the small wavelength shifts in the reflection spectrum of an in-fiber Bragg grating that result from the application of strain.

Two main sensor configurations were examined, broadband sensors and laser sensors. Designs that utilized a broadband optical source were found to provide near $\mu\varepsilon$ strain sensitivity over a 2000 $\mu\varepsilon$ operating range, with reflected signal powers below 0.5 μW. In addition, the wavelength monitor output was observed to behave very linearly with strain over the demonstrated range. Laser-based sensors were found to be a less sensitive means for strain sensing. However, they do offer important advantages, which include a significantly greater obtainable output signal power and a narrower spectral linewidth. Both of these properties facilitate higher precision wavelength determination. Unfortunately, the difficulty in stabilizing the laser system's output power and wavelength limits the effectiveness of the technique.

Finally, a wavelength division multiplexed sensor system was presented containing four Bragg gratings of varying center wavelength, a wavelength demultiplexer and an array of in-line waveguide photodetectors. The detector array is used to track the precise wavelength position of the grating signals within their designated demultiplexer channel bands. The technique requires no moving parts or scanning features, and allows all gratings in the system to be simultaneously monitored for static and dynamic strains.

Chapter 7

Conclusions

This thesis has focused on the development of a new, potentially low cost optoelectronic device capable of functioning as a sensitive wavelength monitor. The primary objective of this work was to devise a simple and feasible approach for tracking wavelength shifts in wavelength division multiplexing networks, tunable diode lasers and fiber Bragg grating optical strain sensors. The need for such components has dramatically increased over recent years as optical communication systems become more complex and new sensing technologies emerge.

The wavelength monitor consists of an in-line pair of quantum well waveguide photodiodes fabricated along a common ridge waveguide channel. The ratio of photocurrents generated between two consecutive waveguide segments was taken as a measure of the input wavelength at photon energies near the detector's absorption band edge. High performance operation was exhibited with a wavelength sensitivity of better than 3 pm, achieved for optical input powers as low as 5 μW (averaged over 0.2 s). In addition, the photocurrent ratio exhibited very low optical power dependence. Compressively strained quantum wells were utilized to enhance the energy separation of the TE and TM absorption band edges, allowing the device to only respond to the TE component within the input optical signal. By this means, the detectors were capable of functioning independently of the input signal polarization. By applying a reverse bias to the detectors, the absorption band edge of the quantum wells was shown to tune over a range exceeding 25 nm, via the quantum confined

Stark effect. This allowed the total operating range of the wavelength monitor to extend past 60 nm.

Compared to other reported technologies this method ranks very highly in terms of wavelength sensitivity, operating range and simplicity. The important functions of wavelength filtering, power splitting and photodetection are all performed by a single semiconductor component allowing the device to be extremely compact. This quality is important not only to increase the number of devices that can be fabricated per wafer, but to also increase their flexibility for optoelectronic integration. In addition, only a single-step optical alignment (fiber-to-waveguide) is required. This significantly lowers the assembly costs relative to approaches using multiple hybrid components.

The wavelength monitors were originally intended for single channel operation. For many applications this is a desirable function, while for others the simultaneous monitoring of several wavelengths is necessary. By using an array of in-line detectors and a wavelength demultiplexer, a system capable of monitoring 4 wavelength channels was demonstrated. The simplicity of the device's geometry allows large detector arrays to be fabricated while maintaining a relatively small chip size.

The temperature sensitivity of the method was determined by the thermal dependence of the material's energy band gap. This value was shown to be approximately -0.73 nm/°C. By using an additional set of in-line detectors integrated on the same semiconductor chip, and a fixed reference wavelength, a novel temperature compensation scheme was presented. This scheme utilized the quantum confined Stark effect to electrically induce a wavelength shift in the absorption band edge to counteract any thermally induced shifts.

As a practical demonstration, various types of fiber Bragg grating optical strain sensors were constructed and characterized. The in-line detectors were utilized to track the small wavelength shifts in the reflection spectrum of an in-fiber Bragg grating that resulted from the application of strain. Two main configurations were examined, including a broadband and a laser sensor design. The broadband sensors were found to be superior and provided near $\mu\varepsilon$ strain sensitivity over a 2000 $\mu\varepsilon$ operating range. In addition, the wavelength monitor output was observed to behave very linearly with strain over the demonstrated range. Finally, a four point multiplexed fiber

Bragg grating strain sensor was presented which contained four fiber Bragg gratings of different center wavelengths, a wavelength demultiplexer and an array of in-line waveguide photodetectors. The array of in-line detectors was used to track the precise wavelength positions of the grating signals within their designated demultiplexer channel bands. The approach required no moving parts or scanning features allowing all gratings in the system to be monitored simultaneously for static and dynamic strains.

7.1 Future Work

The results obtained in this work were very encouraging and further research devoted to this project would be beneficial. Some potential areas for future study are suggested in this section.

The material structure of the wavelength monitor was chosen to be similar to that of typical 1.55 μm SCH laser designs. Although the chosen structure provided excellent results, there is still significant room for improvement. Additional studies devoted to optimizing the material system would be useful. For example, the effects of redesigning the active region to contain varying numbers of quantum wells, or to contain wells of various depth and width, may be examined. By altering the quantum well properties, variations in device operation due to changes in exciton binding energies and changes in reverse bias tuning behavior can be studied. Additionally, the optical waveguide characteristics can be designed to suit a desired application. For example, the detector's waveguide mode can be made more symmetrical and shaped to match that of an input fiber's, improving the fiber-to-waveguide coupling efficiency. Many passive waveguide components have such a structure. Designs can also be implemented for increased absorption by maximizing the optical confinement factor with respect to the quantum wells.

One of the desirable features of this approach is the potential offered for monolithic integration with other waveguide-based components. A combination of great interest is a tunable diode laser with an integrated wavelength monitor. The importance of this component was discussed in chapter 1. Since both devices typically work near the absorption band edge of strained quantum wells and have similar layer structures, they are well matched for integration. However, the development of this device is not trivial as many practical issues arise, such as the need for high electrical isolation, precision temperature control and potentially an optical attenuator. Integration with passive components, such as a demultiplexer or optical waveguide, is another possibility. Again, this is not a straightforward task as such a device requires absorbing and non absorbing sections to be present on a single semiconductor chip. This problem may be solved by chemically removing the absorbing regions in the passive sections and then performing a material regrowth. Alternatively, quantum well intermixing techniques may be used which can induce localized changes in band gap [78].

For strain sensing applications, it would be desirable to demonstrate the simultaneous fabrication of broadband optical sources and wavelength monitors on the same semiconductor wafer. Since both devices are produced in close proximity of one another on the same material, they will have similar band gap energies. This ensures wavelength overlap between source output and detector operating range, as well as significantly lowering production costs. This has been demonstrated at 980 nm by Densmore and Jessop [25], who first constructed superluminescent diode sources with wavelength monitors which were later used as part of a fiber Bragg grating sensor. However, this has not yet been achieved at 1.55 μm.

Finally, some practical issues may be investigated. Studies involving reliability and aging associated effects, robustness, fabrication and growth tolerances, packaging issues and wafer yields would be important for commercial production.

Appendix A

Photodetector Electronics

A.1 Photocurrent Divider Circuit

Fig. A.1 illustrates the circuit used for the measurement of the detector responsivities and the photocurrent ratio. A two stage amplifier is used to convert the small photocurrents to measurable voltage signals. Two symmetrical arms are utilized; one for each detector segment. The photocurrent generated by a detector segment is sent directly to the input of a LT1055 precision operational amplifier. It is configured as a transimpedence amplifier with a gain of 10^6 V/A, determined by the 1 MΩ feedback resistor. The value of the feedback resistor and thus the gain, was constantly being changed to suit the incoming light intensity. The second stage consists of a low noise OP-27 precision operational amplifier. It has a gain of 10 and is used to amplify the output voltage of the transimpedence amplifier. A 2 kΩ potentiometer is added to OP-27's non-inverting input to control the input offset voltage to cancel any background signal. The output voltages from the second detector stages are recorded by two digital multimeters and the generated photocurrents can then be deduced. The outputs are also directed to the inputs of a DIV100 analog voltage divider chip which divides the rear detector signal by the front. The voltage divider has a gain of 10, so that an output voltage of 10 V corresponds to a photocurrent ratio of 1. A positive voltage bias is applied to the common n-side contact of the photodetectors to act as a reverse bias.

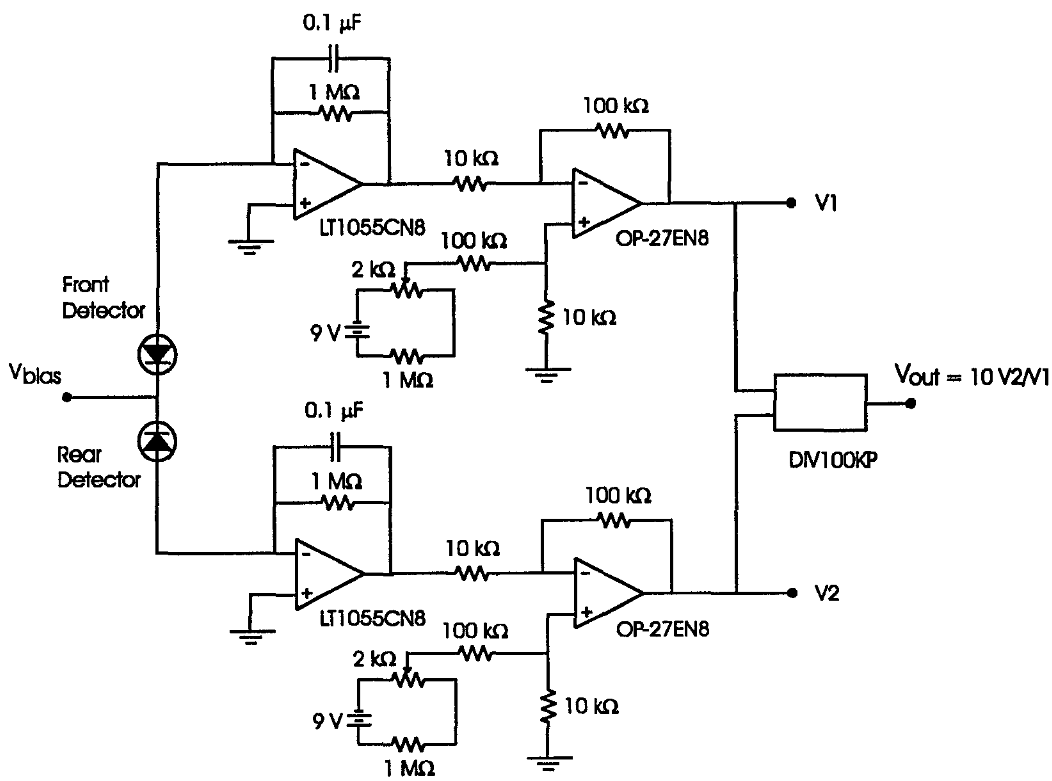

Figure A.1: Circuit used for the measurement of photocurrent and the photocurrent ratio.

A.2 Comparator Circuit

The active locking of the photocurrent ratio to a fixed value is accomplished by use of a comparator circuit shown in Fig. A.2. The comparator circuit generates a positive feedback voltage which is directly connected to the base of the wavelength monitor. The feedback signal induces a shift of the detector band edge via the QCSE, to actively lock the photocurrent ratio to a fixed preset value. As the signal wavelength is changed, the comparator output varies to maintain the locking condition.

The photocurrent signals from the two detector segments are passed through a two stage amplifying process similar to that of the photocurrent divider circuit. The transimpendence gain of the first stages are set to be 10^5 V/A. The second amplifying stage has a fixed gain of 10 for the rear detector element whereas, a potentiometer is added to the front detector amplifier to allow the gain to be varied. The gain of the upper amplifying path is set such that the ratio of the second stage gains is equal to the inverse of the photocurrent ratio value that we wish to lock to. The outputs of the voltage amplifiers are sent to the inputs of a high gain difference amplifier which generates a signal proportional to their difference. The negative output signal then passes through an inverting voltage integrator to convert it to a positive voltage and to reduce noise. A Zener diode is added to this stage to limit the output voltage to be less than 7.5 V for protection of the device. Finally, an additional amplifier is added with an adjustable offset voltage to ensure that the feedback signal remains positive. The output of the comparator is then sent to the common base electrode of the wavelength monitor.

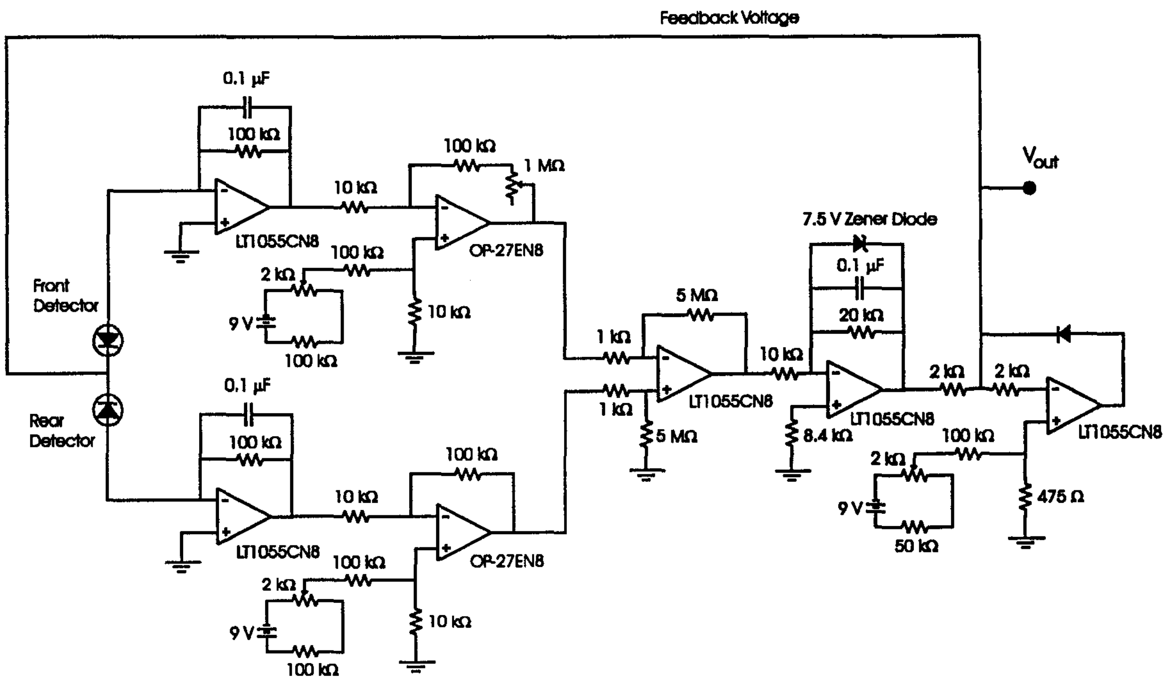

Figure A.2: Detector electronics to actively lock the photocurrent ratio to a fixed value by means of varying the reverse bias feedback voltage.

Appendix B

Mask Sets Used for Photolithographic Processing

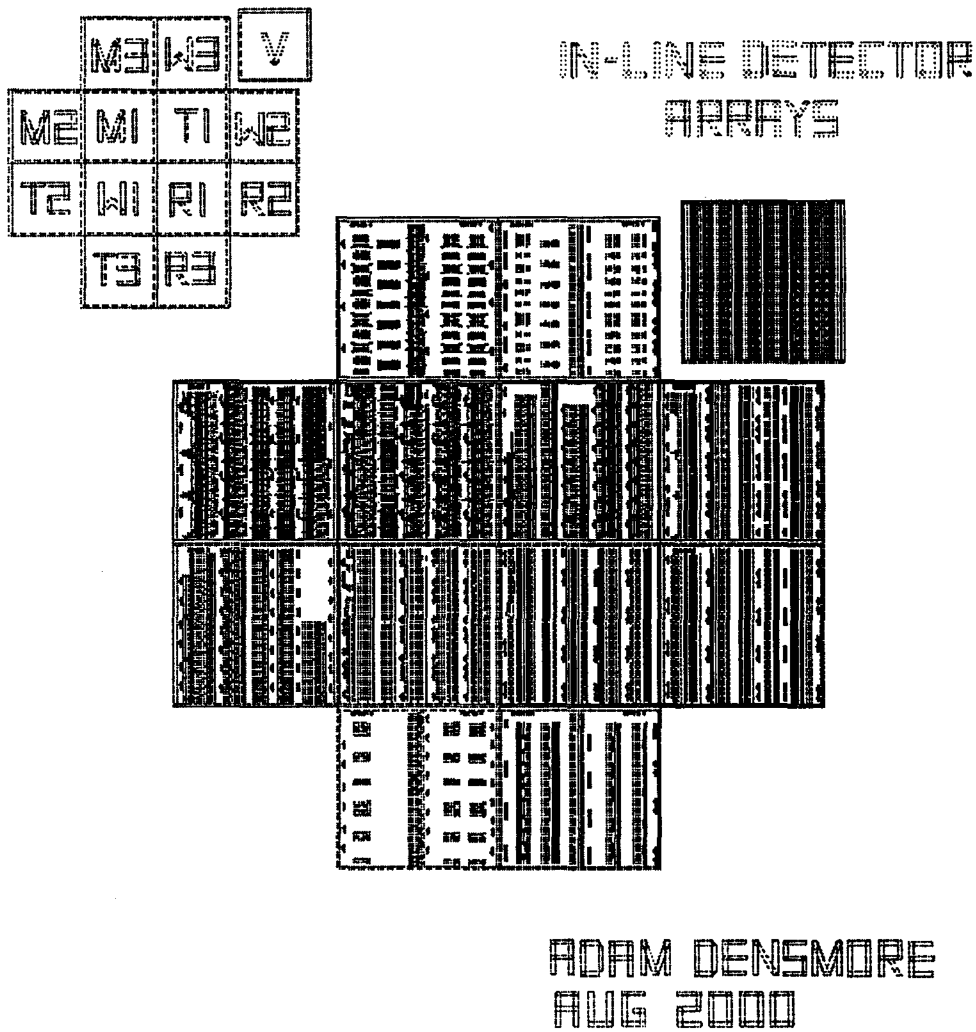

Figure B.1: Photomask layout used for device fabrication.

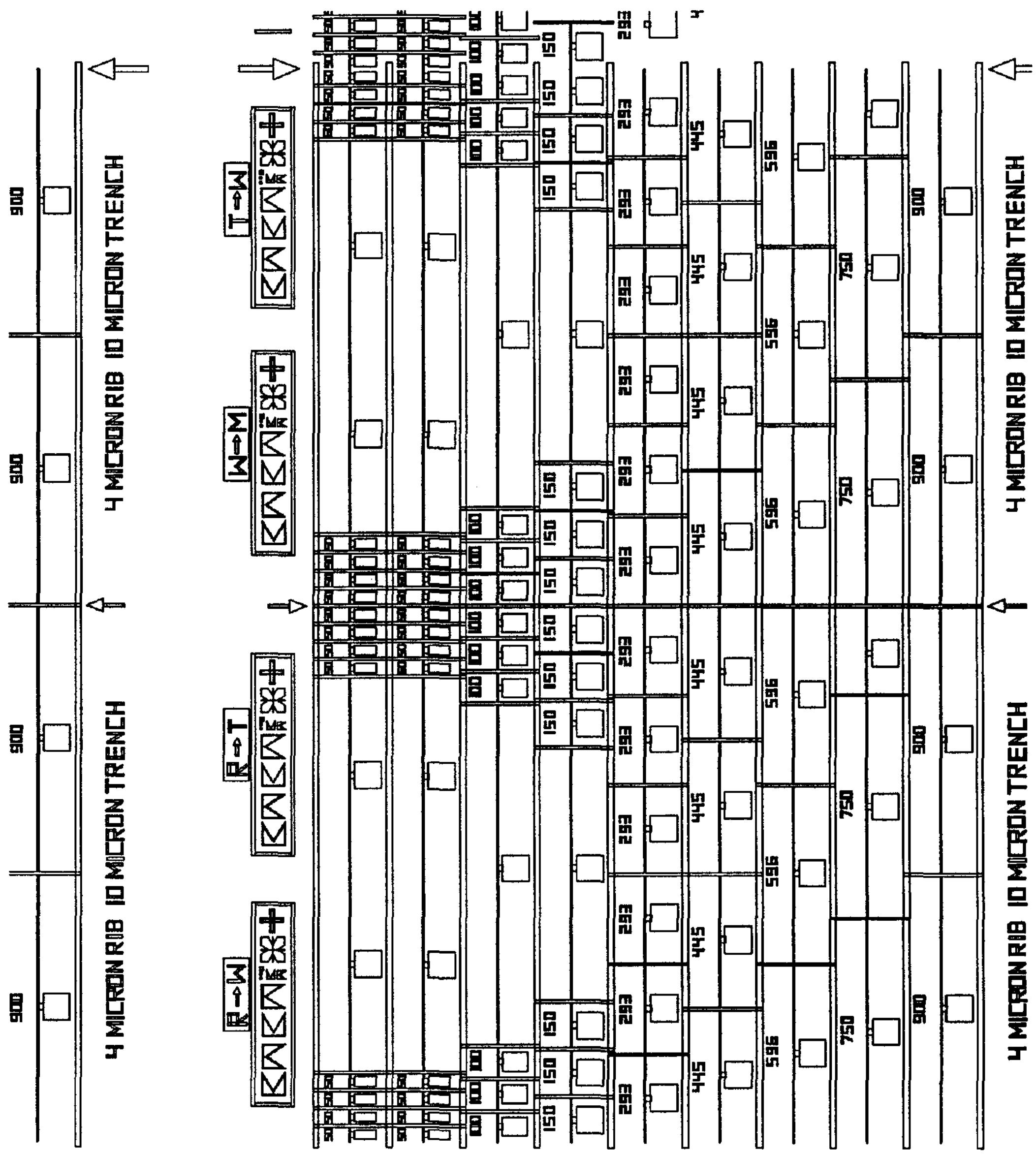

Figure B.2: Magnified view of all mask layers superimposed.

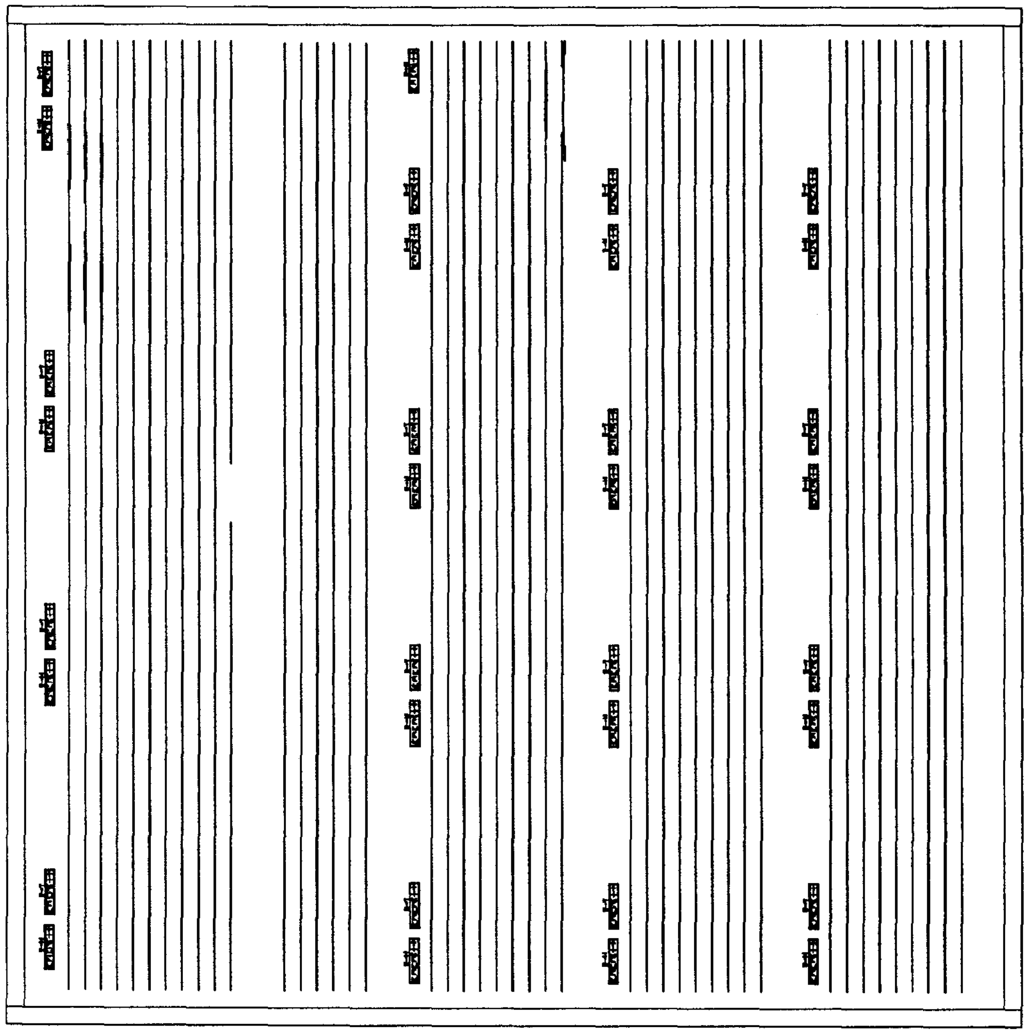

Figure B.3: Photomask layer for the definition of the waveguide ridges.

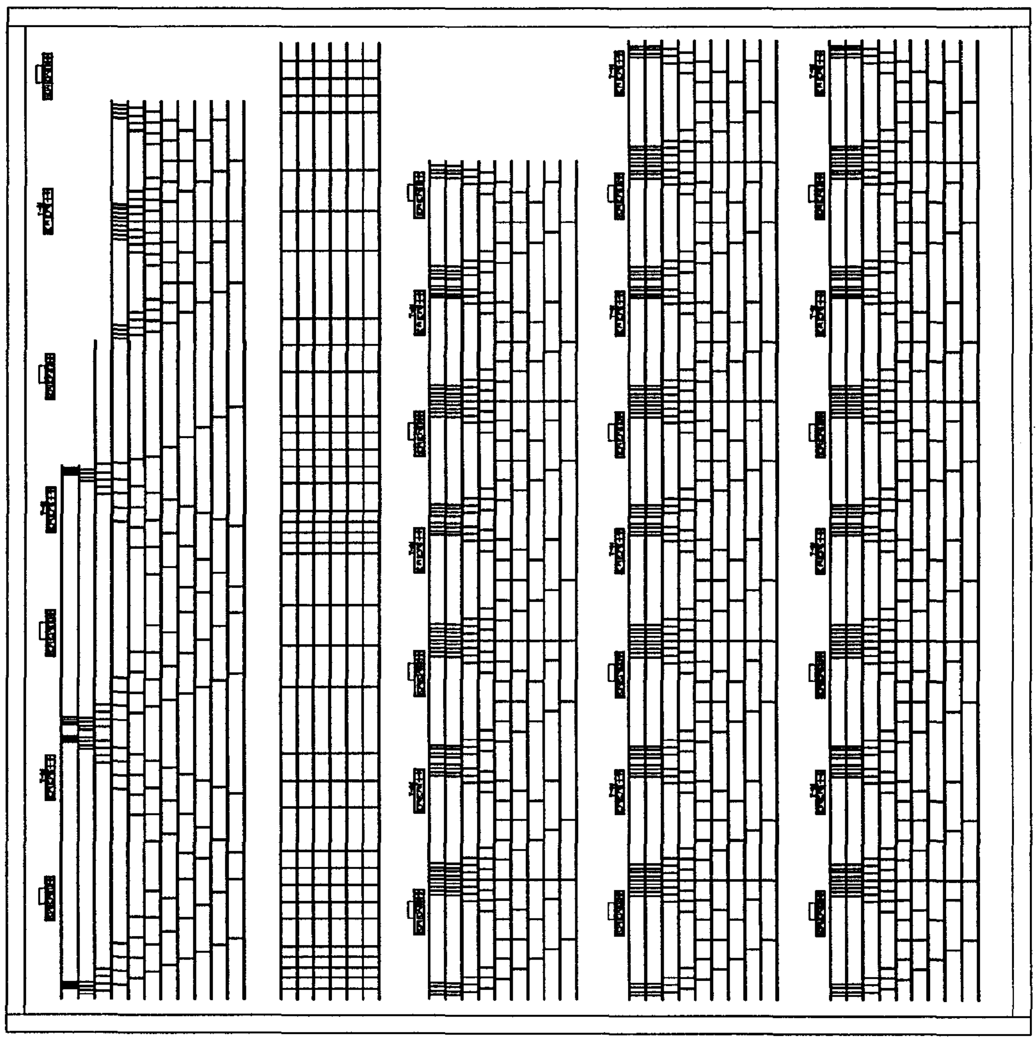

Figure B.4: Photomask layer for the isolation trench etch.

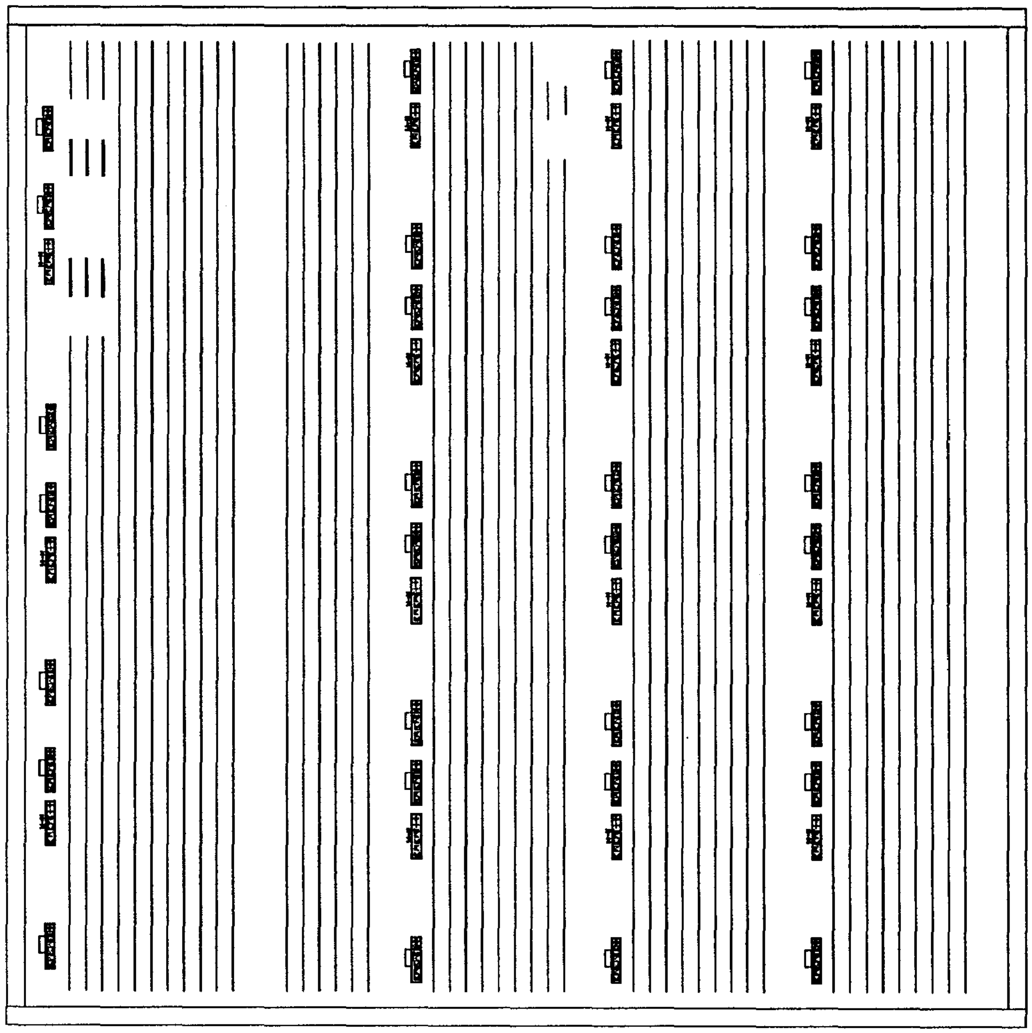

Figure B.5: Photomask layer for the etching of the contact windows above the waveguide sections.

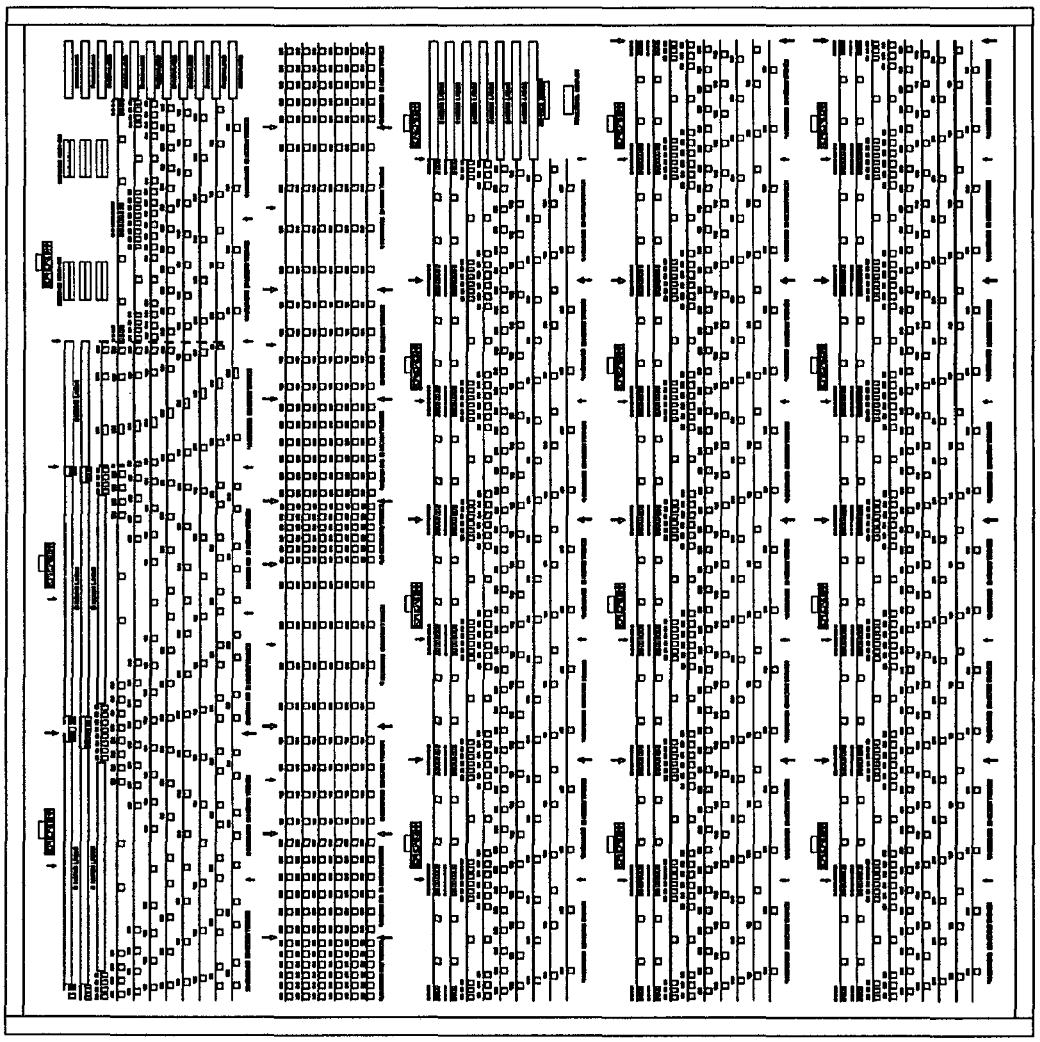

Figure B.6: Photomask layer used for lift-off to define the p-side electrodes.

Bibliography

[1] D. Wood, *Optoelectronic semiconductor devices.* Toronto: Prentice Hall, 1994.

[2] G. Agrawal, *Fiber optic communication systems.* Toronto: John Wiley and Sons, first ed., 1992.

[3] C. Park, W. Seo, and B. Yoon, "Simple channel monitoring method for fail detection of multiple WDM channels using a wavelength selective detector," *Electronics Lett.*, vol. 34, pp. 1677–1678, Aug. 1998.

[4] S. Hendow, "High-bandwidth networks bring new monitoring requirements," *Laser Focus World*, pp. 171–178, Aug. 1998.

[5] H. Lee and S. Yang, "Long-term stabilization of the frequency and power of a laser diode," *Rev. Sci. Instrum.*, vol. 67, pp. 2671–2674, Aug. 1996.

[6] R. Vodhanel, M. Krain, R. Wagner, and W. Sessa, "Long-term wavelength drift of the order of -0.01 nm/yr for 15 free-running DFB laser modules," *Proc. of OFC, Technol. Digest Series*, Feb. 1994.

[7] B. Mason, S. DenBaars, and L. Coldren, "Tunable sampled-grating DBR lasers with integrated wavelength monitors," *IEEE Photon. Technol. Lett.*, vol. 10, pp. 1085–1087, Aug. 1998.

[8] S. Lee, L. Lin, and M. Wu, "Distributed feedback lasers integrated with micromachined wavelength meters for dense WDM systems," *Proc. of LEOS, Annual Meeting*, pp. 511–512, 1996.

[9] A. Kersey, M. Davis, H. Patrick, M. LeBlanc, K. Koo, C. Askins, M. Putnam, and E. Friebele, "Fiber grating sensors," *J. Lightwave Technol.*, vol. 15, pp. 1442–1463, Aug. 1997.

[10] K. Hill and G. Meltz, "Fiber Bragg grating technology: fundamentals and overview," *J. Lightwave Technol.*, vol. 15, pp. 1263–1276, Aug. 1997.

[11] T. Berkoff and A. Kersey, "Fiber Bragg grating array sensor system using a bandpass wavelength division multiplexer and interferometric detection," *IEEE Photo. Technol. Lett.*, vol. 8, pp. 1522–1524, Nov. 1996.

[12] X. Jiang, J. Kemp, Y. Ning, A. Palmer, and K. Grattan, "Accurate wavelength determination in a Wollaston interferometer for sensor applications," *IEEE Photon. Technol. Lett.*, vol. 8, pp. 1055–1057, Aug. 1996.

[13] M. Davis and A. Kersey, "Application of a fiber Fourier transform spectrometer to the detection of wavelength-encoded signals from Bragg grating sensors," *J. Lightwave Technol.*, vol. 13, pp. 1289–1295, July 1995.

[14] A. Kersey, T. Berkoff, and W. Morey, "High-resolution fibre-grating based strain sensor with interferometric wavelength-shift detection," *Electron. Lett.*, vol. 28, pp. 236–238, Jan. 1992.

[15] T. Dimmick and J. Weidner, "Simple, inexpensive wavemeter implemented with a fused fiber coupler," *Appl. Optics*, vol. 36, pp. 1898–1901, March 1997.

[16] M. Davis and A. Kersey, "All-fiber Bragg grating strain-sensor demodulation technique using a wavelength division coupler," *Electron. Lett.*, vol. 30, pp. 75–77, Jan. 1994.

[17] S. Melle, A. Alavie, S. Karr, T. Coroy, K. Liu, and R. Measures, "A Bragg grating-tuned fiber laser strain sensor system," *IEEE Photo. Technol. Lett.*, vol. 3, pp. 274–276, Mar. 1991.

[18] A. Ribeiro, L. Ferreira, M. Tsvetkov, and J. Santos, "All-fibre interrogation technique for fibre Bragg sensors using a biconial fibre filter," *Electron. Lett.*, vol. 32, pp. 382–383, Feb. 1996.

[19] A. Kersey, T. Berkoff, and W. Morey, "Multiplexed fiber Bragg grating strain-sensor system with a Fabry-Perot wavelength filter," *J. Lightwave Technol.*, vol. 17, pp. 1415–1421, Aug. 1999.

[20] M. Xu, H. Geiger, J. Archambault, L. Reekie, and J. Dakin, "Novel interrogating system for fiber bragg grating sensors using an acousto-optic tunable filter," *Electron. Lett.*, vol. 29, no. 17, pp. 1510–1511, 1993.

[21] K. Tsuzuki, H. Takeuchi, S. Oku, H. Tanobe, Y. Kadota, and M. Yamamoto, "Temperature insensitive InGaAsP/InP optical filter integrated with dual photodiodes," *Electron. Lett*, vol. 33, pp. 1948–1949, Nov. 1997.

[22] T. Wood, "Wavelength-selective voltage-tunable photodetector made from multiple quantum wells," *Appl. Phys. Lett.*, vol. 47, pp. 190–192, Aug. 1985.

[23] T. Coroy, R. Measures, T. Wood, and C. Burrus, "Active wavelength measurement system using an InGaAs-InP quantum-well electroabsorption filtering detector," *IEEE Photon. Technol. Lett.*, vol. 8, pp. 1686–1688, Dec. 1996.

[24] X. Wu, P. Jessop, D. Bruce, B. Robinson, and D. Thompson, "In-line quantum well waveguide photodetectors for the measurement of wavelength shifts," *J. Lightwave Technol.*, vol. 15, pp. 2278–2283, 1997.

[25] A. Densmore and P. Jessop, "Wavelength monitoring devices for use in fiber optic sensors," *Conf. Lasers and Electo-Optics, OSA Tech. Dig. Ser., Washington, DC: Opt. Soc. Amer.*, vol. 6, p. 57, 1998.

[26] A. Densmore and P. Jessop, "Quantum-well waveguide photodetector for high-precision wavelength monitoring about 1.55 μm," *IEEE Photon. Technol. Lett.*, vol. 11, no. 12, pp. 1653–1655, 1999.

[27] A. Densmore and P. Jessop, "Arrays of wavelength monitoring photodetectors for WDM and fiber sensing applications," *Proc. of SPIE*, vol. 4277, pp. 77–84, Jan. 2001.

[28] S. Adachi, *Physical properties of III-V semiconductor compounds.* Toronto: John Wiley and Sons, 1992.

[29] S. Adachi, "Material parameters of InGaAsP and related binaries," *J. Appl. Phys.*, vol. 53, pp. 8775–8792, Dec. 1982.

[30] S. Chuang, *Physics of Optoelectronic Devices.* Toronto: John Wiley and Sons, 1995.

[31] O. Madelung, M. Schulz, H. Weiss, and Landolt-Borstein, *Semiconductors.* Berlin: Springer, 3 ed., 1982.

[32] E. Kuphal, "Phase diagrams of InGaAsP, InGaAs, and InP lattice matched to (100)InP," *J. Crys. Growth*, vol. 67, pp. 441–457, 1984.

[33] G. Pettit and W. Turner, "Refractive index of InP," *J. Appl. Phys.*, vol. 36, p. 2081, 1965.

[34] H. Burkhard, H. Dinges, and E. Kuphal, "Optical properties of InGaAsP, InP, GaAs, and GaP determined by ellipsometry," *J. Appl. Phys.*, vol. 53, pp. 655–662, Jan. 1982.

[35] S. Chuang, "Efficient band-structure calculations of strained quantum wells," *Phys. Rev. B*, vol. 43, no. 12, pp. 9649–9661, 1991.

[36] C. Cohen-Tannoudji, B. Diu, and F. Laloe, *Quantum mechanics.* New York: Wiley, 1977.

[37] M. Li, *Modern semiconductor quantum physics.* New Jersey: World Scientific, 1994.

[38] C. Weisbuch and B. Vinter, *Quantum semiconductor structures: fundamentals and applications.* Toronto: Academic Press, 1991.

[39] J. Matthews and A. Blakeslee, "Defects in epitaxial multilayers I. Misfit dislocations," *J. Cryst. Growth*, vol. 27, pp. 118–125, 1974.

[40] J. Evans, *Effects of intentionally mismatch strain on the operating characteristics and temperature performance of InGaAsP/InP long wavelength semiconductor lasers.* PhD thesis, McMaster University, Nov 1993.

[41] L. Coldren and S. Corzine, *Diode lasers and photonic integrated circuits.* Toronto: John Wiley and Sons, 1995.

[42] M. Jaros, *Physics and applications of semiconductor microstructures.* New York: Oxford University Press, 1989.

[43] C. Kittel, *Introduction to solid state physics.* Toronto: John Wiley and Sons, 1986.

[44] H. Mathieu, P. Lefebvre, and P. Christol, "Simple analytical method for calculating exciton binding energies in semiconductor quantum wells," *Phys. Rev. B*, vol. 46, pp. 4092–4101, Aug. 1992.

[45] R. Green, K. Bajaj, and D. Phelps, "Energy levels of Wannier excitons in GaAs-AlAs quantum well structures," *Phys. Rev.*, vol. B29, pp. 1807–1812, 1984.

[46] T. Wood, "Multiple quantum well waveguide modulators," *J. Lightwave Technol.*, vol. 6, pp. 743–757, June 1988.

[47] A. Tipping, G. Parry, and P.Claxton, "Comparison of the limits in performance of multiple quantum well and Franz-Keldysh InGaAs/InP electroabsorption modulators," *IEE Proc.*, vol. 136, Pt.J, pp. 205–207, Aug. 1989.

[48] T. Wood, "Direct measurement of the electric field dependent absorption coefficient in GaAs/AlGaAs multiple quantum wells," *Appl. Phys. Lett.*, vol. 48, pp. 1413–1415, May 1986.

[49] T. Tutken, G. Frankowsky, A. Hangleiter, V. Harle, K. Streubel, and F. Scholz, "Quantum confined Stark effect in InGaAs/InP and InGaAs/InGaAsP multi

quantum well structures," *Superlattices and Microstructures*, vol. 7, no. 4, pp. 309–313, 1990.

[50] D. Miller, D. Chemla, T. Damen, A. Gossard, W. Wiegmann, T. Wood, and C. Burrus, "Electric field dependence of optical absorption near the band gap of quantum well structures," *Phys. Rev. B*, vol. 32, no. 2, pp. 1043–1060, 1985.

[51] J.S. Weiner, "Strong polarization sensitive electroabsorption in GaAs/AlGaAs quantum well waveguides," *Appl. Phys. Lett.*, vol. 47, pp. 1148–1150, 1985.

[52] M. Koshiba, *Optical Waveguide Analysis.* Toronto: McGraw-Hill, 1990.

[53] R. Syms and J. Cozens, *Optical Guided Waves and Devices.* Toronto: McGraw-Hill, 1992.

[54] D. Griffiths, *Introduction to Electrodynamics.* New Jersey: Prentice Hall, 1989.

[55] H. Nishihara, M. Haruna, and T. Suhara, *Optical Integrated Circuits.* Toronto: McGraw-Hill, first ed., 1989.

[56] R. G. Hunsperger, *Integrated Optics: Theory and Technology.* New York: Springer-Verlag, third ed., 1991.

[57] L. M. Walpita, "Solutions for planar optical waveguide equations by selecting zero elements in a characteristic matrix," *Journal of the Optical Society of America A*, vol. 2, no. 4, pp. 595–602, 1985.

[58] D. Marcuse, *Theory of Dielectric Waveguides.* New York: Academic Press, 1974.

[59] G. Hocker and W. Burns, "Mode dispersion in diffused channel waveguides by the effective index method," *Appl. Opt.*, vol. 16, pp. 113–118, 1977.

[60] S. Sze, *Physics of semiconductor devices.* Toronto: John Wiley and Sons, 1969.

[61] B. Streetman, *Solid state electronic devices.* New Jersey: Prentice Hall, fourth ed., 1995.

[62] S. Forrest, "Performance of InGaAsP photodiodes with dark current limited by diffusion, generation recombination, and tunneling," *IEEE J. Quantum Electron.*, vol. QE-17, pp. 217–259, Feb. 1981.

[63] A. Alping, "Waveguide pin photodetectors: theoretical analysis and design criteria," *IEE Proc.*, vol. 136J, pp. 177–182, June 1989.

[64] A. Alping, R. Tell, and S. Eng, "Photodetection properties of semiconductor laser diode detectors," *J. Lightwave Technol.*, vol. Lt-4, pp. 1662–1668, Nov. 1986.

[65] A. Larsson, P. Andrekson, S. Eng, and A. Yariv, "Tunable superlattice p-i-n photodetectors: characteristics, theory and applications," *IEEE J. Quantum Electron.*, vol. 24, pp. 787–801, May 1988.

[66] D. Yeo, K. Yoon, H. Kim, and S. Kim, "Integration of waveguide type wavelength demultiplexing photodetectors by the selective intermixing of an InGaAs-InGaAsP quantum well structure," *IEEE J. Quantum Electron.*, vol. 37, pp. 824–829, June 2001.

[67] D. Moss, F. Ye, D. Landheer, P. Jessop, J. Simmons, H. Champion, I. Templeton, and F. Chatenoud, "Ridge waveguide quantum well wavelength division demultiplexing detector with four channels," *IEEE Photon. Technol. Lett.*, vol. 4, pp. 756–759, July 1992.

[68] A. Katz, B. Weir, and W. Dautremont-Smith, "Au/Pt/Ti contacts to p-InGaAs and n-inp layers formed by a single metallization common step and rapid thermal processing," *J. Appl. Phys.*, vol. 68, pp. 1123–1128, 1990.

[69] A. Baca, F. Ren, J. Zolper, R. Briggs, and S. Pearton, "A survey of ohmic contacts to III-V compound semiconductors," *Thin Solid Films*, vol. 308-309, pp. 599–606, 1997.

[70] P. Webb, R. McIntyre, and J. Conradi, "Properties of avalanche photodiodes," *RCA Rev.*, vol. 35, pp. 234–277, June 1974.

[71] F. Osaka and T. Mikawa, "Excess noise design of InP/GaInAsP/GaInAs avalanche photodiodes," *IEEE J. Quantum Electron.*, vol. QE-22, pp. 471–478, 1986.

[72] K. Hill, B. Malo, F. Bilodeau, D. Johnson, and J. Albert, "Bragg gratings fabricated in monomode photosentive optical fiber by UV exposure through a phase mask," *Appl. Phys. Lett.*, vol. 62, pp. 1035–1037, 1993.

[73] D. Hall, W. Burns, and R. Moeller, "High-stability Er^{3+}-doped superfluorescent fiber sources," *J. Lightwave Technol.*, vol. 13, pp. 1452–1460, July 1995.

[74] D. Dagenais, L. Goldberg, R. Moeller, and W. Burns, "Wavelength stability characteristics of a high-power, amplified superfluorescent source," *J. Lightwave Technol.*, vol. 17, pp. 1415–1421, Aug. 1999.

[75] J. Wagener, P. Wysocki, M. Digonnet, and H. Shaw, "Effects of concentration and clusters in erbium doped fiber lasers," *Opt. Lett.*, vol. 18, pp. 2014–2016, 1993.

[76] R. Weis, A. Kersey, and T. Berkoff, "A four element fiber grating sensor array with phase sensitive detection," *IEEE Photon. Technol. Lett.*, vol. 6, no. 12, pp. 1469–1472, 1994.

[77] N. Park and P. Wysocki, "24-line multiwavelength operation of Erbium-doped fiber-ring laser," *IEEE Photon. Technol. Lett.*, vol. 8, pp. 1459–1461, Nov. 1996.

[78] J. Marsh, O. Kowalski, S. MacDougall, B. Qiu, A. McKee, and C. Hamilton, "Quantum well intermixing in material systems for 1.5 μm," *J. of Vacuum Sci. and Techn. A*, vol. 16, pp. 810–816, 1998.